Tuning Resistive Switching in Complex Oxide Memristors

A thesis submitted in fulfilment of the requirements for the degree of Doctor of Philosophy

Taimur Ahmed

M.Sc

Chalmers University of Technology, Gothenburg, Sweden

School of Engineering

College of Science, Engineering and Health

RMIT University

October 2017

Declaration

I certify that except where due acknowledgement has been made, the work is that of the author alone; the work has not been submitted previously, in whole or in part, to qualify for any other academic award; the content of the thesis is the result of work which has been carried out since the official commencement date of the approved research program; and, any editorial work, paid or unpaid, carried out by a third party is acknowledged.

_____

Taimur Ahmed
October 2017

Abstract

The continuous demand of lightweight portable, cheap and low-power devices has pushed the electronic industry to the limits of the current technology. Flash memory technology which represents the mainstream non-volatile memories has experienced an impressive development over the last decade. This led their fabrication down to a 16 nm node and implementation of high density 3D memory architectures. Due to the scaling limit of Flash technology the need of new memories that combine the characteristics of a Flash but overcome the scaling limits is increasing. In this surge, oxide based resistive memories – also called memristors – have emerged as a new family of storage-class memory. The extremely simple physical structure fast response, low cost and power consumption render resistive memories as a valid alternative of the Flash technology and an optimal choice for the next generation memory technology.

The nanoscale resistive memories have demonstrated a variety of memory characteristics which depends on the electrochemical properties of the oxide system and several physical parameters including device structure and electrical biasing conditions. This indicates a complex nature of the underlying microscopic switching mechanisms which require a thorough understanding in order to fully benefit from the virtue of this technology.

The work presented in this Doctoral Dissertation focuses on the realization and fine tuning the memory characteristics of $SrTiO_3$ based resistive switching memories. A novel synthesis route is adopted to realize highly complementary metal oxide semiconductor (CMOS) compatible nanoscale memristive devices and engineer the composition of the functional $SrTiO_3$ perovskite oxide. By following the novel synthesis approach, $SrTiO_3$ memristive devices with different stoichiometry such as different concentration of oxygen vacancies, metallic dopant species and physical structures are fabricated to achieve multifunctional characteristics of these devices. Rigorous electrical and material characterizations are carried out to analyze the resistive switching performance and understand the underlying microscopic mechanisms.

Stable multi-state resistive switching is demonstrated in donor (Nb) doped oxygen-deficient amorphous $SrTiO_3$ (Nb:*a*-STO_x) memories. The dynamics of multi-state switching behavior and the effect of Nb-doping on tuning the resistive switching are investigated by utilizing a combination of interfacial compositional evaluation and

activation energy measurements. Furthermore, multiple switching behaviors in a single acceptor (Cr) doped amorphous $SrTiO_3$ (Cr:*a*-STO_x) memory cell are demonstrate. A physical model is also suggested to explain the novel switching characteristics of these versatile memristive devices.

A highly transparent and multifunctional $SrTiO_3$ based memory system is fabricated which offers a reliable data storage and photosensitive platform for further transparent electronics. Also a unique photoluminescence mapping is presented as an identification technique for localized conduction mechanism in oxide resistive memories.

Finally, $SrTiO_3$ resistive memories are engineered to mimic biological synapses. A hybrid CMOS-memristor approached is presented to demonstrate first implementation of higher order time and rate dependent synaptic learning rules. Furthermore, these artificial synapses are tuned for energy efficient performance to highlight their potential for the future neuromorphic networks.

Acknowledgements

My deepest gratitude and thanks for my supervisors Assoc. Prof. Sharath Sriram, Assoc. Prof. Madhu Bhaskaran, Dr. Sumeet Walia and Dr. Omid Kavehei for their continuous encouragement, moral support, technical advice and valuable suggestions. I am grateful for all the unique opportunities provided to me by my supervisors. I am thankful to Hussein Nili for helping me in the early days of my research and introducing me to the exciting field of resistive memories. I am thankful to Prof. Vipul Bansal for his valuable insights on my research. Also thanks to Dr. Rajesh Ramanathan for his insights and valuable suggestions on spectroscopic experiments and data analysis.

The state-of-the-art scientific equipment and facilities of RMIT University have been indispensable in the successful completion of this research program. The valuable support of the technical staff across the network of RMIT University is gratefully acknowledged. I would like to thank MNRF and RMMF for their support during the fabrication and characterization of samples throughout the research work.

I deeply treasure the absolute support and love of my beloved family, especially my wife whom I always found encouraging in the stressful moments in the course of this research program. Without them, this work would not have been possible.

I deem it a source of pleasure in expressing my gratitude to my group-mates Dr. Shiva Balendhran, Ataur Rahman, Sruthi Kuriakose, Fahmida Rahman and Jeeson Kim for their help and support during experiments in the labs.

Last but not least, I want to thank RMIT for giving me a wonderful opportunity to do PhD and providing a wonderful environment to carry out this research work.

Contents

List of Figures

List of Abbreviations and Acronyms

STO	Strontium Titanate
a-STO	Amorphous Stronitum Titanate
CMOS	Complementary Metal Oxide Semiconductor
MIM	Metal-Insulator-Metal
XPS	X-ray Photoelectron Spectroscopy
PL	Photoluminescence
TEM	Transmission Electron Microscopy
EELS	Electron Energy Loss Spectroscopy
VCM	Valance Change Mechanism
CRS	Complementary Resistive Switching
BP	Bipolar
ReRAM	Resistive Random Access Memory
HRS	High Resistive State
LRS	Low Resistive State
STDP	spike-time-dependent-plasticity
V_o	Oxygen Vacancy

List of Appendices

1 Introduction

The enormous progress in the traditional memory technology and storage hierarchy over the past three decade is facing challenges in the design of large-scale and high performance systems. The gap between the memory space and performance is continually widening. Also the energy consumption and cost of the storage systems pose significant doubts on achieving even higher performance. This has driven a strong innovation in the current memory technology but it has also motivated for the development of alternative memory technologies as well, in anticipation of its scaling limitations.

Among several potential candidates for alternative memory, resistive random access memories (ReRAMs) have been recognize as a viable option due to their simple physical structure, scalability potential and reliable characteristics. The recent research on ReRAMs is focused on optimizing the performance of these devices through material and structural engineering and realizing large scale integration of memristive devices in hybrid CMOS-memristor systems.

In this context, the research in oxide based nano-electronics gained a significant attention due to their technological relevance.[1] The fascinating properties of complex oxides, such as perovskite oxides, arising from their atomic structure and interfaces (*i.e.*, oxide/oxide or metal/oxide) are the gateway to novel devices with potential to surpass their semiconductor predecessors, both in performance and scale.[2] Recently, perovskite oxide $SrTiO_3$ based ReRAMs have shown an immense potential for the

future high density memory systems.[3-5] Its self-doping tendency with oxygen vacancies subject to electrical or thermal stress can transform its electronic structure from a band insulator to a metallic conductor and facilitate electro-resistive switching suitable for two-terminal memory devices.[6, 7] The resistive switching in $SrTiO_3$-based devices is generally attributed to highly localized accumulation of oxygen vacancies (*i.e.,* nano-filaments) along the extended defect structures, which results in the local bypassing of the depletion layer at the metal–oxide interfaces.[6, 8] Additionally, the defect structure of STO can be directly manipulated *via* doping with a donor or acceptor type transition metal, which can be employed to modulate the electronic structure at local (*e.g.,* grain boundaries and point defects) and bulk levels.[8] This can be used as a tool to engineer the arrangement and electronic/ionic transport properties of nano-filaments, and therefore, the memristive devices.

1.1 Context and objective

The motivation of this Doctoral dissertation aligns with the demands of the on-going research in oxide resistive memories. The control of resistive switching characteristics with full understanding of the underlying mechanisms is highly required. This can lead to the realization of highly customable and multifunctional memories for the future high density memory systems and efficient neuromorphic networks. The research outlined herein addresses the following research questions (RQs):

1. How do the resistive switching characteristics change by introducing the oxygen vacancies and metal (acceptor and donor) dopant species in the prototypical $SrTiO_3$ oxide system?
2. What are the underlying conduction mechanisms in the oxygen deficient and doped amorphous $SrTiO_3$ resistive memories?
3. What are the switching characteristics of multi-layered $SrTiO_3$ resistive memory architectures?
4. Explore the capability of $SrTiO_3$ resistive memories to implement biological synaptic functions for the applications of brain-inspired neuromorphic computation and networks?

These RQs are systematically investigated and research findings are presented in the chapters of this dissertation.

1.2 Original Contributions

The scientific achievements and original contributions through this research work are listed below:

- In literature, perovskite oxide based resistive memories are reported either on substrates or thin films which are fabricated at high temperatures (more than 650 ˚C). This makes them incompatible with conventional CMOS technology, as such limiting their applications for future electronics.

  Herein, a room temperature synthesis route based on physical deposition (*i.e.*, sputtering) is developed to achieve perovskite oxide thin films with a control over their stoichiometry. It is demonstrated that by following this synthesis method CMOS compatible amorphous $SrTiO_3$ (*a*-STO) based resistive memories are fabricated on conventional substrates (*e.g.*, Si and SiO_2/Si). Furthermore, the control over synthesis parameters allowed engineering the resistive switching behaviour in resistive memories. In the context of composition of synthesized thin films, *a*-STO thin films with different compositions are demonstrated, as listed below:

  - In case of undoped *a*-STO thin films, different ratios of oxygen deficiencies (*i.e.*, oxygen vacancies) in the oxide system are achieved by using RF magnetron sputtering from a single ceramic source.
  - Acceptor and donor doped *a*-STO thin films with control over the concentration of dopant species are realized *via* co-sputtering of ceramic and metal targets. It is demonstrated that by engineering the composition of *a*-STO thin films allows the tuning of corresponding memory characteristics.
- Multi-state resistive switching behavior is achieved in donor doped Nb:*a*-STO resistive memories. A combination of electrical and composition analysis techniques are employed to identify the dynamics of charge transport in these novel resistive memories.
- First realization of a acceptor doped Cr:*a*-STO memory system exhibiting multiple resistive switching behaviours in a single memory cell which can be

selectively induced by a single parameter before their application. Thus offering a versatile resistive memory system capable of tuning its behaviour according to the demand by application. Furthermore, a thorough investigation is carried out to explain the underlying mechanism.

- First realization of a highly transparent *a*-STO based resistive memories with a transient response to a range of optical wavelengths. Indicating a multifunctional memory system with potential to operate as a non-volatile memory and at the same time as a photo-detector.
- A unique photoluminescence mapping is demonstrated to pinpoint the location of localized conductive paths in the transparent resistive oxide memories. Unlike the conventional cross-sectional methods to analyse the nature of localized defect structures in the oxide resistive memories, which require a tedious sample preparation and complex tools, this mapping technique is simple and non-destructive. Furthermore, it allows analysing the real-time applied field driven compositional changes in the functional oxides to understand the resistive switching mechanisms.
- The electroforming process (a soft breakdown of oxide under applied electric field) is regarded as the energy consuming and highly uncontrolled process to achieve resistive switching behaviour in any oxide based resistive memories. It may induce high device-to-device variability which limits the reliability of the memory system. Herein, *a*-STO based resistive memories are engineered to exhibit electroforming free resistive switching behaviour. Through the electrical and nano-compositional characterization, insights into the nanoscale nature of electroforming free behaviour are achieved.
- First experimental implementation of the higher order time and rate-dependent synaptic functions is demonstrated. The comparison of results obtained from *in-vivo* and *in-vitro* biological synapses (reported in literature) and *a*-STO resistive memories show a very close match. This imply that the *a*-STO memory can mimic the synaptic functionalities, hence an artificial neuro-synapse. Furthermore, a hybrid CMOS-memristor approach is presented to implement a variety of synaptic functions. This indicates the potential of *a*-STO based resistive memories for application in the future neuromorphic networks.

1.3 Thesis Outline

This dissertation covers the research work carried out to tune the resistive switching characteristics of *a*-STO based resistive. In order to effectively represent the scientific findings, each chapter addresses a specific research question (or questions). The structure of the thesis is outlined as follows:

Chapter 2 covers a brief literature review and background on the recent research into the perovskite oxide systems, memristive devices and resistive switching mechanisms.

Chapter 3 presents the multi-state resistive switching in Nb-doped *a*-STO memories. The role of donor dopants in modulating the switching behaviors is investigated by utilizing a combination of interfacial compositional evaluation and activation energy measurements. In this chapter RQ 1 and 2 are addressed.

Chapter 4 details the multiple resistive switching behaviors in a single cell of Cr-doped *a*-STO memories. Several comprehensive characterizations are employed to understand the underlying nanoscale mechanisms responsible for such a versatile switching behavior. This chapter addresses RQ 1 and 2.

Chapter 5 demonstrates a highly transparent and multifunctional *a*-STO based memory system. The transparent memory devices are fabricated in a multi-layer stacked configuration and their switching characteristics are evaluated. Transient photoresponse of these devices to a range of wavelengths is also presented. Furthermore, a unique PL mapping technique is showcased to identify the localized conduction in oxide based transparent resistive memories. This chapter provides research findings to answer RQ 3.

Chapter 6 shows the practical application of electroforming free *a*-STO resistive memories for the future highly efficient neuromorphic networks. A highly flexible hybrid CMOS-memristor approach is utilized to implement a variety of brain-inspired synaptic learning rules. This chapter addresses RQ 4.

1.4 Publications

1.4.1 Patent

1. **T. Ahmed**, S. Walia, M. Bhaskaranand and S. Sriram “Multifunctional and multi-bit storage resistive memories” Australian Provisional Patent, 2016902654 (2017).

1.4.2 First-authored papers

2. **T. Ahmed**, S. Walia, J. Kim, H. Nili, R. Ramanathan, E. L. H. Mayes, D. W. M. Lau , O. Kavehei, V. Bansal, M. Bhaskaran, S. Sriram "Transparent amorphous strontium titanate resistive memories with transient photo-response" *Nanoscale* 9 (38) (2017).
3. **T. Ahmed**, H. Nili, S. Walia, R. Ramanathan, S. Rubanov, J. Kim, O. Kavehei, V. Bansal, M. Bhaskaran, S. Sriram "Microstructure and dynamics of vacancy-induced nanofilamentary switching network in donor doped $SrTiO_{3-x}$ memristors" *Nanotechnology* 4 (50) (2016).
4. **T. Ahmed**, S. Balendhran, M. N. Karim, E. L. H. Mayes, M. R. Field, R. Ramanathan, M. Singh, V. Bansal, S. Sriram, M. Bhaskaran, S. Walia, "Degradation of black phosphorus is contingent on UV–blue light exposure" *npj 2D Materials and Applications* 1(1) (2017). *Not included in this dissertation*

1.4.2.1 In Progress

5. **T. Ahmed**, S. Walia, E. L. H. Mayes, R. Ramanathan, Paul Guagliardo, V. Bansal, M. Bhaskaran, J. J. Yang and S. Sriram "Creating multiple switching behaviors in strontium titanate based resistive memories" *in review*.
6. **T. Ahmed**, S. Walia, E. L. H. Mayes, R. Ramanathan, V. Bansal, M. Bhaskaran, S. Sriram and O. Kavehei "A neuro-inspired imitation of higher order synaptic learning using complex oxide memristors" *in review*.

1.4.3 Co-authored papers

7. J. Kim, **T. Ahmed**, H. Nili, J. Yang, D. S. Jeong, P. Beckett, S. Sriram, D. C. Ranasinghe, O. Kavehei "A physical unclonable function with redox-based nanoionic resistive memory" *IEEE Transactions on Information Forensics and Security*, DOI:10.1109/TIFS.2017.2756562 (2017).
8. F. Rahman, **T. Ahmed**, S. Walia, E. L. H. Mayes, S. Sriram, M. Bhaskaran, S. Balendhran "Two-dimensional MoO_3 via a top-down chemical thinning route" *2D Materials* 4 (3) (2017).
9. S. Walia, S. Balendhran, **T. Ahmed**, M. Singh, C. El-Badawi, M. D Brennan, P. Weerathunge, M. Karim, F. Rahman, A. Rassell, J.Duckworth, R. Ramanathan, G. E. Collis, C. J. Lobo, M. Toth, J. C. Kotsakidis, B.

Weber, M. Fuhrer, J. M. Dominguez-Vera, M. J.S. Spencer, I. Aharonovich, S. Sriram, M. Bhaskaran, V. Bansal "Ambient Protection of Few-Layer Black Phosphorus via Sequestration of Reactive Oxygen Species" *Advanced Materials* 29 (2017).

10. M. Singh, E. D. Gaspera, **T. Ahmed**, S. Walia, R. Ramanathan, J. Embden, E. Mayes, V. Bansal "Soft Exfoliation of 2D SnO with size-dependent optical properties" *2D Materials* DOI:10.1088/2053-1583/aa6efc (2017).
11. C. Zou, G. Ren, M. M. Hossain, S. Nirantar, W. Withayachumnankul, **T. Ahmed**, M. Bhaskaran, S. Sriram, M. Gu, C. Fumeaux "Metal-Loaded Dielectric Resonator Metasurfaces for Radiative Cooling" *Advanced Optical Materials* DOI: 10.1002/adom.201700460 (2017).
12. M. C Siu, S. R. Anderson, M. Mohammadtaheri, **T. Ahmed**, S. Walia, R. Ramanathan, V. Bansal "Role of Water in the Dynamic Crystallization of CuTCNQ for Enhanced Redox Catalysis (TCNQ= Tetracyanoquinodimethane)" *Advanced Materials Interfaces* 4 (15) (2017).
13. R. M. Clark, J. C. Kotsakidis, B. Weber, K. J. Berean, B. J. Carey, M. R. Field, H. Khan, J. Z. Ou, **T. Ahmed**, C. J. Harrison, I. S. Cole, K. Latham, K. Kalantar-zadeh, T. Daeneke "Exfoliation of quasi-stratified Bi_2S_3 crystals into micro-scale ultrathin corrugated nanosheets" *Chemistry of Materials* 28 (24) (2016).
14. S. Walia, Y. Sabri, **T. Ahmed**, M. R. Field, R. Ramanathan, A. Arash, S. K. Bhargava, M. Bhaskaran, S. Sriram, V. Bansal, S. Balendhran "Defining the role of humidity in the ambient degradation of few-layer black phosphorus" *2D Materials* 4 (1) (2016).
15. H. Nili, S. Walia, A. E. Kandjani, R. Ramanathan, P. Gutruf, **T. Ahmed**, S. Balendhran, V. Bansal, D. B. Strukov, O. Kavehei, M. Bhaskaran, S. Sriram "Donor-induced performance tuning of amorphous $SrTiO_3$ memristive nanodevices: Multistate resistive switching and mechanical tunability" *Advanced Functional Materials* 25 (21) (2015).

2 Literature Review

The approaching scaling limit of the conventional semiconductor memory technology motivated surge for alternative non-volatile memories with properties of high scaling, low power and low cost. Oxide based memories have shown potential to fulfil the demands of future memory technology. This chapter presents a brief introduction of the prototypical $SrTiO_3$ pervoskite oxide and its technological relevance for non-volatile memory technology.

2.1 Prototypical perovskite oxide: $SrTiO_3$

Over the past few decades, perovskite ABO_3 oxides have attracted great interest due to their dynamic (semiconducting, electro-chromic, magneto-resistive, dielectric and multi-ferroic) properties.[9] This can be attributed to the intrinsic flexibility they offer to change their electronic structure *via* localized or distributed changes in the valance states and a vast variety of compositional engineering. Furthermore, the BO_6 oxygen octahedron provides a large degree of freedom to tailor the material system for any specific application. Specifically, the polarization, ionic conductivity and self-doping tendency with oxygen vacancies make perovskite oxides useful for sensing and memory

devices.[10-12] As such, the perovskite oxides have been topic of intense studies for the realization of novel nanoscale oxide electronics.

2.1.1 Fundamentals of $SrTiO_3$

The bulk prototypical $SrTiO_3$ (STO) perovskite oxide is an ionic crystal with a cubic crystal structure at room temperature with a lattice constant of 3.9 Å.[13] It consists of SrO and TiO_2 layers stacked in [001] direction and also corner-shared TiO_6 octahedra form a framework with Sr ions. The undoped single crystal STO is an insulator with experimentally determinded indirect band-gap of 3.25 eV and direct band-gap of 3.75 eV.[14] As such, it is commonly used as a gate oxide or a substrate in oxide electronics due to its high dielectric constant. However, controlled engineering of the STO electronic structure and composition allows it to exhibit a vast variety of functional properties, such as superconductivity,[15] ferroelectricity,[16] magnetoresistance,[17] photoluminescence,[18] metal-insulator transition[19] and resistive switching.[4, 6, 20]

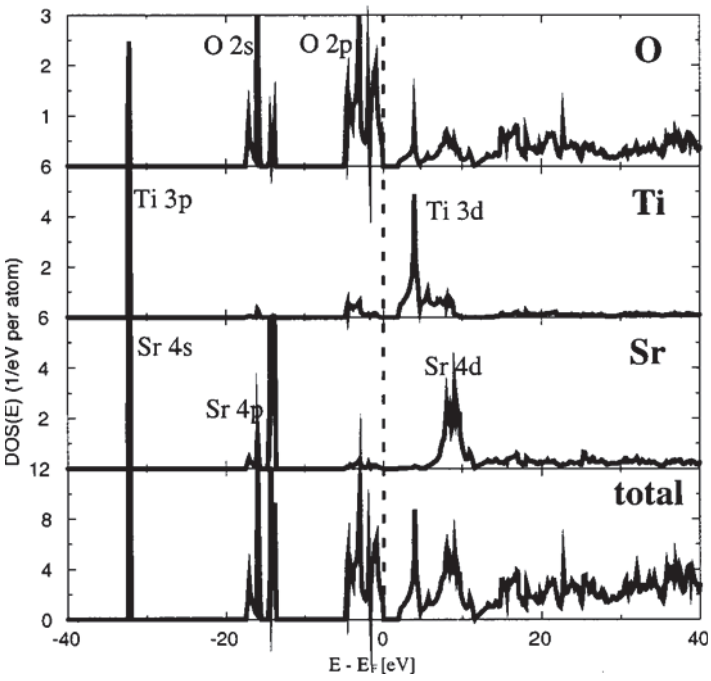

Figure 2.1 The calculated total and partial density of states (DOS) of pristine STO and O, Ti and Sr sites, respectively. Reproduced from Ref.[19]

From the electronic perspective, the conduction band edge of STO is composed of mainly Ti 3*d* states and followed at higher energies by the Sr 4*d* states. While the upper valence band is mainly dominated by O 2*p* states hybridized with Ti and Sr states.[14]

Figure 2.1 shows the site projected density of states where it is clearly shown that the bottom of the conduction band is dominated by the Ti states while the top of the valance band is mainly formed by the O states.

2.1.2 Defect chemistry of $SrTiO_3$

The densely packed crystal structure of STO can accommodate a variety of intrinsic and externally induced defects. The most significant defects include anion and cation vacancies on all three sub-sites (*i.e.*, Sr, Ti and O sites), and externally doped substitutional impurities. The interplay of these defects can be described by considering the defect chemistry of the STO.

The presence of vacancy-type defects in STO have been extensively studied by the electrical conductivity measurements as a function of temperature and analysed by the defect chemistry models.[21-23] Also based on the theoretical models, a good understanding has been developed to model the formation of intrinsic vacancy-type defects.[23-25] It is shown that the full Schottky defects ($V_{Sr}^{2-} + V_{Ti}^{4-} + 3V_O^{2+}$) have lower formation energy than the Frenkel-type defects which involve interstitial antisite-like disorders. However, the SrO partial Schottky defects ($V_{Sr}^{2-} + V_O^{2+}$) have even lower formation energy than the TiO_2 partial Schottky defects ($V_{Ti}^{4-} + 2V_O^{2+}$).[23, 24]

In the context of conductivity and ionic mobility in STO, the cation vacancies have negative charge and act as acceptor centres. At lower temperatures (<1300 K), the cation vacancies are immobile and considered as frozen-in defects due to their very low mobility.[26] On the other hand, oxygen vacancies are highly mobile even at room temperature and contribute in the ionic conductivity in STO rendering the carrier concentration in the rage from 10^{17} to 10^{19} cm^{-3}.[27]

In the bulk STO, the equilibrium point defect concentration of oxygen vacancies is controlled by the interaction of oxygen in the atmosphere, above a threshold exchange temperature (>700 K).[28] It is shown that the Joule heating can induce the localized temperature gradient higher than the threshold oxygen exchange temperature which can lead to the formation and mobility of oxygen vacancies (also discussed in the next chapters).[3] According to the oxygen exchange reaction:[28]

$$O_0 \rightleftharpoons \frac{1}{2}O_2(g) + V_O^{\bullet\bullet} + 2e' \tag{2.1}$$

Where O_0 represents neutral oxygen ions on the regular lattice sites and $V_O^{\bullet\bullet}$ denotes oxygen vacancies, in the Kröger-Vink notation. The Equation 2.1 shows the oxygen evolution and incorporation reaction. Also the oxygen vacancies act as donor sites in STO by generating electrons during the evolution reaction.

The Equation 2.1 indicates that the formation of an oxygen vacancy introduces two electrons into the conduction band of STO. Since the conduction band edge of STO is mainly occupied by the Ti 3*d* states (as discussed above), the effect of formation and recombination of oxygen vacancies may be studied by the Ti valance change, between Ti^{4+} and Ti^{3+} oxidation states, as shown in Equation 2.2:

$$2Ti^{4+} + O_0 \rightleftharpoons \frac{1}{2}O_2(g) + V_O^{\bullet\bullet} + 2Ti^{3+} \tag{2.2}$$

The electronic structure of STO can also be modified by substitutional doping of heterovalent cations. A deep understanding of variations in the characteristics of the STO associated with the carrier doping may be instrumental in engineering it properties for oxide based electronics.

2.1.3 Doping in $SrTiO_3$

The stoichiometric STO allows the doping of a variety of iso and heterovalent substitutions at its Sr and Ti sites. Depending on the charge of the dopant species, they can induce *p*-type or *n*-type conduction in STO. If the charge of dopants is less than the host cation they act as acceptors and induce *p*-type conduction. However, if the charge is higher than the host cation they behave like donors. The ionization equilibria are represented as:[28]

$$A^x \rightleftharpoons A' + h^{\bullet} \tag{2.3}$$

$$D^x \rightleftharpoons D^{\bullet} + e' \tag{2.4}$$

where A^x and D^x are the neutral acceptor and donor dopants, respectively, while A' and $D^{\bullet}$ are the ionic acceptor and donor species with single negative and single positive chage, respectively. Also, $h^{\bullet}$ are holes and e' are electrons.

2.1.3.1 Electron doping

At room temperature STO is an insulator, however a slightly *n*-type or *p*-type doped STO can undergo an insulator-to-metal transition.[29, 30] As explained above, the presence of oxygen vacancies introduce electrons in the conduction band of STO which make the oxygen vacancies as donor sites and induce *n*-type conduction in the oxide. The oxygen non-stoichiometry in the STO can be achieved by annealing at temperatures higher than the threshold oxygen-exchange reaction (*i.e.*, >700 K, Equation 2.1).[31] However, in the case of STO thin films it has been shown that the oxygen non-stoichiometry can be controlled during the synthesis processes.[32, 33] Also, STO oxides with different compositions are synthesized in this dissertation *via* sputtering and their composition is extensively analysed.

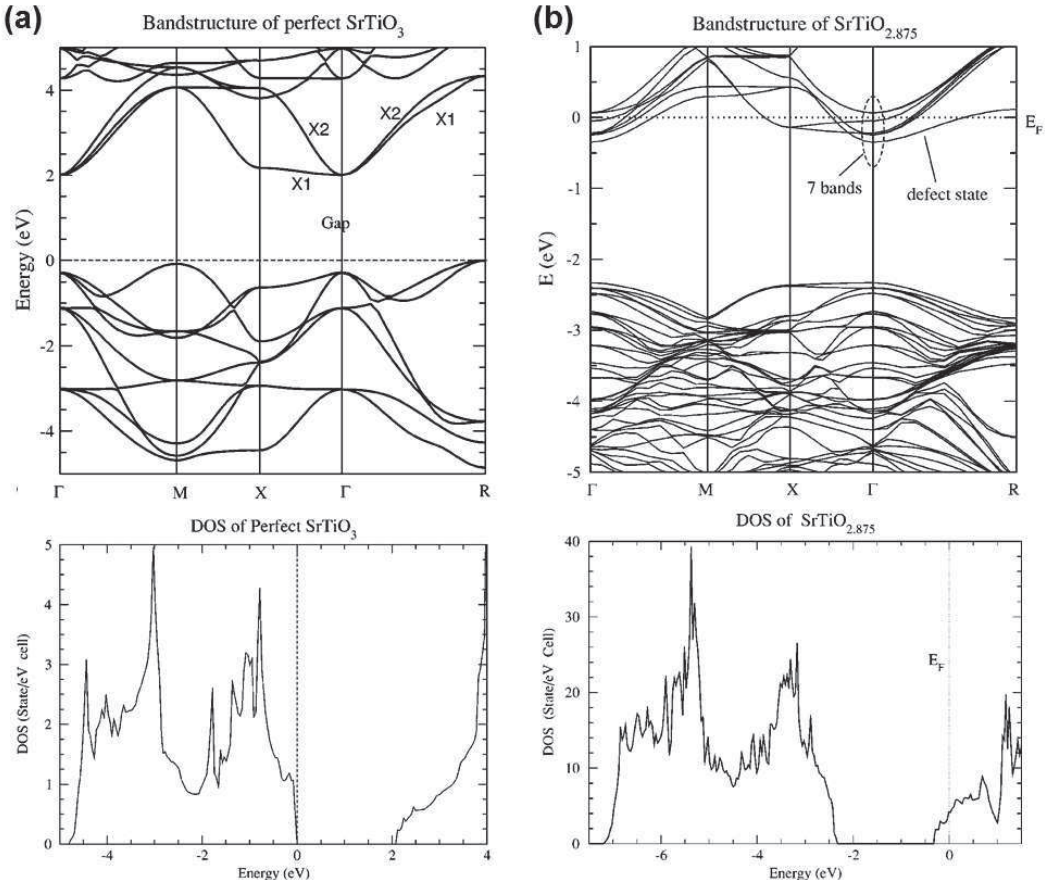

Figure 2.2 Band structure (upper panels) and total density of states (lower panels) of (a) stoichiometric $SrTiO_3$ and (b) oxygen deficient $SrTiO_3$. Reproduced from Ref.[14]

Figure 2.2 shows the density function theory (DFT) simulations of a stoichiometric and electron doped (*i.e.*, oxygen deficient) STO.[29] The band structure and density of state

(DOS) calculated for the stoichiometric STO show that it is an indirect band-gap insulator (Figure 2.2a). While, the oxygen vacancy doping shifts the Fermi level into the conduction band and the DOS at the Fermi level is not at zero due to the electrons introduced into the conduction band (Figure 2.2b). This induces to the metal-like conduction in the doped STO. However, the conduction can be controlled by the defining the concentration of oxygen vacancies, as will be shown in the following chapters.

2.1.3.2 *A*-site doping in $SrTiO_3$

It is well known that the doping in insulating STO may induce large changes in the lattice parameters. It is reported that the substitution of *A*-site Sr^{2+} cation by isovalent ions (such as Pb^{2+}, Ba^{2+}, Ca^{2+} and Mn^{2+}) induce polar state for the ferroelectric behavior in STO.[34] While no polar states are reported for La^{3+} doped at Sr^{2+} site.[34] This indicates that depending on the doping site and dopant species, a wide variety of phases (and hence physical properties), ranging from dipolar glass to relaxor and ferroelectric, can be achieved in STO.

Figure 2.3 shows the influence of chromium (Cr) doping at Ti and Sr on the band structure and electronic properties of the STO, estimated by the first principle DFT calculations.[35]

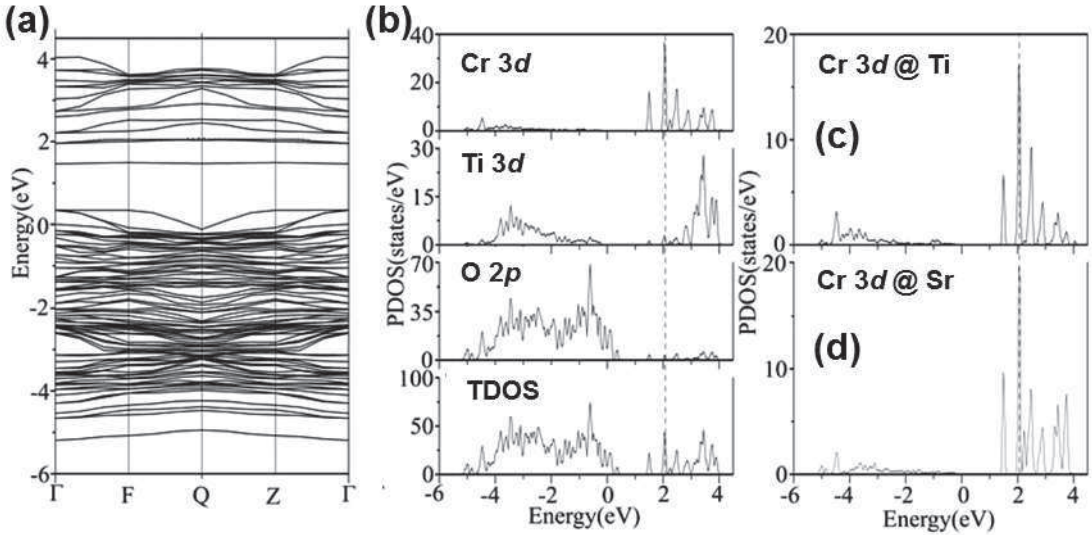

Figure 2.3 The effect of Cr doping on (a) the band structure, (b) total and partial DOS, (c) partial DOS of the Cr 3*d* states doped at Ti site and (d) Cr 3*d* states doped at Sr site in STO. Reproduced from Ref.[35]

The partial DOS calculated (Figure 2.3b) show that the conduction band is formed by Ti 3*d* and Cr 3*d* states while valence band is composed of O 2*p* states. However, the in-gap states appear are composed of the Cr 3*d* states, regardless of the Cr doping site (Figure 2.3c,d).[35]

In this dissertation, Cr-doped oxygen deficient STO thin films are synthesized and their electronic/micro structure is experimentally characterized, as discussed in Chapter 4. Through XPS and PL analyses, it is shown that Cr-doping *via* co-sputtering of Cr metal ions and oxygen deficient STO thin films, Cr cations mainly replace Ti ions at *B*-site. This induces the in-gap states and modifies the conductivity of the oxygen deficient STO thin films. As such, multiple resistive switching behaviours are observed.

2.1.3.3 *B*-site doping in $SrTiO_3$

Generally in the perovskite oxides, the electronic conduction is through the *B*-site network especially when *B*-site cations exhibit multiple oxidation states, such as Ti^{4+}/Ti^{3+}, Mn^{4+}/Mn^{3+} and Nb^{5+}/Nb^{4+} *etc*. This conduction is most likely due to the hopping of electrons from $B^{(n-1)+}$ cations to B^{n+} cations *via* the O-bridges. This indicates that with the higher concentration of $B^{(n-1)+}$ cations the electronic conductivity ($\boldsymbol{\sigma_e}$) will be higher too, given by the following relation:

$$\sigma_e = e \cdot \mu_e \cdot \boldsymbol{B^{(n-1)+}} \tag{2.5}$$

where μ_e denotes the electronic mobility. However, the mobility of electrons depends on several parameters, such as concentration of ions, symmetry/distortion of in the unit cell and microstructure of the oxide *etc*.

The physical properties and electronic structure of the STO with *B*-site doped cations have been studied, theoretically and experimentally.[29, 35-37] The niobium (Nb) doped STO has shown a lot of interest due to its stability at high temperatures (>500 K) and oxidizing atmospheres.[36] It is shown that in Nb-doped STO, Nb^{5+} cations replace Ti^{4+} *B*-site cations and induces *n*-type conduction. [36, 37]

Figure 2.4 shows the band structure and DOS for the Nb-doped STO, calculated by using first principles DFT simulations.[37] The band structure of Nb-doped STO (Figure 2.4a) shows that the Fermi-level shifts into the conduction band due to the carrier generation by the Nb substitutional doping. On the other hand, the total and

partial DOS of constituting ions (*i.e.*, O, Sr, Ti and Nb) shows that the bottom of the conduction band is formed by the Ti 3*d* and Nb 4*d* states (Figure 2.4b), while the top of the valence band is dominated by the O 2*p* states. As such, the Nb-doing induces insulator-to-metal transition. However, it is shown that the conductivity of the doped STO can be controlled from 10^{-7} to 10^{4} S/cm by changing the doping concentration of Nb.[36]

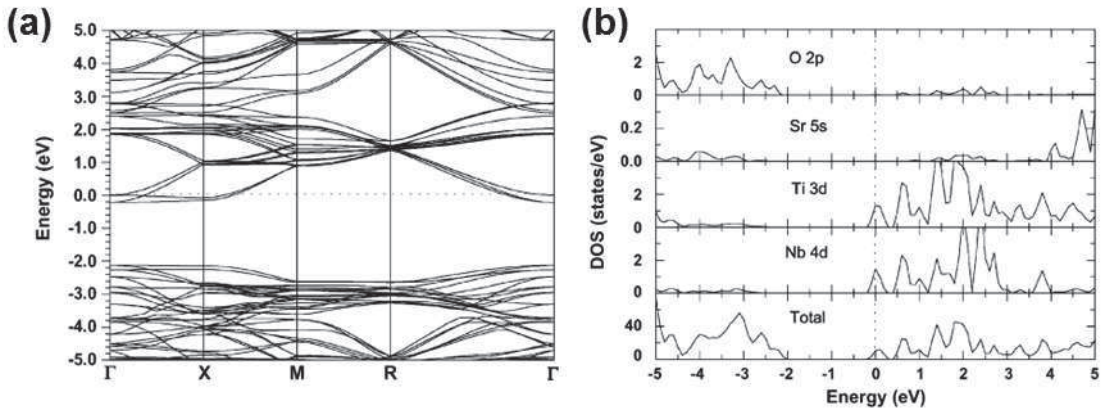

Figure 2.4 (a) The band structure, (b) total and partial density of states of Nb-doped STO. Reproduced from Ref.[37]

In this dissertation amorphous Nb-doped oxygen deficient STO thin films are synthesised by the RF sputtering technique. Also, the effect of Nb substitutional doping on the electronic structure of STO and dynamics of resistive switching behaviour are studied, as discussed in Chapter 3.

2.2 Memrisitve devices and systems

Memristor are resistive switching devices which remember their previous state: memory-resistors. The concept of memristor was first proposed by L. Chua in 1971 as a result of symmetry considerations in theoretical electronics. It was regarded as a resistor with memory element and theoretically completed the characteristic relation between the four fundamental electronic variables, *i.e.*, charge (q), voltage (v), current (i) and flux (φ), defining the memristance (M) by the relation:

$$d\varphi = M \cdot dq \tag{2.6}$$

Later L. Chua and S. M. Kang proposed the models for memristive systems which were defined by the following two equations:

$$\begin{aligned} \dot{\xi} &= F(\xi, x, t) \\ y &= G(\xi, x, t)x \end{aligned} \tag{2.7}$$

where x denotes the system inputs (such as voltage and current), y denotes the system output (such as current or voltage, respectively) and the function G yields either resistance or conductance of the system, respectively. While the function F explains how the internal states ξ evolve. As such, these set of equations (Equation 2.7) describe a highly non-linear resistor whose state of resistance depends on the previous history of the input signals and also on time.

In 2008, D. B. Strukov *et al*.[38] demonstrated a simple model to describe the memristance (M) as coupled with the ionic-electronic carrier transportation in a nanoscale system. Based on the model defined in Equation 2.7, they defined a charge-dependent state variable of the system which is subjected to the history of carrier distribution in the nanoscale system and related resistance (R) of the system with the memristance as:[38]

$$M(q) = R_{OFF}\left(1 - \frac{\mu_v R_{ON}}{D^2}\right) q(t) \tag{2.8}$$

where $M(q)$ is the charge-dependent memristance, R_{OFF} and R_{ON} are the OFF and ON state resistances, respectively, μ_v is the charge carrier mobility and D is the thickness of the employed solid-state device.

2.2.1 Resistive switching memories

The ionic mobility is a field-dependent property in solid state devices such as two-terminal metal-oxide memristive devices.[39] It is shown that an external applied electric field (>1 MV/cm) induces non-linear exponential-type characteristics in a few tens of nanometer thin metal-oxide based device. This indicates the solid-state devices exhibiting coupled ionic-electronic conduction have potential to show large memristive

response on very small time scales (<10 ns) and also the state retention time over years. This is mathematically modelled by the equation:[39]

$$\tau_{store}/\tau_{write} \sim L/2a \times exp(E/E_0) \quad (2.9)$$

Where τ_{store} and τ_{write} are the state retention and response time, respectively, L is the ionic diffusion length, a is the periodicity in the ionic crystal, E is the applied external field and E_0 $(= 2k_BT/a\,q)$ is the characteristic field for a particular mobile atom in the crystal.

This indicates that the memristive devices exhibit inherently non-volatile characteristic which makes them suitable for the memory applications.[28, 38-40] Furthermore, their simple two-terminal capacitor-like structure renders potential for the future ultra-dense memory and computational technologies by overcoming the limitation of the conventional CMOS memory technology. The fabrication and characterization of the resistive memories with different characteristics are the focus of this dissertation.

2.2.2 Resistive switching mechanism and types

Over the past decade, a wide variety of memristive devices and materials have been developed to improve the overall resistive switching characteristics of these novel devices. Along the course, different physical mechanisms have been reported to explain the switching behaviors of different functional materials.[41-44] Based on the functional switching materials and induced physical mechanisms, R. Waser *et al*.[28] have categorized the memory effects, as shown in Figure 2.5.

It has been largely accepted that the resistive switching in most of the binary and complex transition metal oxides is due to the field induced anionic transportation. The anions diffuse through the defect structure of the functional transition metal oxides which can be described as a valence change mechanism (VCM). These anionic species are mostly oxygen related defects, such as oxygen vacancies, exhibiting high mobility under the influence of the external electric fields. However, several other mechanisms have also been reported.[43, 44]

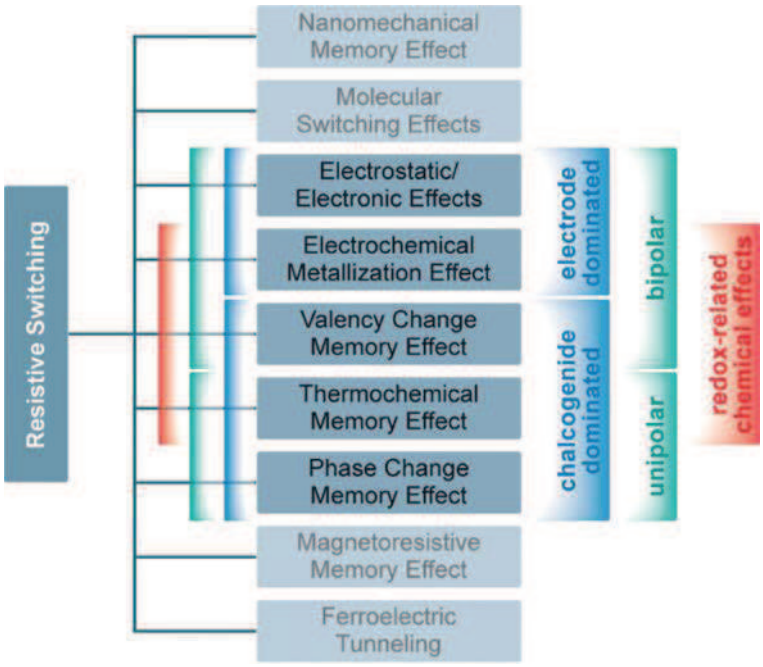

Figure 2.5 Classification of resistive switching mechanisms. Reproduced from Ref.[28]

2.3 Resistive switching in $SrTiO_3$

As mentioned in the previous section, different nanoscale mechanisms can induce resistive switching behaviors in different types of functional materials. However, this dissertation is focused on the VCM based resistive switching in STO based devices. This switching mechanism is widely associated with the oxygen ions migration and subsequent nanoscale redox reactions.[28, 45, 46] The STO is capable to harbour oxygen vacancies which may exist as point and line defects (depending on their concentration). Where these oxygen vacancies can be generated by thermal or electrical reduction of the stoichiometric STO or oxygen-deficient thin films can also be synthesized with as-grown oxygen vacancies.

In the STO based MIM devices, the as-grown thin films (with thickness >30 nm) usually exhibit high resistance. To induce the resistive switching in the MIM devices, typically a current-limited electroforming process is required. This initial electroforming step results in the localized accumulation of oxygen vacancies extending between the opposite electrodes through the perovskite oxide. The extended oxygen vacancy defect structures act as conductive nano-filamentary pathways for the fast electronic charge

transportation across the MIM device. A simplified description of the electroforming process can be considered as following;

In the pristine MIM devices, oxygen vacancies are randomly distributed in the STO oxide and the charge transport is governed by the interfaces between oxide and metallic electrodes. If the electrodes have low work-function and capable to form oxygen bonds with STO via localized redox reactions (as in the case of Ti electrodes), the distribution of oxygen vacancies will not change significantly under the influence of small applied voltages. However, if the electrodes have high work-function and block the ionic current, a non-linear concentration gradient builds up upon the applied electric field (as in the case of Pt electrodes). At higher applied voltages, the distribution of oxygen vacancies changes significantly and depending on the bias polarity, oxygen vacancies start to accumulate at the electroforming cathode. This process may evolve oxygen gas and more oxygen vacancies are formed, as described by the oxygen exchange reaction (Equation 2.1). At the electroforming voltages, the oxygen vacancies extend between the electroforming cathode and anode as a nano-filament and the current abruptly jumps to have values resulting in the low resistive state (*i.e.*, LRS or SET) of the MIM device.

Contrary to the electroforming or SET process, opposite polarity bias re-oxidizes the nano-filament *via* oxygen recombination reaction. This results in annihilation of the nano-filamentary path and high resistive state (*i.e.*, HRS or RESET) is achieved.

Throughout this thesis, detailed discussions (based on experimental evidences) have been provided to explain formation and dynamics of nano-filamentary pathways, and their influence on the resistive switching characteristics of different STO oxide based devices.

3 Dynamics of resistive switching

Doping of perovskite oxides has emerged as an attractive technique to create high performance and low energy non-volatile analog memories. This chapter examines the origins of improved switching performance and stable multi-state resistive switching in Nb-doped oxygen-deficient amorphous $SrTiO_3$ (Nb:a-STO_x) memories. The role of dopants in modulating the switching behaviors in a-STO_x devices is investigated by utilizing a combination of transmission electron microscopy, photoluminescence emission properties, interfacial compositional evaluation and activation energy measurements.

3.1 Introduction

The rapidly advancing memristive (RRAM) technology has found its foothold in multitude of novel applications ranging from high density memory architectures[47-49] to adaptive/neuromorphic computing[50-55] and security primitives[56-58]. Among most technologically relevant resistive switching phenomena, valence-change

mechanisms (VCM) are based on the drift diffusion of oxygen vacancies in binary and ternary metal-oxides subject to large electrical gradients.[59-63] The complete picture of switching mechanisms in VCM devices is likely more complex.[61, 64-68] Nevertheless, control over oxide stoichiometry (*e.g.*, oxygen deficiency gradient and substitutional dopants), metal-oxide interface quality and interfacial barriers has proven to be instrumental in fine tuning the device performance.[63, 69-75] As such, on-going technological issues such as the forming voltage, power consumption, and device yield and uniformity are likely to be addressed through structural and compositional engineering.

Recently, Nili *et al.* reported on the excellent switching performance of amorphous $SrTiO_{3-x}$ (*a*-STO_x) based devices and highlighted oxygen deficiency and substitutional donor doping as reliable pathways for improving and modulating their memristive performance.[69, 70] However, the exact nature of electrochemical redox processes and microstructure of the filamentary pathways in the disordered *a*-STO_x structure are still unclear.

This chapter presents the microstructure of the nano-filamentary conduction in *a*-STO_x. The impact of substitutional dopant (*i.e.*, Nb) in modulating the electronic structure and subsequent switching performance is probed by through microstructural analyses. Temperature stability and bias/time dependence of the switching behaviour are also used to ascertain the role of substitutional dopants and highlight their utility to modulate volatile and non-volatile behaviour in *a*-STO_x devices for adaptive and neuromorphic applications.

3.2 Microstrucutre of Nb:*a*-STO_x memories

3.2.1 Composition of Nb:*a*-STO_x MIM devices

Figure 3.1a shows the cross-sectional TEM view of a virgin Nb:*a*-STO_x device. The selected-area electron diffraction (SAED) patterns collected from multiple regions in the oxide layer (inset of Figure 3.1a) exhibit a halo pattern, confirming the uniform and amorphous nature of room temperature sputtered films.[70] While the low-concentration introduction of Nb species (Nb/Ti ≈ 0.025) does not alter the microstructure and relative concentration of sub-oxide ($Ti^{(3\pm\delta)+}$) species (see Appendix A). However, it does change the electronic structure of *a*-STO_x oxide as

demonstrated in broad blue-light emission (centered at 425 nm) under excitation from a 325 nm source (Figure 3.1b). In crystalline STO, room-temperature blue-light emission is believed to originate from in-gap self-trapped exciton (STE) states centered around oxygen deficient sites.[76] In the context of amorphous titanates, a broad emission peak centered at around 530 nm is associated with localized dynamic energy levels due to the large number of defect states in the severely disordered phase.[77-79] The characteristic amorphous emission peak appears in pristine *a*-STO_x spectrum and appears to shift towards higher energies upon niobium doping. This indicates that the evolution of photoluminescence spectra in Nb:*a*-STO_x is correlated with the increased density of localized defects and conduction electrons.

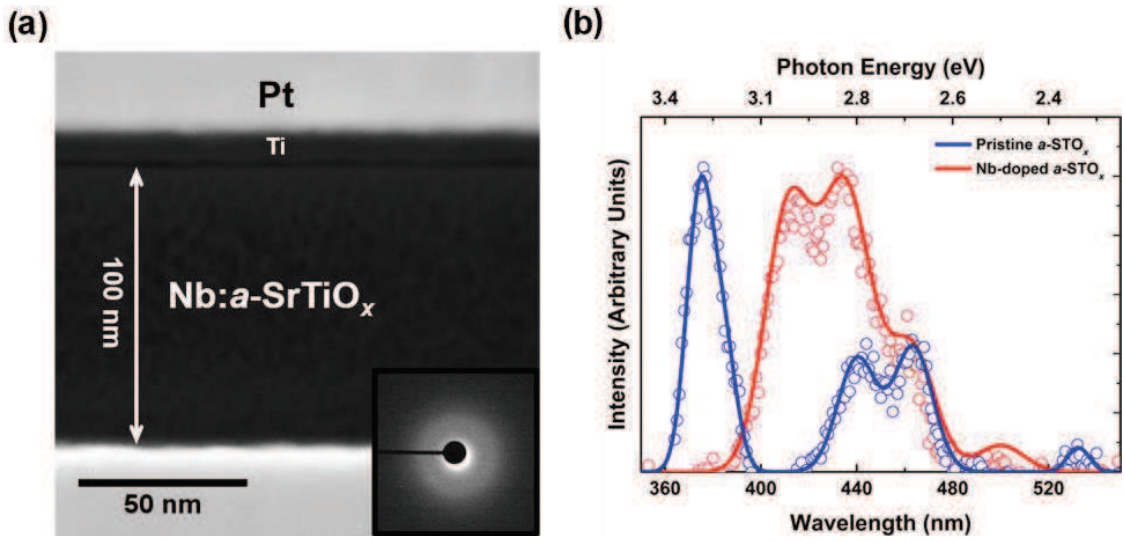

Figure 3.1 (a) Cross-sectional TEM micrograph of a Pt/Ti/Nb:*a*-STO_x/Pt (50/10/100/50 nm) device. The inset shows the SAED pattern acquired from the oxide region. (b) Room temperature photoluminescence (PL) spectrum of *a*-STO_x thin films under 325 nm excitation source.

The high resolution TEM (HR-TEM) and the electron energy loss spectroscopy (EELS) analysis are employed to complete the picture of nano-filamentary redox based conduction in *a*-STO_x devices. Representative FIB-cut specimens were prepared from the central region of virgin and switched (pulsed ON/OFF for at least 100 cycles) pristine as well as Nb:*a*-STO_x devices, and were used for successive EELS analysis and HR-TEM imaging. For area and line-scan surveys of EELS spectra in the switching devices, regions of interest (ROIs) in the cross-sections were identified as markedly

higher contrast regions in bright field STEM images. On the other hand, cross-sections of virgin devices were uniformly amorphous with no indication of crystallization or deformation. As such, random sample areas are chosen across the specimen to evaluate their composition and fine structure. (Appendix A).

3.2.2 Electronic structure of Nb:*a*-STO$_x$ MIM devices

Figure 3.2a and 3.2b show the relative oxygen ratio from survey scans in representative ROIs in virgin and switching devices. The relative compositions are determined through integrating the area under Ti-$L_{2,3}$ and O-*K* edges in EELS spectra.[80-82] The oxygen ratio is relatively uniform across the bulk of the oxide in virgin ROIs and oxygen deficient regions are spatially scattered (with the exception of largely reduced top Ti/*a*-STO$_x$ interface and isolated hotspots at the vicinity of bottom *a*-STO$_x$/Pt interface). In switching ROIs, reduced top interface propagates through the oxide (by an average of ~10 nm). Additionally, oxygen deficient regions appear more prominently in and around the high-contrast regions and align vertically toward the bottom interface to form highly oxygen deficient region with an average width of 35 nm.

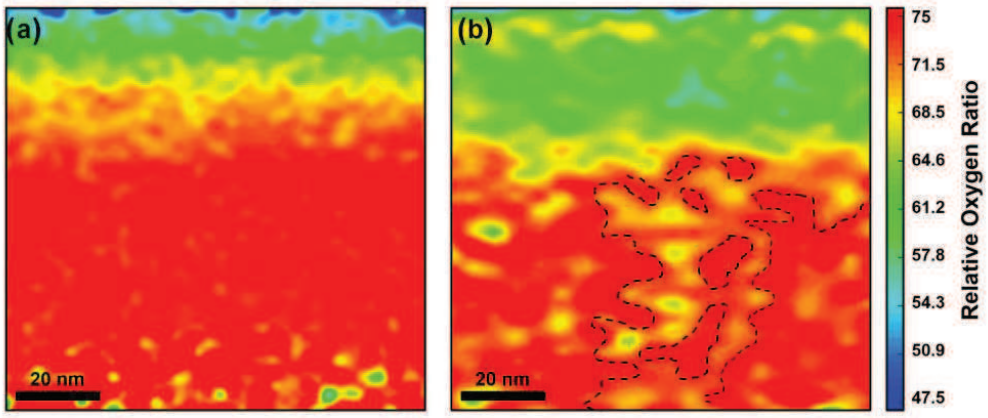

Figure 3.2 Relative oxygen ratio maps for representative scan areas in (a) virgin and (b) switching *a*-STO$_x$ device cross-sections. The ratio was calculated from the area under Ti-$L_{2,3}$ and O-*K* ionization edges for each pixel in survey scan images.

3.2.3 Composition of nano-filamentry networks

For HR-TEM investigations, ROIs were chosen based on the similar contrast profile in STEM-EELS studies. Virgin cross-sections were found to be uniform and amorphous with no evidence of crystalline grains. In contrast, switching cross-sections exhibited

distinct localized crystalline grains, especially in the high-contrast regions, scattered within the amorphous oxide (**Figure 3.3**). The crystal structure of these vertically aligned regions (**Figure 3.4**a and 3.4b) is complex and varying strong and reflections in respective fast Fourier transform (FFT) exist throughout the region. Assuming a predominant crystallization to the perovskite phase,[80, 83, 84] several strong and recurrent reflections can be assigned to the cubic STO phase (Figure 3.4b).

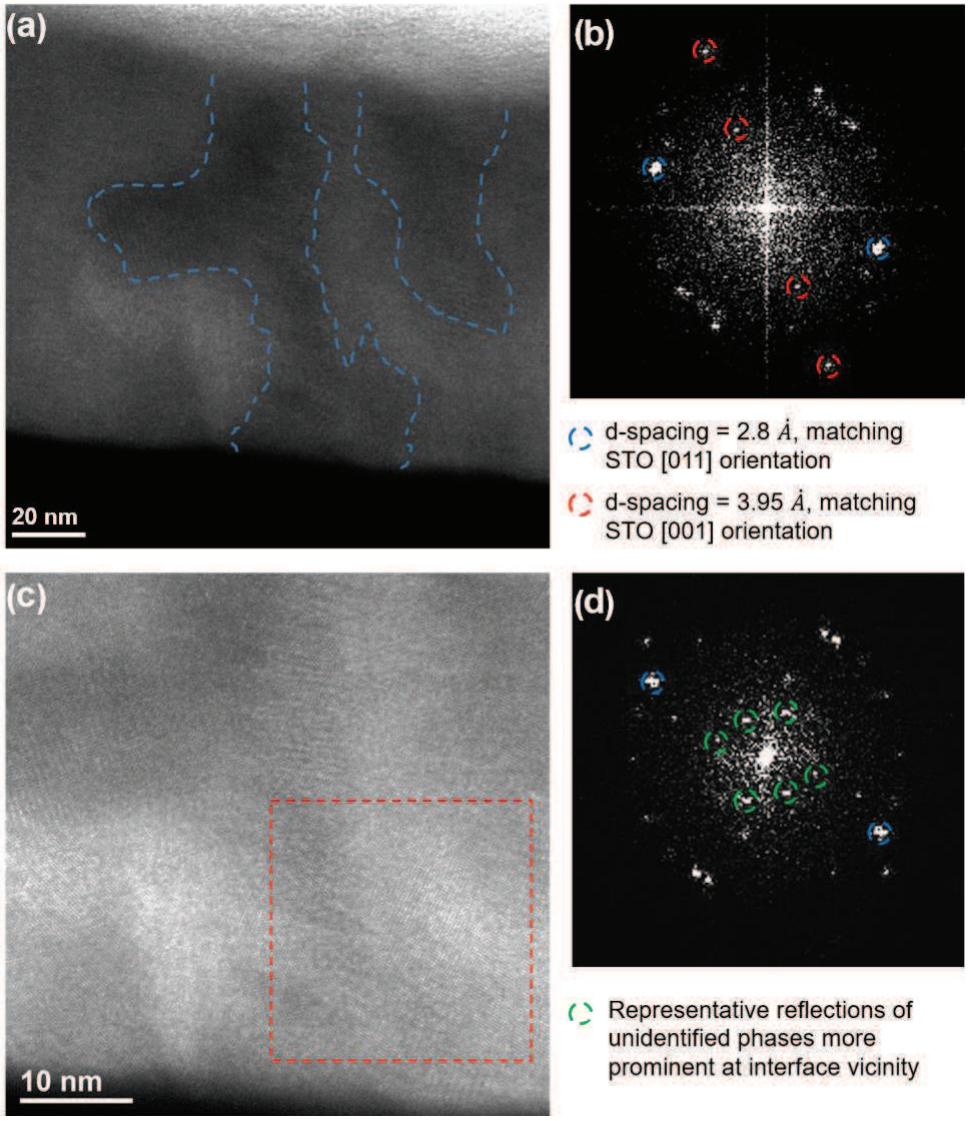

Figure 3.3 (a) HR-TEM micrograph of a possible filamentary region in a switching Nb:*a*-STO_x device cross-section. (b) FFT image for the crystalized region enclosed in blue dashed line in (a); blue and red circles denote reflections that can be assigned to STO cubic phase based on their d-spacing. (c) Magnified micrograph of a crystallized region near the bottom interface and (d) the corresponding FFT image for the region enclosed in red dashed line in panel (c); green circles denote un-identified (possibly titanium oxide subspecies) phases.

However, there exist several secondary reflections (recurring more frequently at the bottom interface vicinity) that cannot be resolved based on current information. Considering secondary phase and compositional evidence from XPS and EELS investigation, these reflections might indicate the formation of segregated titanium oxide phases within the disordered *a*-STO_x network. However, current measurements did not signal any segregation of A-site and B-site cations in Nb:*a*-STO_x devices and more refined studies are required to unambiguously ascertain the nature of secondary phases.

These results help complete the picture of localized nano-filamentary switching processes in Nb:*a*-STO_x devices and provide further support for their scalability prospects. During the electroforming step, Joule-heating assisted electrochemical redox processes, form a network of highly reduced and (at least partially) crystallized conductive filamentary pathways through the amorphous oxide phase. Field-dependent oxygen vacancy migration across the nano-filamentary network determines the resistive switching processes in Nb:*a*-STO_x devices. While oxide phase and compositional engineering ensures an improved and reliable switching performance, engineering switching interface properties to control interfacial defect hotspots is crucial for achieving low variation and uniform device performance.

3.3 Electrical characterization of Nb:*a*-STO_x devices

3.3.1 Temperature dependent switching performance of Nb:*a*-STO_x devices

Although the structural and compositional effects of Nb dopant species could not be confirmed in TEM studies due to their extremely low concentrations, temperature dependence of switching characteristics can provide valuable insights into the role of substitutional species. Figure 3.4a and 3.4b show the bipolar switching and resistive state retention of Nb:*a*-STO_x devices, respectively, in the temperature range of 300-398 K. Maximum low resistance state (LRS) conductivity loss is 3.1% over 10^5 s at 398 K (Figure 3.4b) with a minimum switching ratio of 32. The evolution of LRS conductivity under READ bias (100 mV) over a wide temperature range up to 398 K closely follows typical Arrhenius behaviour, as depicted in Figure 3.4c. On the other

hand, a biphasic Arrhenius behavior for high resistance state (HRS) conductivity indicates a temperature-dependent increase in electronic conduction at the donor sites, similar to that observed in acceptor-doped STO ceramics at elevated temperatures.[85-87].

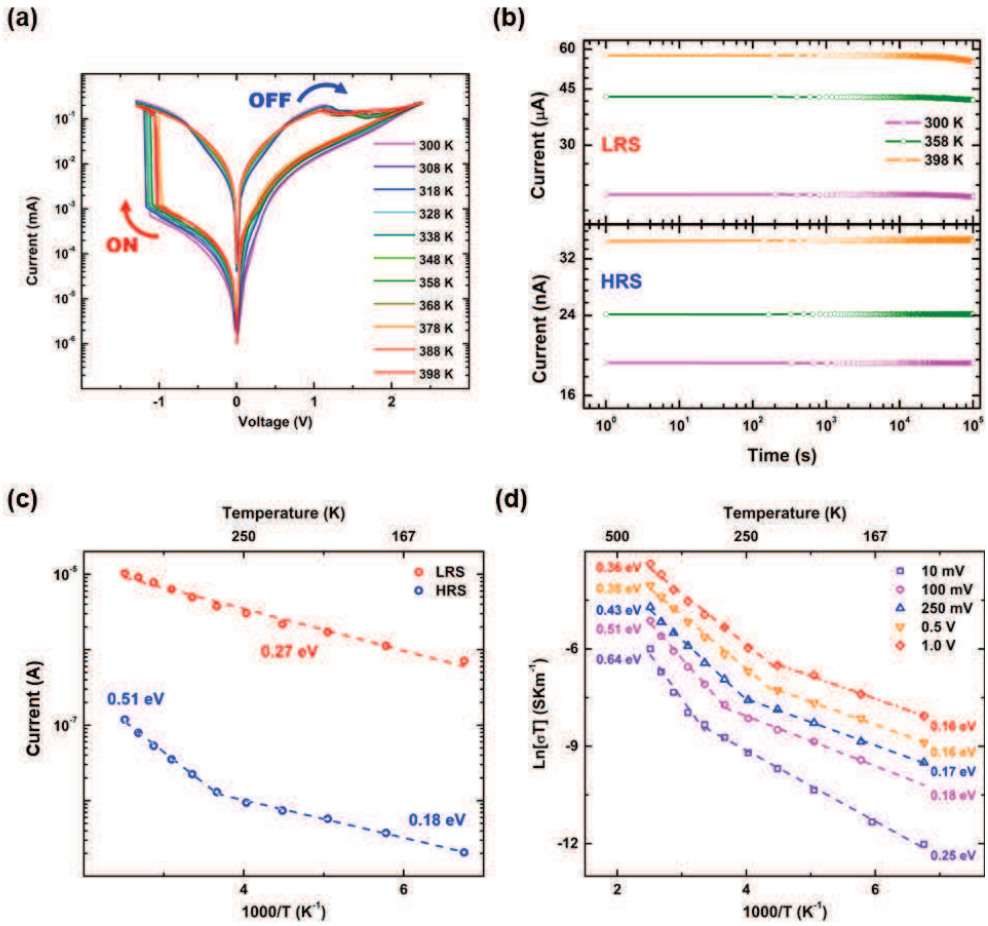

Figure 3.4 (a) Bipolar switching behavior of electroformed Nb:*a*-STO_x devices in the temperature range of 300-398 K (log-linear plot). (b) Room and elevated temperature HRS and LRS stressed retention over 10^5 seconds. (c) Arrhenius plots of the evolution of cell current under READ (100 mV) bias and (d) Arrhenius plots of HRS conductivity under increasing biases in the temperature range of 148-398 K.

To further investigate the origin of the biphasic behavior and its correlation with the stable multi-state OFF transition in Nb:*a*-STO_x devices, temperature-dependent HRS conductivity measurements are repeated under different forward bias (Figure 3.4d). Except for 10 mV bias, which essentially falls in the linear sub-threshold region of the rectifying Pt/Nb:*a*-STO_x barrier in HRS regime, cell conductivities exhibit similar thermal activation energies in the lower temperature range for all bias values. The

conduction in this regime is mainly governed by the electronic transport across the rectifying barrier,[69, 70, 88] where the barrier inhomogeneities and short range trap sites have insignificant impact on the cell conductivity.

The non-linear deviation in the higher temperature regime is likely to originate from conduction enhancement along highly resistive donor sites.[70, 85, 86] The onset of biphasic behavior in Nb:*a*-STO_x has a clear field dependency, shifting to lower temperatures and exhibiting lower thermal activation energies for higher biases. Although the origins of highly resistive grain boundaries in heavily donor- and acceptor-doped STO are different,[87, 89] the current transport across donor dislocation sites with small concentrations in electroformed Nb:*a*-STO_x devices can be explained in a similar manner. The thermally-activated enhancement in conduction across the donor sites is assumed to originate from an increased electron concentration.[85, 87] The field dependence of the onset temperature and activation energies in the higher temperature range can be explained in terms of a reduction in the barrier potential at localized donor sites. Large barrier drops (due to higher electrical fields) reduce the energy requirement for carrier transport across the donor sites which explains the lower onset temperature and activation energies in the Nb:*a*-STO_x devices.[85, 90] A more extensive analysis of the interplay between applied energy and current transports across the oxygen vacancy related defect sites can therefore be instrumental in outlining the external stimulus criteria for an effective control over the current transport in switching cells.

These results further clarify the origin of stable intermediate resistive states during the RESET transition in Nb:*a*-STO_x devices.[70] The RESET transition involves rupture of the filamentary conduction network at the vicinity of the switching interface. An instantaneous partial RESET bias (greater than ~55% of the full RESET threshold) should result in partial degradation of the filamentary network. In the absence of deep level donor trap sites, an increase in the overall RESET stress ultimately results in the full rupture of conduction network at the interfacial region. On the other hand, at the core of donor-induced dislocation sites, the initial high field induced barrier drop at the grain boundary facilitates the injection and accumulation of oxygen vacancies which re-stabilizes the localized donor-induced barrier and limits further redox reactions at its vicinity [85, 86, 91] Therefore, a more robust control over these equilibrium energy states (and consequently the number and relative ratios of intermediate states) can be achieved *via* increasing the quality of switching interface and/or tuning the concentration and distribution of donor dislocations.

3.3.2 Charge transportation in Nb:a-STO$_x$ devices

The complex electronic structure of Nb:a-STO$_x$ devices and stability of their switching processes can provide a powerful toolbox for a wide range of applications from high density memory structure to adaptive and neuromorphic computation. To access the intermediate switching states and charge transport mechanism in the Nb:a-STO$_x$ devices, an approach to probe the bias and time dependence of the SET transition is adopted.[70] A partial SET voltage with (>40% of the average SET bias) was held constant on devices in their HRS state for 60 min steps, as shown in **Figure 3.5**a. After each step, the state retention was monitored for 10^4 seconds (plotted in Figure 3.5b). For partial SET biases below 65% of the average SET threshold, the conductance versus time characteristics represent a decay function ($d|I|/dt < 0$) and the device conductance eventually settles to stable HRS levels. For voltages greater than 70% of the SET threshold, the initial $d|I|/dt > 0$ regime, characterized as the SET transition,[92] saturates to a stable level ($d|I|/dt \approx 0$). It should be noted that the SET transition is triggered by the bias dependent drift diffusion of charged ionic species (*i.e.*, vacancies) under a large electrical gradient and is characterized by ($d|I|/dt > 0$). Since the bias dependent ionic diffusion accelerates under increasing bias, the slope of positive current differential in the SET transition increases with increased bias.

Furthermore, the utility of bias/time dependence together with dynamically tunable states in Nb:a-STO$_x$ devices is demonstrated *via* a simple routine illustrated in Figure 3.5c. The device is first set to an intermediate HRS level by applying a partial (65% - 90%) 500 μs RESET pulse, and then undergoes three 500 μs SET pulses with an amplitude of 0.7 V (about 65% of the average SET bias). Following each pulse, the device conductance is monitored for a period of 100 s. The results clearly show the bias/time and state dependence of conductance and transient behaviors in Nb:a-STO$_x$ devices. These results suggest the utility of energy (bias/time) dependent non-volatile and semi-volatile transitions in a-STO$_x$ based devices for implementation of adaptive computation and bio-inspired plasticity functions.[55, 93] As such, detailed investigations of dynamic switching behaviors and implied plasticity in a-STO$_x$ devices are extensively studied in the following chapters.

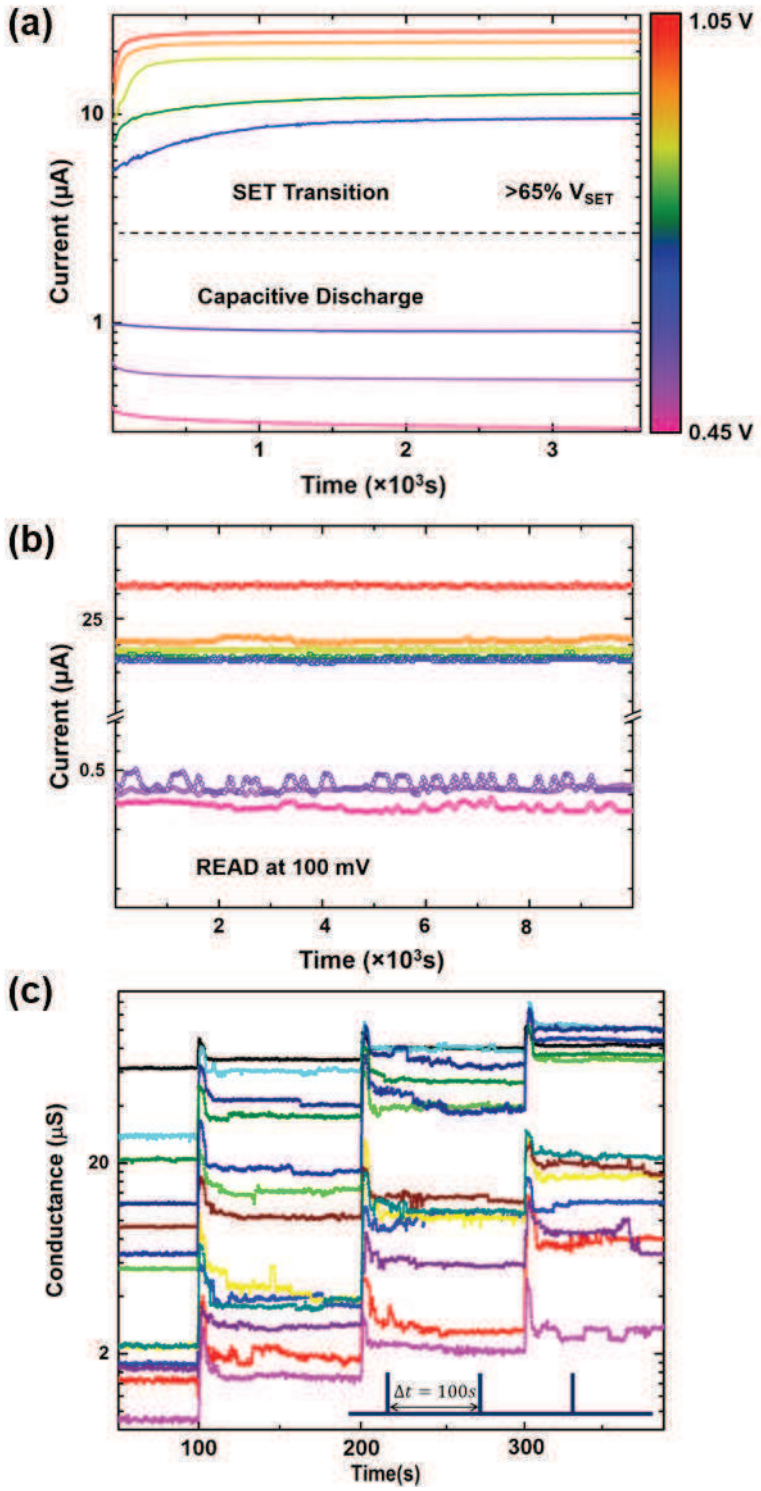

Figure 3.5 (a) Long bias partial SET measurements on Nb:*a*-STO_x devices in complete OFF state. Partial bias amplitudes are varied from 40-95% (shown as various colors) of the average SET voltage (1.1 V). (b) Current retention at READ bias over 10^4 s after each long bias step, where colors correspond to the bias steps in (a). (c) Device excitation response at different conductance levels to 500 μs pulses with 0.7 V amplitude.

4 Multiple switching behaviors

The adaptation of a single memory cell to exhibit different switching characteristics is an important step in harnessing the full suite of capabilities that resistive memories have to offer. This chapter presents the multiple (threshold and bipolar) switching behaviors achieved in selectively chromium-doped a-STO_x memory cells. Extensive electrical and material characterizations are carried out to investigated the switching kinematics of the multiple resistive switching behaviors.

4.1 Introduction

Transition metal oxides are known to exhibit valance change mechanism (VCM) and have demonstrated diverse switching behaviors – namely, unipolar, bipolar (BP) and complementary resistive switching (CRS) – which highlights the complex nature of VCM.[94-100] Among the transition metal oxides, the STO-based resistive memories are known to exhibit bipolar (BP) resistive switching behavior, [3, 28, 98, 101, 102] but there are few reports demonstrating the transition between unipolar and BP resistive

switching behaviors in a single STO-based memory cell.[103, 104] Moreover, no clear and direct evidence is available that elaborates the driving mechanisms for this versatile functionality. Therefore, to achieve and precisely control the existence of more than one switching behaviors in the perovskite STO-based systems, insights into the structural and electrochemical factors are important to understand the multifunctional switching behaviors.

In this chapter, the presence of BP (clockwise and counter-clockwise) and threshold (CRS and "*peculiar*" CRS) resistive switching behaviors in single units of chromium-doped *a*-STO_x (Cr:*a*-STO_x) memories are presented. The distinct resistive switching behaviors are permanently induced by the current compliance limit and applied bias polarity during the initial electroforming step. Through detailed compositional and electrochemical analyses of the Cr:*a*-STO_x MIM devices, the observed multiple resistive switching behaviors are attributed to the distribution and concentration of oxygen vacancies generated, and their drift/diffusion under the influence of set current compliance. It is also observed that the locally-created crystalline regions (formed by the Joule heating) provide a localized conductive path for the anionic-electronic transport across the asymmetric switching MIM cell. Finally, based on the electrical and material characterization, a physical mechanism is suggested to interpret the switching kinematics of the presented multiple resistive switching behaviors.

4.2 Characterization of Cr:*a*-STO_x thin films

Figure 4.1a illustrates a schematic of the Cr:*a*-STO_x based MIM device fabricated in a cross-point structure where a stack of Ti (8 nm)/Cr:*a*-STO_x (25 nm) is sandwiched between Pt electrodes. In order to evaluate the chemical composition of sputtered Cr:*a*-STO_x thin films, comparative compositional analysis is carried out between Cr-doped and un-doped *a*-STO thin films by using high resolution X-ray photoelectron spectroscopy (XPS)(Appendix E). The core-level XPS spectra of Ti 2*p* from Cr:*a*-STO_x (Figure 4.1b) show two spin-orbit pairs (with splitting of ~5.3 eV) and reveal the presence of two oxidation states *i.e.*, Ti^{4+} and Ti^{3+} corresponding to the binding energies of 458.23 eV and 456.22 eV (both $2p_{3/2}$), respectively.[70, 105] In addition, the core-level spectra of O 1*s* and Sr 3*d* show the presence of O^{2-} and Sr^{2+} oxidation states, respectively (Appendix B). The resolved spectra of Cr $2p_{3/2}$ (Figure 4.1c) show two

peaks at 576.72 eV and 579.91 eV which can be assigned to Cr^{3+} and Cr^{6+} oxidation states, respectively.[106-108] It has been reported that doping of Cr in STO can either incorporate the Cr ions at Ti or Sr sites.[107, 108] In the Cr:*a*-STO_x thin films, a shift in the Ti 2*p* peaks (Figure 4.1b) towards lower binding energies (by ~0.16 eV), as compared to the un-doped oxygen deficient *a*-STO_x (Appendix B), together with the presence of Cr^{6+} species suggest that the Cr doping mainly affects the Ti sites in Cr:*a*-STO_x.[107, 108] Also, the Cr^{6+} prefers to accommodate at the Ti-site instead of Sr-site. This is because the ionic radius of Cr^{6+} (0.0440 nm) is similar to that of Ti^{4+} (0.0605 nm). In contrast, the ionic radius of Sr^{2+} (0.1180 nm) is much larger, which does not satisfy the limits of tolerance factor defined by Goldshmidt to retain the structure of an ABO_3-type complex oxide.[108] Furthermore, the substitutional Cr doping in *a*-STO_x with a low concentration (Cr/Ti ≈ 0.025) is not expected to distort the chemical structure of *a*-STO_x perovskite oxide.[109]

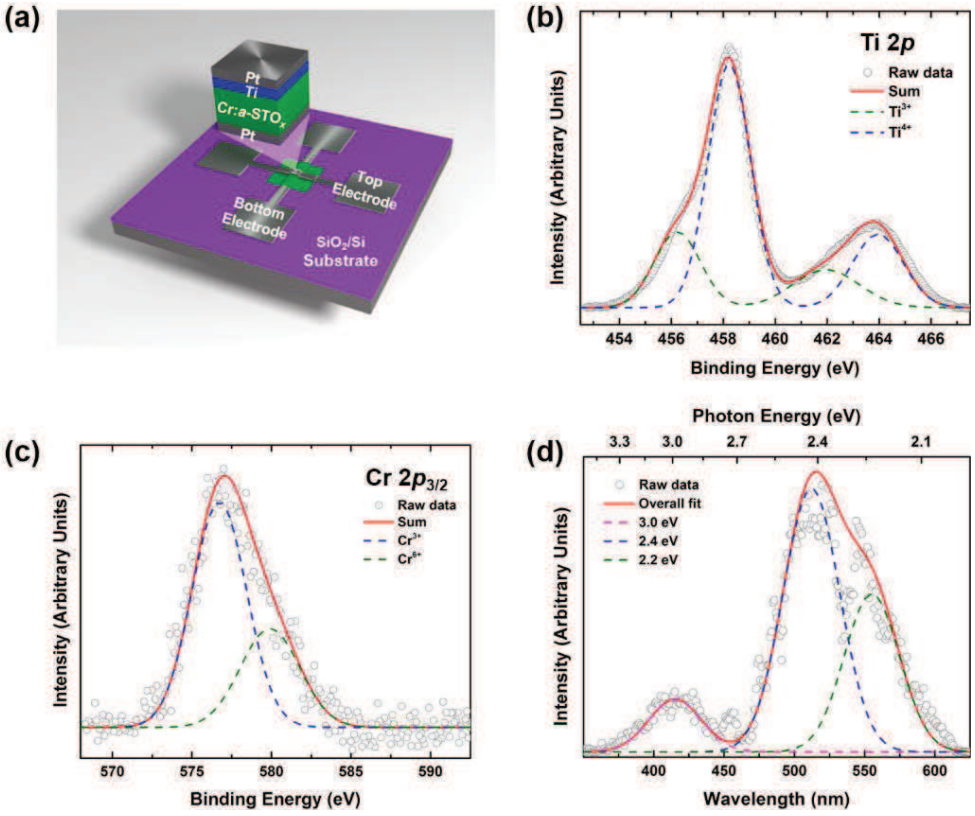

Figure 4.1 Device structure and functional oxide characterization. (a) Schematic illustration of a cross-point Cr:*a*-STO_x MIM device. The XPS core-level spectra of (b) Ti 2*p* and (c) Cr $2p_{3/2}$. (d) Photoluminescence spectra of Cr:*a*-STO_x collected at an excitation wavelength of 325 nm.

The electronic structure of Cr:*a*-STO_x is assessed by obtaining the photoluminescence (PL) spectra at room temperature using a 325 nm (3.82 eV) laser excitation source. Figure 4.1d shows the PL spectra obtained from bare Cr:*a*-STO_x thin films. A high intensity broad peak, centered at 535 nm (2.32 eV) was observed which could be de-convoluted into multiple emission bands. Such a broad emission at room temperature is characteristic of doped[110, 111] and un-doped *a*-STO thin films.[112-114] In un-doped *a*-STO thin films, room temperature PL emission is associated with the presence of TiO_5 defects.[111, 113, 114] On the other hand, Cr is known to modify the electronic structure of STO by forming CrO_5 defect structures with V_os and introducing in-gap electronic states above the valance band edge.[108, 111, 115-117] The emission energy of 2.32 eV in Cr:*a*-STO_x (Figure 4.1d) is comparatively lower than that of the un-doped *a*-STO_x (by 0.94 eV) at the same excitation energy[110] which indicates the presence of in-gap electronic states in Cr:*a*-STO_x. The XPS and PL analyses suggest that a low concentration Cr doping (Cr/Ti ≈ 0.025) in *a*-STO_x, primarily influences the Ti sites, resulting in oxygen deficient [TiO_5V_o] and [CrO_5V_o] complexes that give rise to the in-gap electronic states.[111] Consequently, the introduction of these additional states can offer the possibility of manipulating the switching behaviors of the Cr:*a*-STO_x MIM devices using different applied electric fields, which is discussed later in the manuscript.

4.3 Resistive switching in Cr:*a*-STO_x MIM devices

In order to activate the resistive switching in the STO based MIM devices, usually an initial high voltage sweep (higher than the subsequent switching threshold voltages) is required as an electroforming step which creates extended defects (*i.e.*, nanofilament) through redox processes in the oxide.[6, 28, 70, 98] In Cr:*a*-STO_x MIM devices, the multiple resistive switching characteristics have been achieved (regardless of the device area) by controlling the initial bias polarity and current compliance during the electroforming process (Appendix B).

4.3.1 Threshold switching

4.3.1.1 Complementary resistive switching

The complementary resistive switching (CRS) is considered as one of the possible solutions to eliminate the sneak currents in a passive crossbar array for high density memory integration.[118] The Cr:*a*-STO_x MIM devices electroformed at low current

compliances (in the range 1-5 μA, see Appendix B) exhibit CRS behavior, as depicted in **Figure 4.2**.

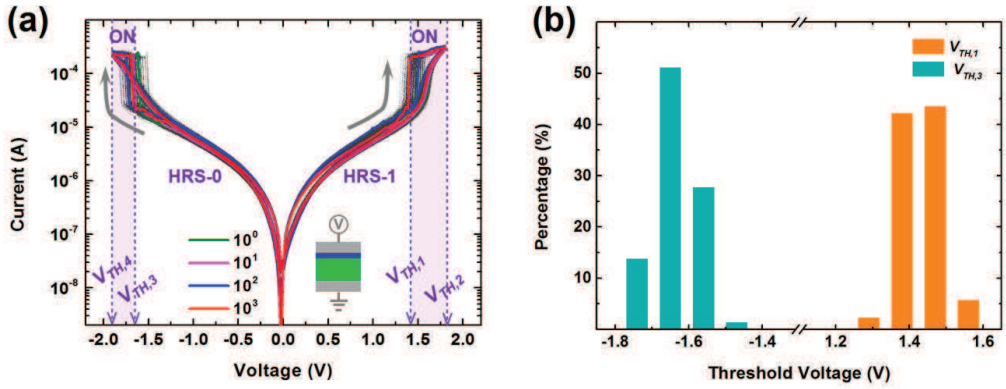

Figure 4.2 Complementary resistive switching behavior of the Cr:*a*-STO$_x$ MIM devices. (a) The CRS characteristics are repeated for 1000 cycles, while 1st, 10th, 100th, and 1000th cycles (green, magenta, blue, and red lines, respectively) are highlighted. Inset shows the biasing scheme during CRS switching cycles. (b) Statistic histograms of the CRS threshold voltages, under positive ($V_{TH,1}$, orange bars) and negative ($V_{TH,3}$, cyan bars) voltages for 1000 cycles.

A commonly known CRS cell comprises of two BP switching cells connected anti-serially through an intermediate electrode (in a tri-layer structure) and each cell can be reversibly switched between low resistive state (LRS) and high resistive state (HRS) under opposite applied voltage polarities. Unlike bipolar characteristics where two resistive states (HRS and LRS) define the device state, three states HRS-1, HRS-0, and ON represent the different configurations of the resistive states in the CRS operation.[99, 118] Both HRS-1 and HRS-0 states give high resistance at low READ voltages (V_{READ}) than a certain threshold voltage (which is an intrinsic property of the CRS mechanism to suppress sneak currents in a memory array) while ON state gives low device resistance at high V_{READ}.

In Cr:*a*-STO$_x$ MIM devices, transition of resistive states from HRS-1 to ON and from ON to HRS-0 occurs at positive threshold voltages during cyclic voltage sweeps and are denoted by $V_{TH,1}$ and $V_{TH,2}$, respectively, as shown in Figure 4.2a. Similarly, the transition from HRS-0 to ON and from ON to HRS-1 occurs at negative threshold voltages as denoted by $V_{TH,3}$ and $V_{TH,4}$, respectively. In CRS, both HRS-1 and HRS-0

are regarded as HRS at low V_{READ} (between $V_{TH,3}$ and $V_{TH,1}$) whereas ON is a transition state (between HRS-1 and HRS-0) that separates resistive states at higher V_{READ} (such as $V_{TH,1} < V_{READ} < V_{TH,2}$ or $V_{TH,3} < V_{READ} < V_{TH,4}$)[99, 118]. Figure 4.2b shows the statistical distribution of $V_{TH,1}$ and $V_{TH,3}$ for 1000 cycles and the average values are calculated to be 1.43 V and -1.65 V, respectively.

4.3.1.2 *Peculiar* complementary resistive switching

In a conventional readout operation of CRS devices, generally a higher V_{READ} (than transitional thresholds $V_{TH,1}$ and $V_{TH,3}$) is required, as the stored states (HRS-1 and HRS-0) cannot be distinguished at lower V_{READ}. This can change the resistive state of the CRS device and re-writing of the resistive state is required as a result of the destructive readout operation.[119, 120] Interestingly, the Cr:*a*-STO_x MIM devices, electroformed at moderate current compliance limits (in range 10-15 μA, Appendix B), show a reproducible *"peculiar"* CRS (*p*-CRS) behavior Figure 3a., where the stored resistive states can be distinguished at lower read voltage (*i.e.*, $V_{READ,1}$) in a non-destructive readout. The prominent feature of *p*-CRS (as compared to the conventional CRS) is the possibility of three-level memory states where LRS, HRS and ON can be distinctively stored in a single cell and the inherent switchable diode characteristics of *p*-CRS can facilitate the implementation of complete logic operations.[121] As depicted in **Figure 4.3**a, the devices switch the states from LRS to ON at $V_{TH,1}$ and from ON to HRS at $V_{TH,2}$. Also the transition from HRS to ON occurs at $V_{TH,3}$ and ON to LRS at $V_{TH,4}$. The average values of transition thresholds $V_{TH,1}$ and $V_{TH,3}$ are calculated to be +1.45 V and -1.35 V, respectively, from their statistical distribution (Figure 4.3b) and the values of $V_{TH,2}$ and $V_{TH,4}$ are +1.8 V and -1.8 V, respectively.

Figure 4.3c shows the retention of the *p*-CRS regime for 10^5 s. A constant $V_{READ,1}$ of +0.2 V and $V_{READ,2}$ of +1.6 V are used to measure the HRS/LRS and ON state resistances, respectively. Distinguishable HRS and LRS with an average switching ratio (HRS/LRS) of ~9 suggests the capability and stability of bi-level storage of the *p*-CRS behavior in Cr:*a*-STO_x MIM devices. Figure 4.3d shows the endurance characteristics of the *p*-CRS regime for <5000 switching cycles. The loss of resistive states after 4.3×10^3 cycles can be attributed to the cycling-induced degradation due to relatively higher $V_{READ,2}$ and dual V_{SET} pulses in each cycle (as depicted inset of Figure 4.3d).[122, 123] During the endurance measurements, a train of short pulses with a duration of

50 µs are used to WRITE/ERASE/READ the devices (inset of Figure 4.3d) For each complete WRITE/ERASE/READ cycle, a positive pulse with an amplitude of +2.3 V switches the devices to HRS followed by a $V_{READ,1}$ pulse with an amplitude of +0.2 V. A negative pulse of -2.3 V amplitude switches the devices to LRS/ON followed by $V_{READ,1}$ (+0.2 V) and $V_{READ,2}$ (+1.6 V) pulses to READ the LRS and ON states, respectively. Finally, a second negative pulse of -2.3 V is required to restore the LRS/ON states, prior to the next cycle. The *p*-CRS characteristics are evaluated for more than 15 devices which reveal that Cr:*a*-STO$_x$ MIM devices exhibit reproducible *p*-CRS behavior (Section S2, Appendix B).

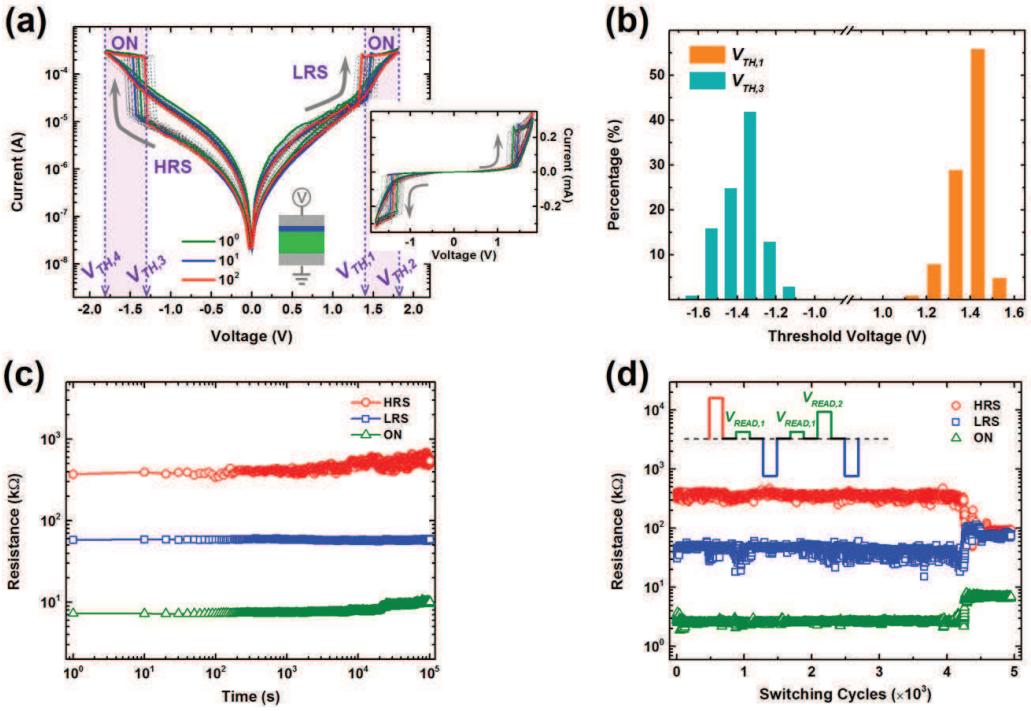

Figure 4.3 *Peculiar* complementary resistive switching of the Cr:*a*-STO$_x$ MIM devices. (a) Characteristic *I*–*V* sweeps for 100 cycles. 1st, 10th, and 100th cycle (green, blue, and red lines, respectively) are highlighted. Inset shows *I*–*V* sweeps of 100 cycles on a linear scale along with the bias scheme. (b) Statistic histograms of $V_{TH,1}$ (orange bars) and $V_{TH,3}$ (cyan bars) for 100 *p*-CRS switching cycles. (c) The retention performance of LRS and HRS measured at constant $V_{READ,1}$ of +0.2 V and ON resistive state measured at constant $V_{READ,2}$ of +1.6 V for 10^5 s. (d) The endurance of *p*-CRS threshold switching for <5000 cycles. Inset shows a train of pulses in a complete switching cycle where each pulse has duration of 50 µs.

4.3.2 Bipolar resistive switching

As depicted in **Figure 4.4**, two different electroforming-polarity dependent BP resistive switching behaviors (see Appendix B) are observed in Cr:*a*-STO_x MIM devices. Both BP resistive switching behaviors are induced at higher current compliances than the CRS and *p*-CRS during the initial electroforming step. While applying positive bias on the top electrode, the electroforming processes with current compliance in 40-100 μA range, sets the Cr:*a*-STO_x MIM devices into the clockwise BP (CW-BP) resistive switching regime.

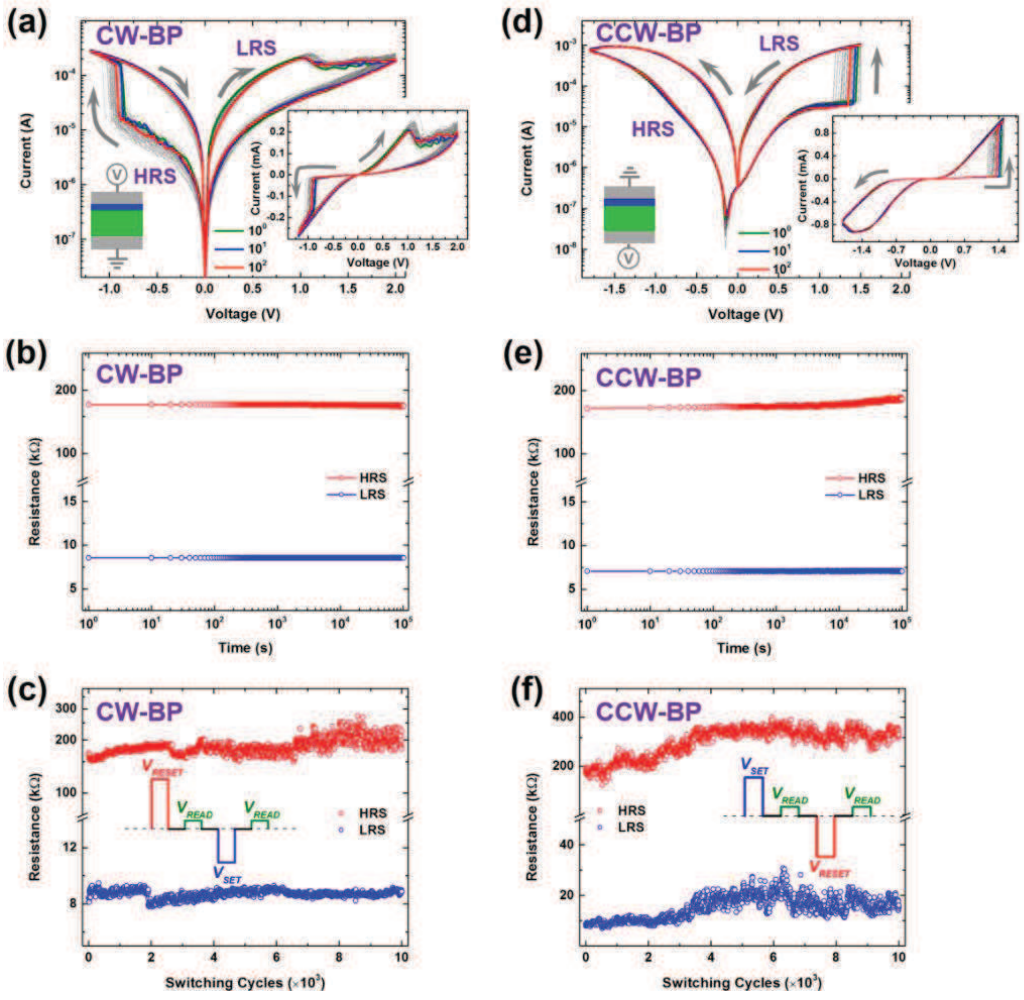

Figure 4.4 Electroforming polarity-dependent bipolar resistive switching behavior of the Cr:*a*-STO_x MIM devices. (a) Characteristic *I–V* sweeps of CW-BP resistive switching for 100 cycles, where the representative 1st, 10th, and 100th cycle (green, blue, and red line, respectively) are highlighted. Inset shows the biasing scheme and *I–V* sweeps for 100 cycles on a linear scale. (b) Retention performance of CW-BP resistive switching behavior for 10^5 s under a constant V_{READ} of +0.2 V. (c) Endurance of CW-BP

resistive switching for 10^4 switching cycles. Inset depicts a schematic of a switching cycle where V_{RESET} of +3 V, V_{SET} of -2.7 V and V_{READ} of +0.2 V are applied as short pulses each with the duration of 50 μs. (d) The characteristic *I–V* sweeps of CCW-BP resistive switching for consecutive 100 cycles, the representative 1st, 10th and 100th cycle (green, blue and red line, respectively) are highlighted. Inset shows the biasing scheme and *I–V* sweeps for 100 cycles on a linear scale. (e) Retention performance of CCW-BP resistive switching behavior for 10^5 s under a constant V_{READ} of +0.2 V and (f) endurance of CCW-BP resistive switching for 10^4 switching cycles. Inset depicts a schematic of a switching cycle where pulses of 50 μs duration (as V_{SET} of +2.4 V, V_{RESET} of -3 V and V_{READ} of +0.2 V) are applied.

Figure 4.4a shows repeatable and well-defined CW-BP switching cycles which are a signature of *a*-STO devices (RESET on positive bias and SET on negative bias).[70, 98] Figure 4b show stable retention characteristics for 10^5 s with an average switching ratio (HRS/LRS) of ~19 at a constant V_{READ} of +0.2 V. Figure 4.4c the endurance of the MIM devices (preset into CW-BP switching behavior) for 10^4 cycles. On the other hand, applying positive bias on the bottom electrode during the electroforming process (with current compliance in 40-100 μA range) induces a counter-clockwise BP (CCW-BP) resistive switching (Figure 4.4d). The retention of CCW-BP switching behavior is measured for 10^5 s (Figure 4.4e) and shows no degradation with an average switching ratio of ~25 at a constant V_{READ} of +0.2 V. Figure 4.4f shows endurance of CCW-BP switching behavior for 10^4 cycles.

The existence of multiple resistive switching behaviors (in identical MIM devices) suggests that the intrinsic Schottky contact at the bottom Cr:*a*-STO_x/Pt interface[5, 124] and an expected Ohmic contact at the top Pt/Ti/Cr:*a*-STO_x interface [125] are modified under the influence of different current compliance limits and applied polarities during the electroforming step.[126] The oxidation of the top Ti layer into a sub-stoichiometric titanium oxide (as discussed in the following sections) introduces another functional switching layer at the top interface which contributes in defining and executing the multiple resistive switching behavior. In order to understand the role of the top Ti layer, symmetric Pt/Cr:*a*-STO_x/Pt MIM devices were fabricated (Appendix B). Regardless of the current compliance and applied polarity during the initial electroforming, no significant and well defined resistive switching characteristics are observed. This further

indicates that the presence of Ti at the top interface renders Cr:*a*-STO_x MIM devices with the asymmetry which is responsible for the observed multiple resistive switching behaviors.

4.4 Spectroscopic analyses of the Cr:*a*-STO_x MIM devices

4.4.1 Secondary ion mass spectroscopy (SIMS)

In the electroforming process, isolated incomplete filaments can simultaneously be formed over the electroforming cathode along with a fully extended nanofilament in a MIM device (Appendix B). A depth profile analysis can indicate the switching mechanism through the distribution of principal elements, without distorting their oxidation states, throughout the thickness of MIM device. The dynamic secondary ion mass spectroscopy (SIMS) depth profiles are used to assess the distribution of principal elements across the Cr:*a*-STO_x MIM devices.. The raw depth profile data, shown in **Figure 4.5**, depicts the distribution of O^-, TiO^-, SrO^- and CrO^- species across three different MIM devices in three different states, namely – pristine, LRS and HRS, as a function of sputtering time during analyses. Also, the switching MIM devices were pre-set to exhibit CW-BP resistive switching behavior and subjected to *I–V* switching cycles (at least 100 cycles). An increase in signals for the O^- and TiO^- species at the top Ti/Cr:*a*-STO_x interface of the pristine MIM device indicates the partial oxidation of the Ti layer. This is consistent with cross-sectional compositional analyses (discussed in the following section) and earlier XPS depth profile analyses of the switching MIM devices.[70] The O^- profile in the pristine and LRS shows a uniform distribution of oxygen across the Cr:*a*-STO_x layer. However, for the device set in the HRS, the O^- profile clearly shows that the oxygen content drops at the bottom Cr:*a*-STO_x/Pt interface. This indicates that in HRS relatively more V_os accumulate at the vicinity of the bottom electrode than the top interface. The relative differences in LRS and HRS profiles suggest that the drift of V_os under the reverse bias polarities and nano-redox reactions induce the change in resistive states.[28, 38, 127, 128]

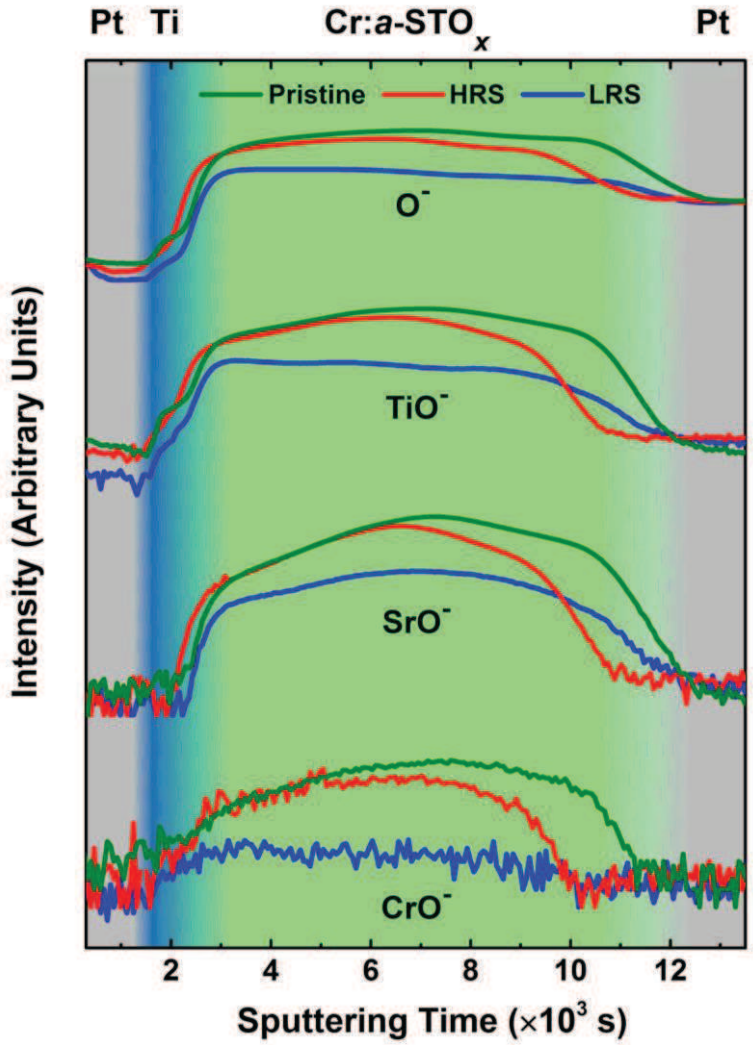

Figure 4.5 Nano-SIMS depth profile of the pristine and CW-BP resistive switching Cr:*a*-STO$_x$ MIM devices. The elemental profiles are obtained across the MIM devices in their pristine state (green lines), HRS (red lines), and LRS (blue lines).

4.4.2 Cross-sectional structural and compositional analyses

In order to establish the resistive switching mechanism in the Cr:*a*-STO$_x$ MIM devices, high resolution transmission electron microscope (HR-TEM) and electron energy loss spectroscopic (EELS) analyses are carried out. As expected, the TEM micrographs of the pristine MIM device show an amorphous microstructure of the functional oxide layer along the length of the device cross-sections, owing to the room temperature sputtering of Cr:*a*-STO$_x$ thin film (Appendix B). Also, the cross-sectional EELS analysis of the pristine MIM device reveals the partial oxidation of the top Ti layer and

presence of a sub-stoichiometric titanium oxide layer at the top Ti/Cr:*a*-STO_x interface (Appendix B).

The HR-TEM micrographs of the MIM devices exhibiting BP resistive switching characteristics illustrate the presence of localized crystalline regions in the functional Cr:*a*-STO_x layer. To analyze the structure and composition of these localized crystalline regions and the metal/oxide interfaces, regions of interest (ROIs) were identified in the lamellae prepared from MIM devices preset into LRS. In the MIM devices exhibiting CCW-BP resistive switching behavior, a distinguishable high contrast ROI in the bulk amorphous functional oxide layer (highlighted in Figure 4.6a) is selected, which contains a crystalline region emanating from the bottom Pt electrode. Similar localized crystalline regions are also observed in MIM devices set to HRS of CW-BP behavior prior to TEM sample preparation (Appendix B). The fast Fourier transform (FFT) diffraction pattern (Figure 4.6b) of the ROI shown in Figure 4.6a is generated to determine the constituent phases of the crystalline structures. The high intensity diffraction spots marked as spot 1 and spot 2 in Figure 4.6b can be assigned to the cubic STO phase. Spot 1 with the *d*-spacing of 0.19 nm is used to generate the inverse FFT (Figure 4.6c) of the ROI which outlines the predominant existence of the [200] cubic STO phase in the Cr:*a*-STO_x layer. Spot 2 with the *d*-spacing of 0.21 nm matches the inter-planar spacing of [111] cubic STO and has a relatively less volume ratio. It should be noted that due to the instrumental limitations and experimental conditions we cannot exclude the presence of other sub-stoichiometric STO phases in the ROI [65, 129] (Appendix B).

Now, we assess the top interface. The ROI shown in Figure 4.6d depicts a crystalline region at the top Ti/Cr:*a*-STO_x interface of the switching MIM device set in a LRS prior to sample preparation. The respective FFT diffraction patterns (Figure 4.6e) are used to index the existing phase in the ROI. The highest intensity diffraction spot marked as spot 3, with the *d*-spacing of 0.21 nm, is used to outline the crystalline region in the inverse FFT micrograph (Figure 4.6f) and could be indexed to a [200] rhombohedral Ti_2O_3 phase. This suggests that the top Ti layer changes its microstructure from as-deposited amorphous to crystalline after the MIM devices are subjected to the electroforming (Appendix B) and subsequent switching cycles.[130, 131] Moreover, the electric field induced oxygen evolution in the Cr:*a*-STO_x layer and its diffusion into the Ti layer during continuous cyclic switching and electrical stress results in a gradual increase in the thickness of the sub-stoichiometric phase (such as Ti_2O_3) at the top

Ti/Cr:*a*-STO_x interface.[110, 132, 133] The formation of Ti_2O_3/Cr:*a*-STO_x oxide heterostructure explains the observed threshold resistive switching behavior in MIM devices, as discussed in the next section.

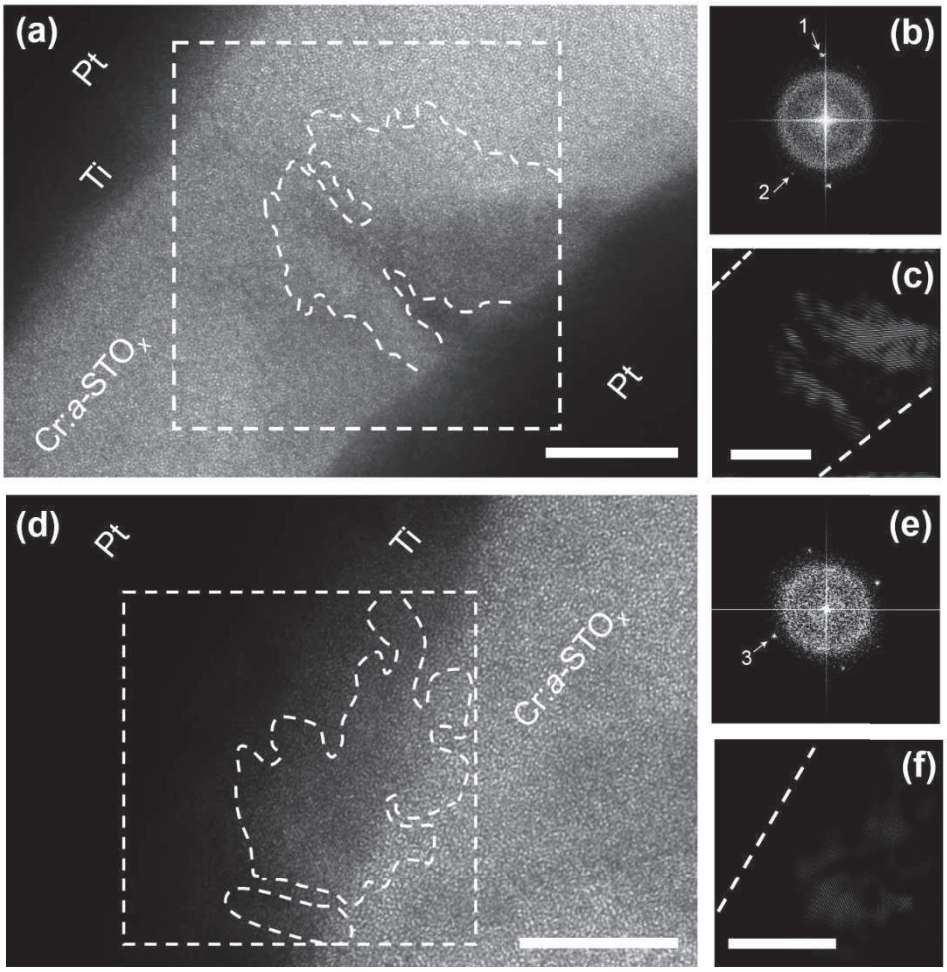

Figure 4.6 Morphological analyses of a representative Cr:*a*-STO_x MIM device cross-section from a device exhibiting CCW-BP resistive switching behavior and preset to LRS . (a) TEM micrograph of the MIM device subjected to at least 100 switching cycles and set to LRS prior to the lamella preparation. ROI is enclosed in the box. (b) The FFT diffraction patterns generated from the ROI in (a). (c) The inverse FFT obtained from spot 1 in (b) and highlighted on ROI in (a). (d) TEM micrograph of the top Pt/Ti/Cr:*a*-STO_x interface with ROI enclosed in the box.

To assess the relative differences in the electronic structure of the bulk amorphous and the locally crystalline ROIs, EELS spectra from cross-sectional line and area scans were acquired from switching devices. The fine structures of Ti–$L_{2,3}$ and O–*K* edges are used

to analyze the oxidation states of titanium and the distribution of oxygen content, respectively, across the MIM devices. Considering the instrument limitations, a qualitative analysis is carried out instead of quantifying the relative changes in the electronic structure. **Figure 4.7**a shows the EELS area map of the locally crystalline ROI (indicated in Figure 4.6a) to highlight the relative distribution of oxygen content across the MIM device after the cyclic CCW-BP switching. The EELS area map is generated by considering the O–*K* edge intensities of the collected spectra (at each pixel) after pre-edge background subtraction. It reaffirms the observations of the FFT analysis which showed that the Ti layer at the top Ti/Cr:*a*-STO_x interface (Figure 4.6e) oxidizes to sub-stoichiometric Ti_2O_3 phase due to the electrochemical redox reactions. The relatively lower oxygen concentration in the upper region of the ROI indicates the sub-stoichiometric nature (oxygen-deficient) of the top Ti/Cr:*a*-STO_x interface relative to the bottom Cr:*a*-STO_x/Pt interface. Furthermore, the oxygen deficient regions (*i.e.*, V_os) extending from top Pt electrode (acting as cathode), through the Cr:*a*-STO_x layer towards the bottom Pt electrode (acting as anode), indicate the filamentary path across the MIM structure in the LRS. Spatially isolated oxygen deficient hotspots in the bulk Cr:*a*-STO_x layer, identified in the EELS map, indicate the oxygen deficient stoichiometry of the functional oxide which is explained earlier in the XPS analysis (Figure 4.1). The presence of oxygen content within the top and bottom Pt electrodes can be attributed to the out-diffusion of oxygen ions along the Pt grain boundaries during the cyclic switching.[134, 135] In order to assess the distribution of V_os in the HRS of CW-BP behavior, the EELS area map of the ROI (Appendix B) shows the accumulation of V_os at the anode without their extension to the cathode (Appendix B). Based on the observed distribution of V_os in LRS and HRS, it can be inferred that the bias polarity induced migration of V_os and the associated formation and rupture of the oxygen deficient path is responsible for the switching in Cr:*a*-STO_x MIM devices. In the following section, we provide further evidence that indicates that these oxygen deficient pathways are the conductive routes for the charge transportation due to the change of Ti valance from Ti^{4+} to Ti^{3+}.

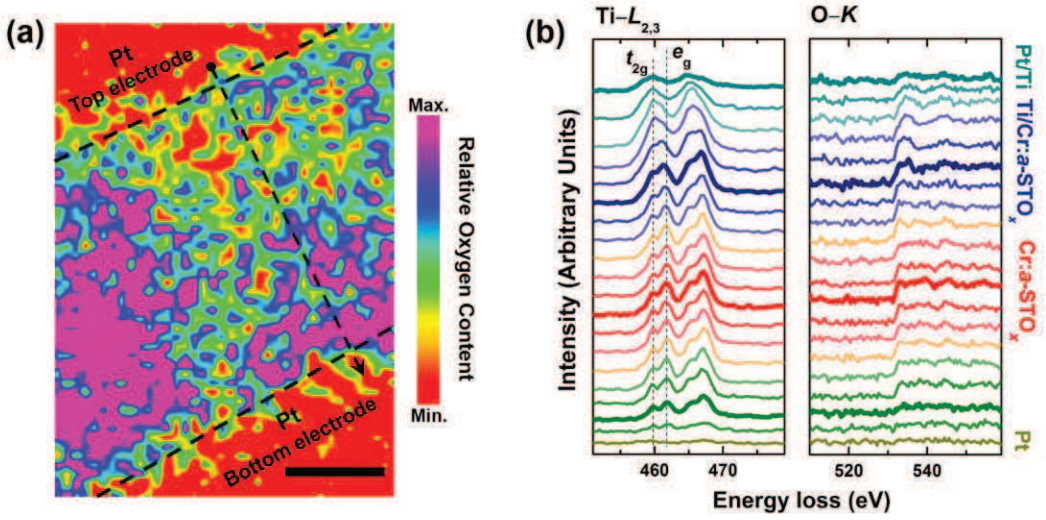

Figure 4.7 Electronic structure and compositional analysis of the filamentary path induced by CCW-BP resistive switching. (a) The EELS O–*K* edge area map of the conductive filament. The area map is collected over the ROI indicated in Figure 6a. Scale bar: 10 nm. (b) The Ti–$L_{2,3}$ and O–*K* edge profiles along a line scan across the MIM structure, passing over the conductive filamentary path in (a).

Figure 4.7b depicts the relative change in the fine structures of the background-subtracted Ti–$L_{2,3}$ and O–*K* edges along the EELS cross-sectional line scans passing over the locally crystalline ROI highlighted in Figure 4.6a. The edge profiles at the distinct points such as the top Pt/Ti interface, Ti/Cr:*a*-STO$_x$ interface, centre of the oxide layer and at the bottom Cr:*a*-STO$_x$/Pt interface are highlighted. The gradual evolution of the Ti oxidation states from the top Pt/Ti interface to the bottom Pt electrode are clearly observed in the Ti–$L_{2,3}$ edge profiles. On the other hand, O–*K* and Cr–$L_{2,3}$ edge spectra collected from the EELS line scan are weak and exhibit low signal-to-noise ratio which can be associated with the resolution limit of the instrument and low doping concentration of Cr (Cr/Ti ≈ 0.025). So we rely on the Ti–$L_{2,3}$ edge profiles to qualitatively analyze the electronic structure of the locally crystalline ROI. Since each V_o introduces two electrons into the Ti 3*d* orbital, the resulting change in the Ti valence band can be observed from the Ti–$L_{2,3}$ edge.[128, 136] At the top Pt/Ti interface, the Ti–$L_{2,3}$ profiles with broad peaks and relatively weak intensities indicate the presence of mixed Ti^{2+} and Ti^{3+} oxidation states.[132, 137, 138] At the Ti/Cr:*a*-STO$_x$ interfacial region, the crystal-field splitting of the Ti–L_3 and Ti–L_2 peaks into t_{2g} and e_g peaks which can be attributed to the presence of Ti^{3+} and Ti^{4+} oxidation

states.[132, 137, 139] However, away from the top interface and towards the bottom, more pronounced t_{2g} and e_g peaks indicate the dominant presence of the Ti^{4+} oxidation state. The change in Ti oxidation states across the MIM device suggest that the top Pt/Ti/Cr:*a*-STO_x interface is more oxygen deficient compared to the bottom Cr:*a*-STO_x/Pt interface which is consistent with the EELS O–*K* area map of the ROI (Figure 4.7a).

4.5 Mechanism of resistive switching in Cr:*a*-STO_x MIM devices

Based on the extensive material and interfacial characterization as well as the electrical characteristics, a mechanism for the unique behaviour of Cr:*a*-STO_x MIM devices is suggested. The inherent V_os in the Ti–O_6 octahedra that are created by preferentially removing the oxygen atoms due to the heavy Ar^+ ion bombardment during the sputtering process,[70] generate conduction band electrons in the Ti 3*d* states. However, doping with Cr (*via* co-sputtering from a metallic Cr target) localizes the conduction band electrons by trapping them at Cr sites, which reduces the Cr from Cr^{4+} to Cr^{3+} species.[140, 141] Consequently, no conduction electrons are introduced in the Ti *3d* states and therefore the pristine Cr:*a*-STO_x oxide exhibits an insulating nature.[140] Prior to the electroforming, all Cr:*a*-STO_x MIM devices exhibit device resistances of >1 GΩ. It is widely accepted that the electroforming process generates V_os and alters their distribution in metal oxides through subsequent electrochemical redox processes.[28, 40, 45, 127] Consequently, a localized channel for current flow through the oxide system is created which is essentially an oxygen deficient filamentary pathway. Moreover, the subsequent resistive switching is attributed to the rapture and formation of the filamentary path at its weakest part, most likely close to the electroforming anode,[95] through the Joule heating and drift of V_os under the influence of applied bias.

In the Cr:*a*-STO_x MIM devices, Cr doping further increases the concentration of V_os which facilitates the formation of a conductive filamentary path during the electroforming process.[46] The locally confined current flow through the filamentary pathway may induce local Joule heating causing the formation of locally extending crystalline regions in the bulk amorphous Cr:*a*-STO_x layer. Also, the top Ti layer (that

develops into a sub-stoichiometric Ti_2O_3 layer) introduces an additional switching layer that is electrochemically different to the Cr:*a*-STO_x. This causes a change in the mobility [142] and formation energies of V_os.[7, 143, 144] Ti_2O_3 is known to exhibit semiconductor-metal transition at an elevated temperature and is potentially responsible for the threshold resistive switching in MIM devices. During the switching cycles, the Joule heating produced by the electrical bias switches the Ti_2O_3 to its conducting phase resulting in a minimal electric field drop on Ti_2O_3 and as such it sustains the electrical bias without further reduction. Therefore, the current compliance and bias polarity dependent generation of V_os and the formation of filamentary paths in the Ti_2O_3/Cr:*a*-STO_x oxide heterostructure govern the multiple resistive switching behaviors in Cr:*a*-STO_x MIM devices. When the electroforming bias is applied across the MIM devices the applied electric field initializes the generation of V_os which is driven by the movement of oxygen ions towards the anode and several localized spots, including Cr doped sites, becoming oxygen deficient.[145] Under the influence of applied electroforming bias, the positively charged V_os drift towards the electroforming cathode and start to accumulate at its vicinity whereas their density extends towards the anode, forming an extended oxygen deficient filamentary pathway.

At lower current compliances (*i.e.*, 1-15 μA) during the electroforming, relatively less density of V_os are generated.[145] Also the insufficient driving force for their migration prohibits the complete formation of the filamentary pathway across the Ti_2O_3/Cr:*a*-STO_x interface. This results in the formation of two distinctive filamentary paths in the Ti_2O_3 and Cr:*a*-STO_x layers. Depending on the bias polarity, each layer switches (to LRS and HRS) individually to define the resistive state of the MIM device. Under these conditions, we explain the threshold switching behavior in MIM devices by the repetition of processes schematically depicted in the bottom panel of **Figure 4.8**. Post-electroforming electrical characteristics of the CRS and *p*-CRS behaviors suggest that both resistive switching behaviors follow a similar switching mechanism in terms of V_o distribution and migration in Ti_2O_3 and Cr:*a*-STO_x layers.

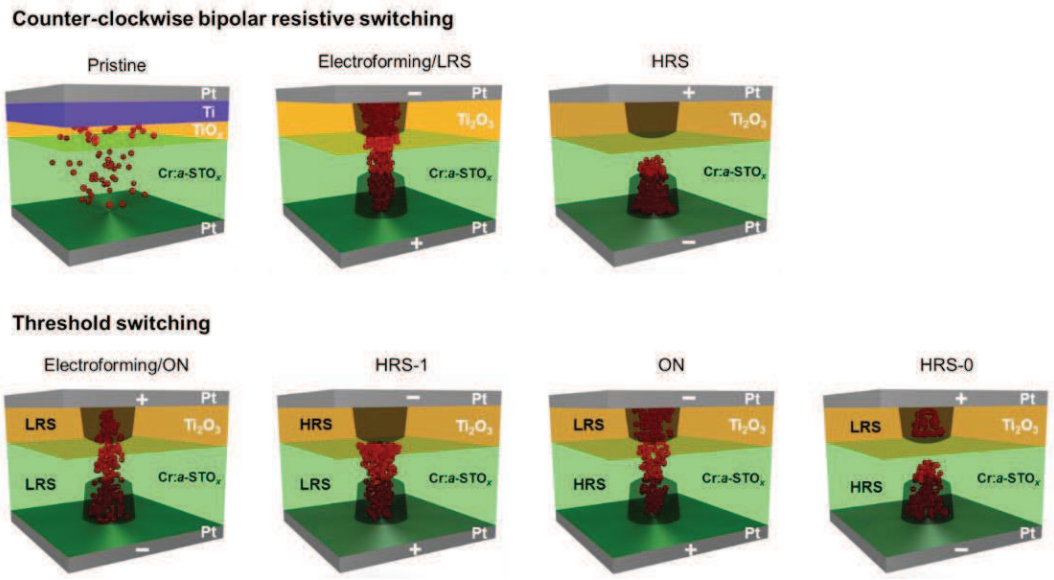

Figure 4.8 Schematic illustrations of the possible resistive switching mechanisms induced by variation in the current compliances during initial electroforming. The top panel depicts the changes during and after electroforming in the MIM devices exhibiting CCW-BP switching behavior. The lower panel illustrates the threshold resistive switching mechanism. The red spheres represent the V_os and dark structures in the center of schematics represent crystalline regions.

On the other hand, electroforming at higher current compliances (40-100 μA) generate a higher density of V_os and sufficient driving force is available for their migration across the Ti_2O_3/Cr:*a*-STO_x interface. The top panel in Figure 4.8 schematically depicts the subsequent mechanism of the CCW-BP resistive switching behavior where the complete formation of extended oxygen-deficient filamentary path across the Ti_2O_3/Cr:*a*-STO_x corresponds to the LRS and ruptured filamentary path (under reverse bias) set the HRS in MIM devices. Similar switching mechanism with opposite bias polarities can be applied to explain the CW-BP resistive switching behavior.

5 Bilayer Resistive Memories

Transparent non-volatile memory devices are desirable for realizing visually-clear integrated systems for information storage. This chapter is dedicated to the fabrication and characterization of the transparent a-STO_x based memory cells. In order to highlight the potential of these transparent memories for future multifunctional transparent and wearable electronics, a transient response to optical excitations is demonstrated.

5.1 Introduction

Transparent electronics is of increasing interest for the next generation of smart electronic circuitry that can enable devices capable of displaying information on surfaces such as glass windows. For a fully transparent integrated circuit, high transparency is also desirable in its important circuit element: the memory unit. For optical transparency without compromising memory density, inherent transparency is needed in a single memory unit. That raises the requirement of both the active switching material and the electrodes being transparent. In the past, a variety of materials and

microstructures including metal oxides,[146-148] nanotubes/rods [149, 150] and graphene based hybrid structures [151-153] have been studied separately as either opto-tunable or transparent memory systems. However, it is still challenging to achieve optical/electrical tunability and transparency on a single memory cell that is capable of high density data storage.

As the mechanisms governing many resistive switching systems are not yet fully understood and well-established, they are still part of ongoing research. Thus, assessment of any potential application in transparent electronics depends on the actual demonstration of a working system. This chapter demonstrates *a*-STO based fully transparent resistive random-access memories (*t*-ReRAMs) that feature high transparency (>85% including the substrate). The *t*-ReRAM cells are implemented in a stacked configuration with a bilayer structure comprising two *a*-STO layers with varying concentrations of V_os. It has been previously reported that a bilayer structure with each layer having different stoichiometry exhibits better switching performances compared to a single layer.[154-157] This is mainly because a combination of two layers, each with an intrinsic Schottky barrier, eliminates the need for using an additional element (generally a transistor or diode) to remove stray leakage current paths in high-density memory arrays.[155] Indium tin oxide (ITO), a well-known transparent conductor is used as the top and bottom electrode. The entire memory system is fabricated on glass, rendering all constituent elements of the memory unit to be optically transparent.

5.2 Optical transmission of *t*-ReRAMs

A schematic of the fabricated cross-point *t*-ReRAM cell is shown in **Figure 5.1a**, where the cell area (marked inside a rectangle on the cross-point structure) is magnified for a clear illustration of the multilayer cell structure. A homojunction of functional *a*-STO oxides with different concentration of V_os is achieved by sputtering STO in different O_2/Ar flow rates while keeping the deposition pressure constant at 3.5×10^{-3} Torr. A thin *a*-STO layer, as a base layer (BL) of the stack, is sputtered in 5% of oxygen (*i.e.*, O_2:Ar::5%:95%) on the bottom ITO electrode. This base layer is denoted as *a*-STO_y for further discussions. Following the *a*-STO_y sputtering, a second *a*-STO layer is sputtered (on *a*-STO_y/ITO) in a pure Ar environment (0% oxygen), denoted by *a*-STO_x. The stoichiometry of each *a*-STO layer is explained in the following section. As a top

electrode, a thin film of Ti (5 nm) is DC sputtered in a pure Ar environment on the oxide homojunction and capped with an ITO (40 nm) electrode. The Ti layer is expected to act as a sink for oxygen ions that evolve during electric field induced redox reactions resulting in the partial oxidation of Ti layer to Ti_2O_3 at the top interface. The role of top Ti/Ti_2O_3/*a*-STO_x interface in resistive switching, in the *t*-ReRAM cells, is further discussed in the following sections.

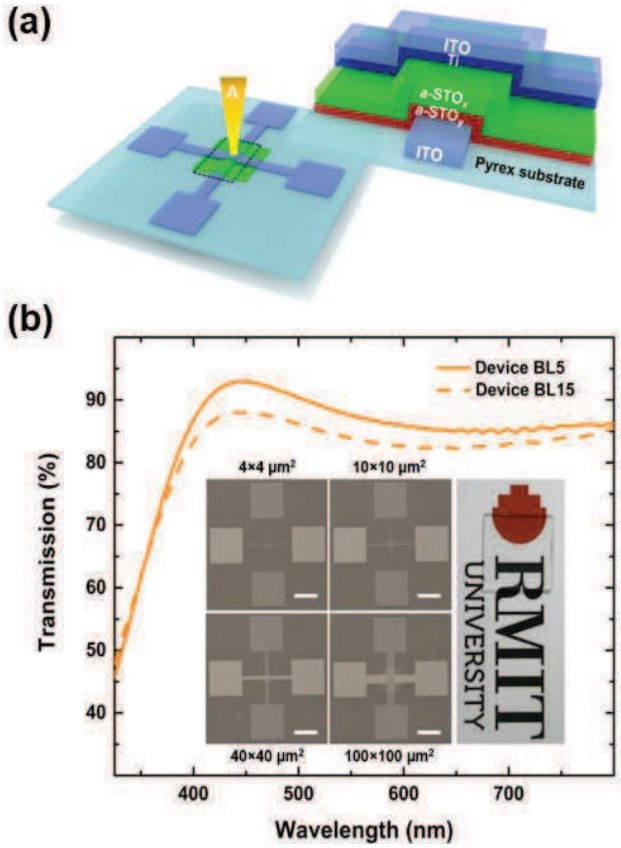

Figure 5.1 Physical structure and optical transmission characterization of *t*-ReRAM cells. (a) Schematic illustrations of the fabricated cross-point devices. Area enclosed in rectangle (presented with black dashed outline) on the cross-point structure, represents the active ITO/Ti/*a*-STO_x/*a*-STO_y/ITO/substrate region of the *t*-ReRAM cell. (b) The UV-Vis transmission spectra of Device BL15 and Device BL5 in the 325-800 nm optical range. The spectra are collected from the device area highlighted by "A" in (a). Inset shows the optical microscope images of cross-points with different sizes (scale bar 300 μm) and a 14×14 mm^2 sample placed on the RMIT University logo.

Two types of devices with varying BL (*a*-STO_y) thicknesses (15 nm and 5 nm) are synthesized, referred as Device BL15 (with the bilayer stack of *a*-STO_x/*a*-STO_y (10 nm/15 nm)) and Device BL5 (with the bilayer stack of *a*-STO_x/*a*-STO_y (10 nm/5 nm)). These devices are characterized optically and electrically. The optical transmission characteristics of the *t*-ReRAM cells are obtained from the area schematically indicated by a marker 'A' in Figure 5.1a. To assess the optical properties of each component constituting a *t*-ReRAM cell, the transmission and reflectance characteristics of the sputtered oxides are also acquired (Appendix C). The UV-Vis transmission spectra of the fabricated *t*-ReRAM cells (Figure 5.1b) for both devices show >80% transmission for visible optical wavelengths. Compared to Device BL5, a slightly lower transmission (by 3-5%) is observed in Device BL15, which can be attributed to the difference in the thickness of the functional oxide stack.

5.3 Compositional analyses of *a*-STO oxides

To evaluate the chemical composition of the sputtered *a*-STO oxides, XPS analysis is carried out on the uncapped bare *a*-STO_x and *a*-STO_y thin films. For elemental analysis, the as-obtained spectra are resolved by using a non-linear least square fitting method followed by background correction carried out using Shirley algorithm.[158] The core level spectra of O 1*s* and Sr 3*d* (Appendix C) do not show any significant shift in their respective binding energies (except for intensities) and are within the margin of error for the instrument resolution (±0.1 eV). The analyses of the de-convoluted spectra of the core level binding energies of Ti 2*p* are shown in **Figure 5.2**a. Both *a*-STO_x and *a*-STO_y spectra are fitted with two distinct components, namely – Ti^{4+} and $Ti^{(4-\delta)+}$. It is known that the presence of solely a Ti^{4+} component corresponds to a fully stoichiometric STO oxide, while the $Ti^{(4-\delta)+}$ species (such as Ti^{3+} and Ti^{2+}) represent the presence of V_os in the oxide system. However, Ti^{3+} and Ti^{2+} components cannot be resolved without ambiguity.[159] Therefore to avoid any doubt in assigning the oxidation states to these reduced species, we fit with only one component at the lower binding energies and denote as $Ti^{(4-\delta)+}$ (Figure 5.2a). In the *a*-STO_x and *a*-STO_y oxides, the peaks at Ti$2p_{3/2}$ binding energies of 458.4 eV are assigned to Ti^{4+} oxidation state while the peaks at 456.2 eV and 456.5 eV are assigned to $Ti^{(4-\delta)+}$ species.[70, 105, 133, 160] The relative concentration of the individual Ti^{4+} and $Ti^{(4-\delta)+}$ species are calculated by integrating the fitted peaks. The relative concentrations of Ti^{4+} and $Ti^{(4-\delta)+}$ in *a*-STO_x are calculated to

be 72.9% and 27.1%, respectively. On the other hand, the relative concentrations of $Ti^{4+}$and $Ti^{(4-\delta)+}$ species in *a*-STO_y are calculated to be 75.2% and 24.8%, respectively. It is seen that the concentration of $Ti^{(4-\delta)+}$ species in *a*-STO_x is comparatively higher than in the *a*-STO_y. This is expected, as the formation of a $Ti^{(4-\delta)+}$ (*i.e.*, an oxygen vacancy) due to the broken Ti–O bond in the sub-lattice results in the donation of extra electrons into the Ti 3*d* conduction band.[161, 162]

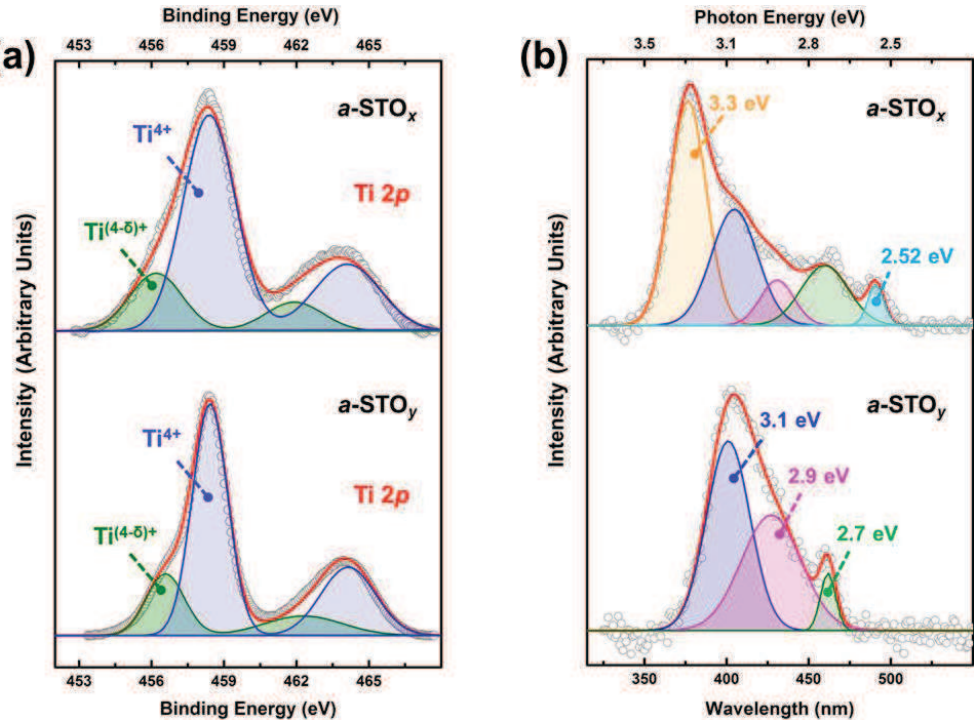

Figure 5.2 Material characterization of the sputtered *a*-STO oxide thin films. (a) The resolved core-level X-ray photoelectron spectra of Ti 2*p* of the sputtered *a*-STO thin films. (b) The resolved photoluminescence emission spectra of *a*-STO thin films, obtained at 300 nm excitation wavelength.

As such, the conduction process through the oxygen-deficient oxides is expected to take place through the Ti sub-oxide defect structures.[163] This indicates that the sputtering of *a*-STO in an oxygen depleted environment results in a relatively higher concentration of V_os than in the presence of oxygen. To explore the electronic structure of the deposited *a*-STO, photoluminescence (PL) emission spectra are obtained at room temperature using excitation at 300 nm (Figure 5.2b). Both oxides reveal a broad emission spectra which is characteristic of amorphous (doped and un-doped) STO.[111-113, 164-166] It is known that sputter deposition in a controlled oxygen environment

leads to the reduction of the inherent oxygen vacancy related defect structures (*i.e.*, $Ti^{(4-\delta)+}$ species),[70] which is confirmed with the XPS analysis (as explained earlier). Therefore, *a*-STO_x is expected to show PL emission at lower wavelengths compared to *a*-STO_y, which is indeed the case in our observations. De-convolution of the collected emission spectra from both *a*-STO films reveals multiple in-gap electronic states in *a*-STO oxides.[76, 113, 114] The *a*-STO_x thin film exhibits a broad emission spectrum between 340 nm and 500 nm with a maximum intensity at 376 nm (~3.3 eV). On the other hand, the *a*-STO_y thin film shows emission peaks between 360 nm to 480 nm with maximum intensity centered at 401 nm (~3.1 eV). The observed red shift (of 25 nm) in the main PL emission peak of *a*-STO_y (as compared to *a*-STO_x) can be associated with the re-organization of defect levels in the *a*-STO_y oxide.[112, 163]

5.4 Resistive switching performance

The typical bipolar resistive switching characteristics of Device BL15 (with *a*-STO_x (10 nm)/*a*-STO_y (15 nm) functional oxide stack) are shown in **Figure 5.3**. In their virgin state, the memory cells show a highly insulating nature (virgin state resistance of at least 0.5 GΩ measured at 0.5 V) and require an irreversible electroforming sweep to initialize the resistive switching behavior (see Appendix C). The current–voltage (*I–V*) characteristics of Device BL15 show a reproducible cyclic bipolar resistive switching (Figure 5.3a). Figure 5.3b shows the statistical distribution of threshold voltages for the onset transition of SET (transition from HRS to LRS, V_{SET}) and RESET (transition from LRS to HRS, V_{RESET}) during the cyclic bipolar resistive switching (Figure 5.3a), respectively. The distribution of V_{SET} ranges from -1 to -2.7 V with a mean at -1.7 V while V_{RESET} ranges from 1.6 to 4.9 V with a mean of 2.8 V.

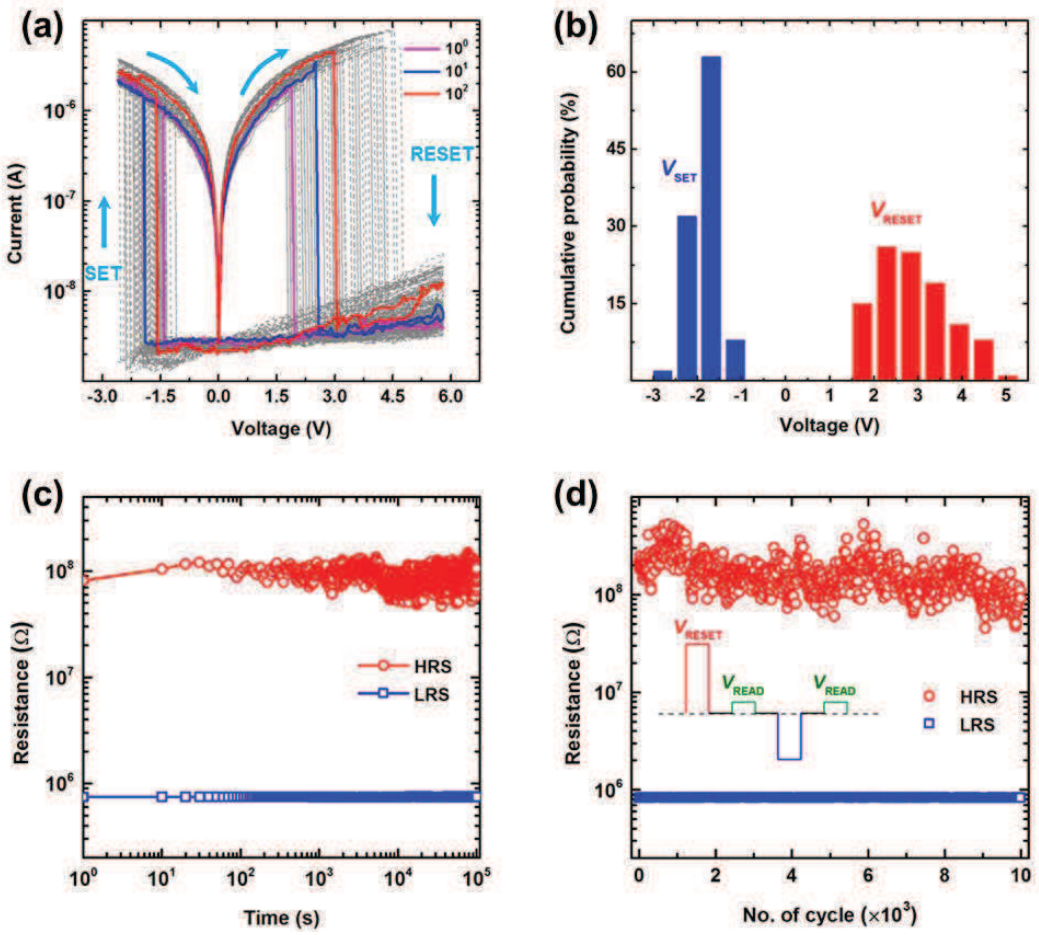

Figure 5.3 Electrical characterization of Device BL15 with 10×10 μm^2 cell area. (a) The post-electroforming bipolar *I–V* characteristics of 100 consecutive cycles on a semi-logarithmic scale. (b) Statistical distribution of V_{SET} and V_{RESET} for 100 consecutive switching cycles, shown in (a). (c) Retention of both LRS and HRS over 10^5 s under a constant positive V_{READ} of 0.5 V. (d) Endurance over 10^4 switching cycles. Inset shows the voltage pulse train used for V_{RESET} (6.2 V), V_{READ} (0.5 V) and V_{SET} (-3.7 V) during the endurance measurement where each pulse has a duration of 150 μs.

Although there are minor fluctuations in both LRS and HRS, the average switching ratio (HRS/LRS) is ~119 over a period of 10^5 s under a constant positive V_{READ} of 0.5 V (Figure 5.3c). The endurance of Device BL15 is measured for 10^4 switching cycles by using pulsed WRITE/READ/ERASE cycles, as shown in Figure 5.3d. During each switching cycle, short pulses (with duration of 150 μs) are used to RESET (6.2 V), READ (0.5 V) and SET (-3.7 V) the *t*-ReRAM cell.

The observed bipolar *I–V* characteristics in Figure 5.3a reveal that Device BL15 exhibits a linear LRS behavior under the measurement conditions. For large scale memory integration, such as crossbar ReRAM arrays, a linear LRS behavior makes the memory cells prone to the sneak paths and compromises the reliability of read data.[167] However, this problem can be overcome by introducing non-linearity into the LRS.[168] In the bilayer *t*-ReRAM cells it is expected that the *a*-STO_y layer plays a significant role in defining the resistive switching behavior.[70] Therefore, to illustrate the role of the *a*-STO_y layer in our bilayer *t*-ReRAM cells, another device (designated as Device BL5) with three times less thickness of *a*-STO_y (5 nm in this case, instead of 15 nm) as compared to Device BL15 is fabricated and characterized.

Figure 5.4 shows the bipolar resistive switching characteristics of Device BL5. The *I–V* characteristics (Figure 5.4a and 5.4b) reveal an asymmetric bipolar resistive switching behavior. The peculiar *I–V* crossing during the negative SET sweeps (at approximately -2.5 V) is explained in the later section. The non-linearity in on-state for Device BL15 and Device BL5 has been obtained by calculating the corresponding slopes of the *I–V* curves between 0-3 V (where the devices are in LRS). This slope for Device BL5 and Device BL15 is calculated to be 2 V/decade and 2.7 V/decade, respectively. This implies that Device BL5 exhibits relatively more non-linear characteristics than Device BL15.

The reliability characterization of Device BL5 reveals stable LRS and HRS retention (Figure 5.4c) for 10^5 s under a constant positive V_{READ} of 0.5 V. The average switching ratio is calculated to be ~114 over a period of 10^5 s. The endurance characteristics (Figure 5.4d) measured for 10^4 switching cycles show no device failure under a V_{READ} of 0.5 V. The non-linear LRS behavior observed in Device BL5 (Figure 5.4a and 4.4b) is preferable to alleviate the sneak currents in their large scale ReRAM array integration.[169] Generally, the memory cells responsible for sneak paths in an array experience lower voltage drop than V_{READ} applied to a target cell. Thus, the non-linear dependence of read current on voltage can significantly reduce the contribution of sneak currents.

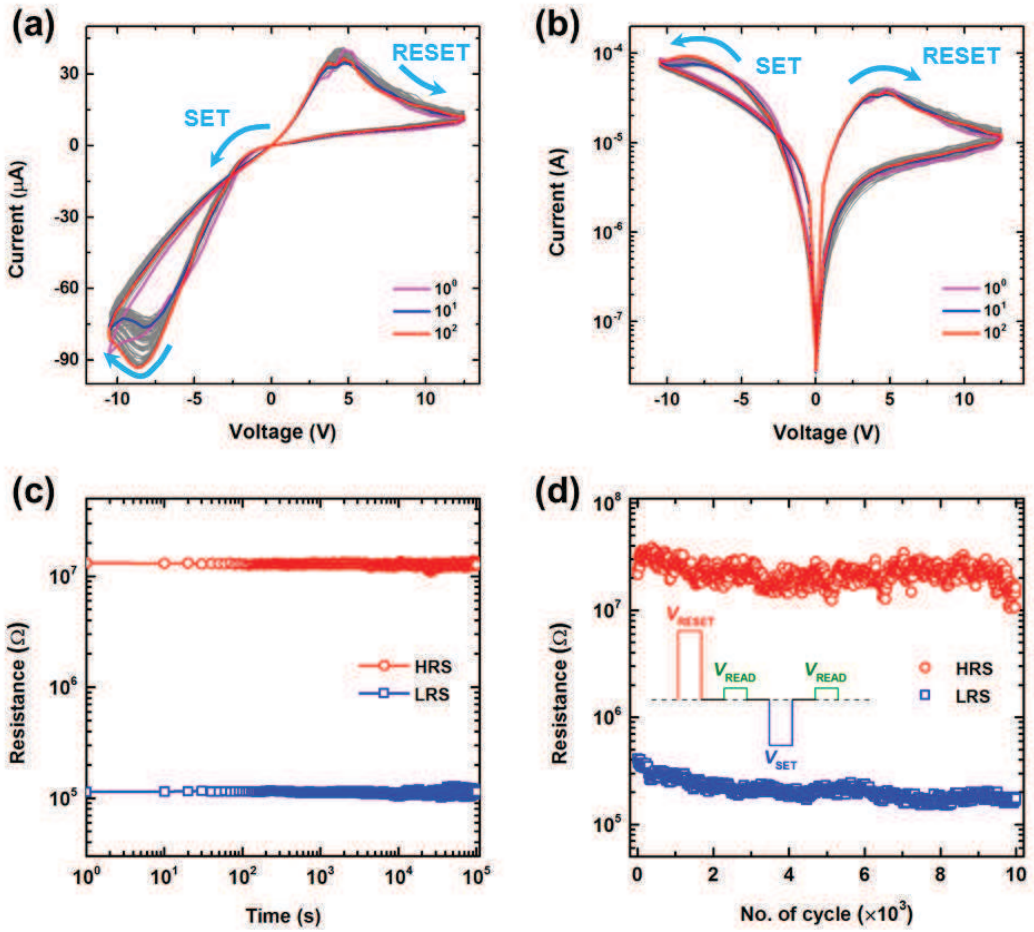

Figure 5.4 Electrical characterization of Device BL5 with 10×10 μm^2 cell area. (a) The post-electroforming bipolar *I–V* characteristics on a linear scale and (b) on a semi-log scale for 100 consecutive switching cycles. (c) Retention of both LRS and HRS over 10^5 s under a V_{READ} of 0.5 V. (d) Endurance over 10^4 switching cycles. Inset shows the voltage pulse train used for V_{RESET} (13.8 V), V_{READ} (0.5 V) and V_{SET} (-12.7 V) during the endurance measurement where each pulse has a duration of 500 μs.

5.5 Microstructure of *t*-ReRAMs

To analyze the physical structure of the *t*-ReRAM cells, cross-sectional TEM micrographs of virgin and electroformed memristive cells are obtained. Figure 4.5a shows the cross-sectional TEM micrograph of Device BL5 in its virgin state. A high-resolution TEM (HRTEM) micrograph reveals an amorphous structure of the *a*-STO stack in the virgin *t*-ReRAM cell (inset of Figure 5.5a). The selected area electron diffraction (SAED) pattern collected from the top ITO electrode and the Ti/*a*-STO$_x$

interface shows a diffused ring (Figure 5.5b), indicative of an amorphous structure whereas, the SAED patterns of the post-deposition annealed bottom ITO electrode showed discrete diffraction spots (Figure 5.5c). The diffraction patterns in Figure 5.5c can be indexed to the cubic bixbyite structure of In_2O_3.[170-173] The polycrystalline structure of the post-deposition annealed ITO thin films is also identified by X-ray diffraction (Appendix C).

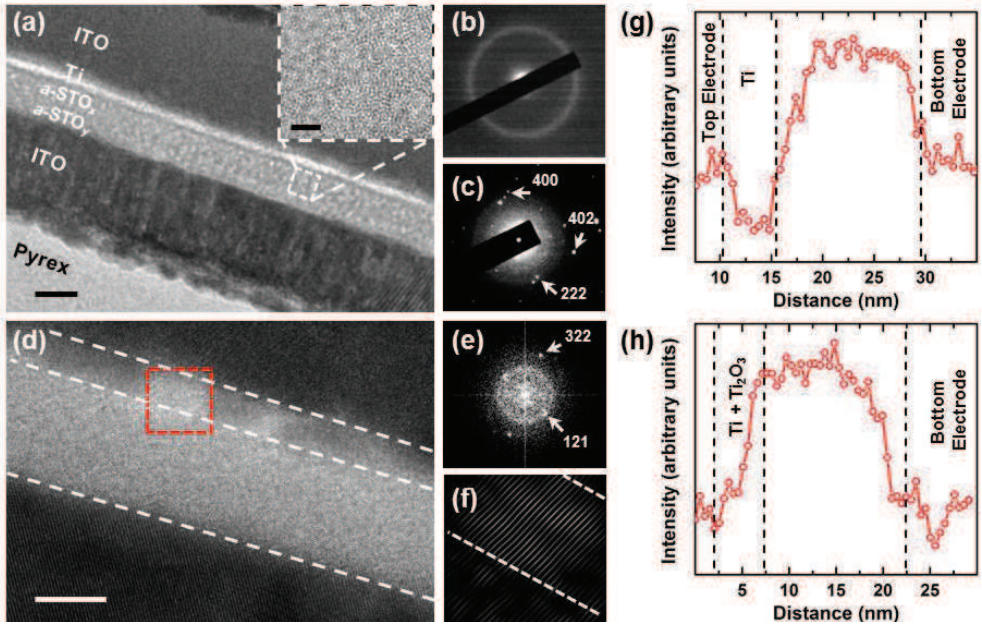

Figure 5.5 Structural analysis of the *t*-ReRAM cells. (a) The cross-sectional TEM micrograph of a virgin Device BL5 *t*-ReRAM cell (scale bar 20 nm). Inset shows the HRTEM image of *a*-STO_x layer (scale bar 2 nm). The SAED patterns collected from the top as-deposited ITO electrode (b) and the bottom annealed ITO electrode (c). (d) The cross-sectional HRTEM micrograph of an electroformed Device BL5 *t*-ReRAM cell (scale bar 10 nm). (e) The FFT of a region of interest selected and highlighted in (d). (f) The inverse FFT of the region of interest obtained from the diffraction spot corresponding to 121 in (e). (g) The EELS oxygen *K*-edge spectra of a virgin and (h) an electroformed *t*-ReRAM cell, recorded along a line scan across the cells.

The cross-sectional HRTEM micrograph of an electroformed Device BL5 *t*-ReRAM cell (Figure 5.5d) reveals the presence of a polycrystalline layer at the top Ti/*a*-STO_x interface. For the compositional analyses of this polycrystalline layer, a region of interest (ROI) is selected (highlighted by a box in Figure 5.5d) at the top Ti/*a*-STO_x interface. Figure 5.5e shows the Fast Fourier transform (FFT) diffraction pattern

obtained from the ROI. The diffraction spots with the *d*-spacing of 0.18 nm and 0.27 nm are indexed to [322] and [121] planes of rhombohedral Ti_2O_3. The [121] diffraction spots are used to generate the inverse FFT (Figure 5.5f) which highlights the dominant existence of Ti_2O_3 [121] in the ROI. This indicates that during the electroforming process, the applied electric field induced Joule heating and diffusion of evolved oxygen ions into the Ti layer result in the formation of a polycrystalline Ti_2O_3 layer.

The observed brighter contrast at the top ITO/Ti/*a*-STO_x interface (in Figure 5.5a) and the distribution of oxygen content across the virgin and electroformed *t*-ReRAM cells is assessed by the electron energy loss spectroscopy (EELS). The oxygen *K*-edge spectrum (Figure 5.5g) collected along a line scan across the virgin *t*-ReRAM cell reveals the partial oxidation of Ti to a oxygen depleted titanium oxide layer (*i.e.*, Ti_2O_3) at the top Ti/*a*-STO_x interface. This observation is consistent with our earlier XPS analysis of virgin memory cells.[70] On the other hand, the oxygen *K*-edge spectrum of the electroformed *t*-ReRAM cell (Figure 5.5h) shows an increase in the thickness of polycrystalline Ti_2O_3 layer at the top Ti/*a*-STO_x interface and a decrease in the oxygen content at the bottom *a*-STO_y/ITO interface as compared to rest of the *a*-STO stack. It can be inferred that relatively higher concentration of V_os are present at the vicinity of bottom interface due to the reversible redox reactions (under the influence of electroforming bias). Furthermore, the Ti $L_{2,3}$-edge spectrum collected from the electroformed cell showed relatively higher morphological ordered in *a*-STO than the virgin *t*-ReRAM cell (Appendix C). A detailed description of the electronic structure of the *a*-STO layers and switching mechanism of the *t*-ReRAM cells is explained in rest of this chapter.

5.6 Resistive switching mechanism in *t*-ReRAMs

In order to assess the resistive switching mechanism in the bilayer *t*-ReRAM cells, a room-temperature PL mapping technique is employed due to its non-destructive analysis nature (unlike cross-sectional TEM analyses) and sensitivity to the defect or impurity states.[164] It is well-known that the intrinsic oxygen related defects (such as $[TiO_5 \cdot V_o^{1+}]$ and $[TiO_5 \cdot V_o^{2+}]$ complexes, where V_o^{1+} and V_o^{2+} denote single and double positively charged oxygen vacancies, respectively) in *a*-STO introduce localized in-gap states above the valence band and are responsible for the room temperature PL emission.[111, 112, 114, 162] Also, the PL emission is correlated with the concentration

of oxygen related defects (*i.e.*, V_os) such that the PL response can be modulated by changing the density of V_os.[76, 164, 174] By exploiting the high sensitivity of PL emission to the V_os, a direct observation of oxygen deficient regions and conductive filament is demonstrated (**Figure 5.6**) *via* submicron high spatial resolution PL maps, under a 405 nm excitation source (Appendix E). As observed in XPS and PL analyses of the sputtered *a*-STO thin films (Figure 5.2) both as-grown oxides (*a*-STO_x and *a*-STO_y) are oxygen deficient. So, the identification of oxygen deficient regions by PL signals is expected in a virgin *t*-ReRAM cell. However, diffuse scattering in ITO/glass substrate hinders the identification of oxygen deficient regions in the virgin cell (Figure 5.6a). On the other hand, a switching cell shows the distribution of oxygen deficient regions over the cell area in both HRS and LRS with different PL emission intensities (Figure 5.6b and 5.6c, respectively). This indicates that the overall concentration of V_os increased in the bilayer stack after the electroforming and subsequent switching cycles. The intensity thresholds are kept the same to enable a direct comparison of the PL response in different resistive states.

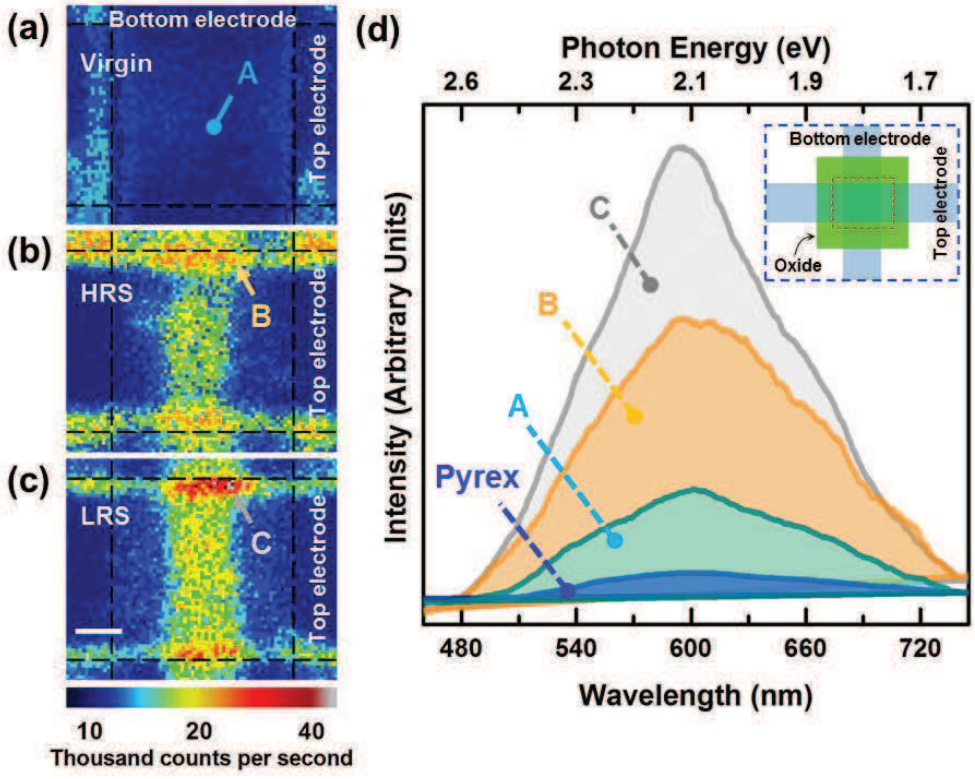

Figure 5.6 Photoluminescence mapping of the bilayer *t*-ReRAM cell. The PL maps (top-view) of a 4×4 μm^2 Device BL15 *t*-ReRAM in its (a) virgin state, (b) HRS and (c) LRS, under 405 nm excitation source. Scale bar corresponds to 1 μm. (d) The PL emission spectra collected from different regions of the cell in its virgin, HRS and LRS

marked in (a), (b) and (c), respectively. Inset of (d) shows a schematic of a *t*-ReRAM cell highlighting the region of interest used for PL maps in (a)-(c).

On comparing the PL maps, relatively more oxygen deficient regions are observed at the edges of the top electrode after a virgin cell is subjected to the electroforming process. This can be attributed to the applied electric field induced generation of higher concentration of V_os in these regions during the electroforming.[40, 45] Figure 5.6d shows broad peaks of the PL emission spectra around 600 nm (2.1 eV), collected from different regions of the *t*-ReRAM cell in its virgin, HRS and LRS marked as 'A', 'B', and 'C' in Figure 5.6a, b and c, respectively. Comparatively, the highest PL intensity observed for location 'C' (Figure 5.6c) can be ascribed to the accumulation of V_os at this hotspot under the influence of the applied LRS bias. This localized intense PL emission compared to its vicinity indicates the presence of a conducting filament comprising of accumulated V_{oS} in the LRS. While relatively lower PL emission ('B') from the same region, indicates a change in the distribution of V_os in HRS. By using different spectroscopic and nano-contact studies, Nili *et al.* have shown the existence of nano-filaments in *a*-STO based resistive memories.[70, 98, 110] However, this PL mapping technique further highlights the primary role of V_os in disordered *a*-STO oxides and clearly indicates the filamentary based resistive switching in the *a*-STO bilayer *t*-ReRAMs.

5.7 Mechanism of resistive switching in *t*-ReRAMs

Based on the electrical and material characterization of our bilayer homojunction *t*-ReRAM cells, a possible resistive switching mechanism in these devices is suggested. It is well known that mixed electronic/ionic charge transport and reversible redox reactions are mainly responsible for the resistive switching in STO based ReRAMs.[20, 28, 70, 98] In the presence of an externally applied electric field, reversible redox reactions increase the concentration of as-grown V_o based defect structure in the Ti–O sub-lattice and consequently nanoionic charge transportation occurs along the Ti^{3+} suboxide.[45, 163] As evident from the XPS analysis, the relative concentration of as-grown $Ti^{(4-\delta)+}$ species is higher in *a*-STO_x (27.1%) than *a*-STO_y (24.8%); therefore, the charge carriers (*e.g.*, oxygen ions and free electrons) are expected to drift across the *a*-

STO bilayer stack under the influence of an applied bias. So the proposed resistive switching model in the bilayer *t*-ReRAM cells is based on the extension and rupture of V_o based defect structure (*i.e.*, localized conductive filament) through the *a*-STO layers.[28, 95]

Figure 5.7 schematically illustrated the possible resistive switching mechanism in the bilayer homojunction (Device BL15 and Device BL5) *t*-ReRAM cells. In its virgin state, a *t*-ReRAM cell (regardless of the device type) has higher concentration of as-grown V_os in *a*-STO_x than *a*-STO_y layer (Figure 5.7a1 and b1). As observed from the TEM analysis (Figure 5.5) of a virgin *t*-ReRAM cell, the top Ti layer partially oxidizes in the vicinity of *a*-STO_x and a thin layer of amorphous Ti sub-oxide (such as Ti_2O_3) is formed at Ti/*a*-STO_x interface. However, this interfacial Ti sub-oxide layer is oxygen depleted and therefore the carrier transport can still take place across the top interface.[70, 133] When the bottom ITO electrode of a virgin *t*-ReRAM cell is negatively biased (Figure 5.7a2 and b2), the localized Ti–O sites become oxygen depleted due to the electrochemical redox process and the oxygen ions (O^{2-}) drift towards the top ITO electrode (acting as anode) through the *a*-STO_x layer. At the anode, O^{2-} discharge to evolve oxygen gas due to the oxidation reaction.[40, 45] In the presence of neutral oxygen and applied electric field induced Joule heating, the thickness of Ti_2O_3 layer increases and its microstructure changes to polycrystalline (as observed in cross-sectional TEM analyses, Figure 5.5d-f). Simultaneously, with an increasing negative bias at the bottom electrode, the concentration of V_os increases in the bilayer oxide stack (as observed in PL maps Figure 5.6). When the applied bias reaches the level of forming voltage for a virgin (or V_{SET} for an electroformed) *t*-ReRAM cell, the concentration of V_os extends toward the anode.[26, 27] As a result the bilayer *a*-STO_x/*a*-STO_y stack provides a localized conductive path for the electronic transport between opposite electrodes thereby, significantly changing virgin state resistance (or HRS for an electroformed *t*-ReRAM cell) to LRS. Also the Joule heating effect can increase the microstructural order of the amorphous oxides,[131, 175] as observed in our EELS analysis of the electroformed cell (Appendix C). On the other hand, a negative bias on the top ITO electrode (acting as a cathode, Figure 5.7a3 and b3) drifts the O^{2-} from the top Ti_2O_3/*a*-STO_x interface towards the *a*-STO_x layer. As the bias increases to V_{RESET}, the O^{2-} recombine with the V_os and produces neutral oxygen ions ($O^{2-} + V_o \rightarrow O_0$). Consequently, a partially ruptured conductive path remains in the bilayer *a*-STO_x/*a*-STO_y stack and the *t*-ReRAM cell switches to HRS.

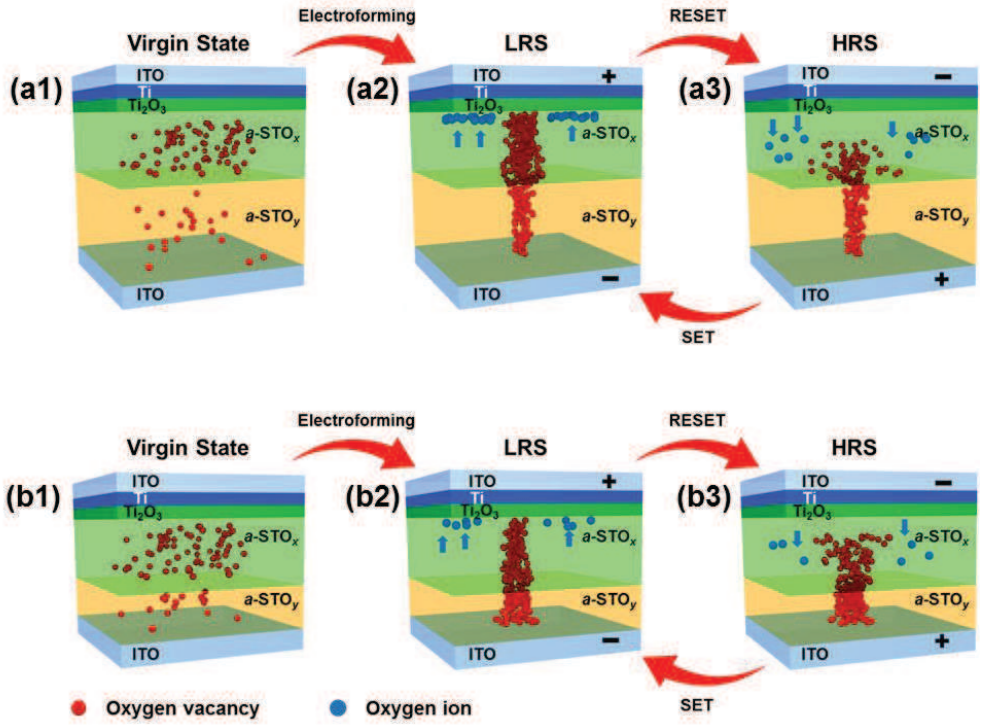

Figure 5.7 Schematic illustrations of the possible resistive switching mechanisms in the *t*-ReRAM cells of (a1-a3) Device BL15 and (b1-b3) Device BL5. Transformation of the *t*-ReRAM cell from (a1, b1) a virgin state to a repeatable (a2, b2) LRS and (a3, b3) HRS. The red and blue spheres represent oxygen vacancies (V_os) and oxygen ions (O^{2-}), respectively, whereas the blue arrows show the direction of O^{2-} drift under the influence of applied electric field.

Despite the similar top and bottom interfaces (Ti_2O_3/*a*-STO_x and *a*-STO_y/ITO, respectively), the observed difference in the resistive switching behaviors in Device BL15 (linear switching) and Device BL5 (non-linear switching) can be explained by considering the distribution of V_os in the *a*-STO_x and *a*-STO_y layers. The Device BL15 electroforms at relatively higher voltages than Device BL5 (Appendix C) which results in higher concentration of V_os in the *a*-STO_x layer, as depicted in Figure 5.7a2. Consequently, the *a*-STO_x layer is more conductive than *a*-STO_y layer which translates into higher resistances in both LRS and HRS of Device BL15 (even at comparatively lower SET/RESET voltages than Device BL5). On the other hand, comparatively higher SET voltages of Device BL5 result in a drift of V_os from the *a*-STO_x layer to the vicinity of bottom *a*-STO_y/ITO interface (as depicted in Figure 5.7b2).

This explains the relatively higher conductivity of the *a*-STO_y layer of Device BL5 (than *a*-STO_y layer of Device BL15) and also its lower LRS/HRS resistances.

Furthermore, a plausible explanation for the peculiar *I–V* crossing during the negative SET sweeps of Device BL5 (Figure 5.4a and b), can be presented by considering the Joule heating induced electrochemical modification of the top Ti_2O_3/*a*-STO_x interface. Under a relatively high SET bias, the localised temperature around the filamentary region can be significantly higher than the rest of device (due to the Joule heating). This can induce a repeatable electro-thermal negative differential resistance (NDR) effect which explains the decrease in current at -8.2±0.5 V (Figure 4.4a). Since the Ti sub-oxide phase (such as Ti_4O_7) is known to exhibit the Joule heating induced NDR phenomenon,[168, 176] the top Ti/Ti_2O_3/*a*-STO_x interface is likely to be electrochemically modified (to a sub-stoichiometeric interfacial layer) during the cyclic SET sweeps. This possibly underpins the peculiar *I–V* crossing at approximately -2.5 V in Device BL5.

5.8 Photo-response of *t*-ReRAMs

To fully benefit from the transparency of the *t*-ReRAM cells, it is essential to explore the optical tunability of their resistive states. We studied the photo-response of our *t*-ReRAM cells *via* a sequential exposure to different illumination wavelengths. As observed in the PL spectra (Figure 5.2b), the presence of V_os induced in-gap electronic states result in a photo-response of *a*-STO oxides in a wide wavelength window (ranging between 365 nm to 530 nm). This suggests that the *t*-ReRAM cells will be optically responsive to the excitation wavelengths in this range.

Figure 5.8 shows the time-resolved photo-electronic response of our *t*-ReRAM cells with varying active areas to different wavelengths in their virgin and HRS states. It can be observed that regardless of their active cell area and resistive states, both Device BL15 (Figure 5.8a) and Device BL5 (Figure 5.8b) show higher photocurrent under ultraviolet (UV, 365 nm) as compared to the blue (455 nm) under equal power densities of 2.5±0.2 mW/cm^2. This is consistent with the observed PL spectra from *a*-STO oxides and indicates that more photo-induced carriers are generated as the illumination wavelength decreases towards the corresponding bandgap (<390 nm).[177-179] Both Device BL15 and Device BL5 show an area dependent photocurrent in their virgin state. This can be explained by considering the area dependent density of V_os in

virgin *t*-ReRAM cells and also relatively lower density of V_os (than electroformed cells) where they act as trapping sites for injected electrons under a low V_{READ}.[180-182] Light illumination de-traps the electrons into the conduction band which are driven through the device by V_{READ}.[147, 183-185] On the other hand, no obvious relation between the active cell size and photocurrent is found in HRS of both Device BL15 and Device BL5 *t*-ReRAM cells. In HRS, low electrical conduction is usually attributed to the transportation of electronic carriers through the oxide/electrode interfacial barrier.[10,41] While the area independent HRS photo-response in the *t*-ReRAM cells can be associated with the transportation of photo-excited electrons through the localized variation of ITO/*a*-STO interfacial barrier at the conductive filament without affecting the remaining interfacial barrier,[186] it should be noted that photo-electronic response is only observed in HRS of the *t*-ReRAM cells. In the LRS however, the presence of electrically induced conductive filamentary path (as discussed in the preceding section) provides a fast route for the transportation of charge carriers;[45] hence, diminishing the photo-response of the *t*-ReRAM cells. Such an area independent optical and electrical properties of *t*-ReRAMs highlight the scalability potential of these devices.

Regardless of the cell area, relatively higher average UV response (I_{UV}/I_{Dark}) of Device BL15 (8.7±0.1) than Device BL5 (4.1±0.2), can be attributed to the higher V_o concentration owing to the thickness of *a*-STO stack.[182, 187, 188] Furthermore, a fast photocurrent modulation (10 Hz) of Device BL15 is achieved under the UV illumination (Appendix C), indicating a fast response time, a required feature for photo-electronic devices such as optoelectronic switches and memories.[187, 189] In addition, to assess the contribution of ITO electrodes in the photo-response, each electrode is exposed to the illumination and no significant photo-response is observed (Appendix C). As a result, the role of ITO can be neglected. These results reveal that the *a*-STO *t*-ReRAMs, with attractive features such as fast and area independent photo-response, demonstrate a multifunctional storage system where memory states can be optically read by using a specific light irradiation. Moreover, the reported memory design is also capable of enabling memory cells to work as light sensors.

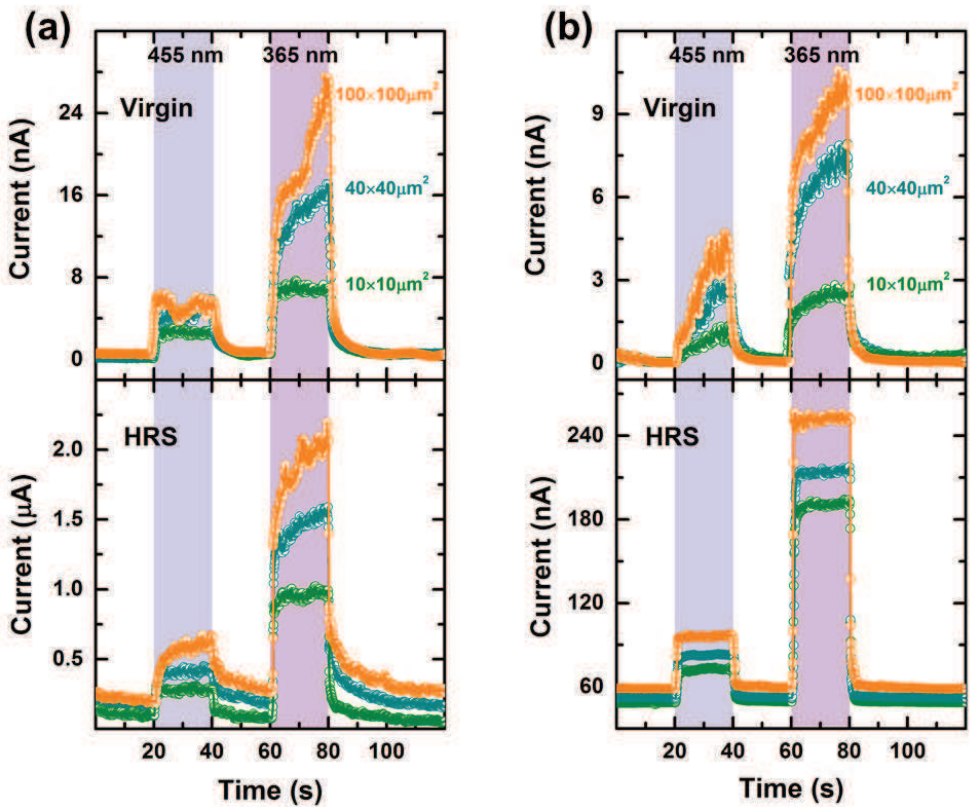

Figure 5.8 Photo-response of ITO/Ti/*a*-STO_x/*a*-STO_y/ITO structured *t*-ReRAM cells in virgin and HRS. (a) The measured photocurrent of Device BL15 and (b) Device BL5 upon exposure to the blue and UV illuminations with wavelengths of 455 and 365 nm, respectively, at a V_{READ} of 0.5 V. The *t*-ReRAM cells with active area of 10×10, 40×40 and 100×100 μm^2 are sequentially exposed to the illuminations with an incident power of 2.5±0.2 mW/cm^2 for 20 s.

6 Memories as artificial synapses

Memristors have been recognized as potential building blocks for the future versatile neuromorphic architectures due to their non-volatility, scalability, low-power consumption, fast response time and homologous regulatory mechanisms with biological synapses. However, despite their desirable characteristics, the complex drive circuitry, electroforming process, device-to-device variability and stochastic nature of resistive switching are hindering the realization of efficient neuromorphic networks. Furthermore, the implementation of several higher order synaptic functions observed in biological neural systems has not been explored in the previous studies. This chapter presents the practical implementation of time and rate-dependent synaptic learning rules on the a-STO memristors.

6.1 Introduction

The functionality of a brain is attributed to the activity-dependent synaptic weight change, enabling principal cognitive functions.[190] Although the underlying precise biological mechanism of the synaptic functionality is still under debate,[191] it is well established that *in vivo* neurons follow Hebbian synaptic learning through spike-time-dependent-plasticity (STDP).[192-196] Conventional complementary metal oxide semiconductor (CMOS) circuits have been employed to mimic the biological synaptic learning,[197] but with no intrinsic learning capability, high energy consumption and limited scalability restrain the CMOS neuromorphic systems to achieve similar efficiency and density as a brain (10^8-10^{14} mm^3).[198] Significant reduction in complexity, energy consumption, intrinsic non-volatility and high scalability of a nanoscale memristor qualify it as a basic element for any versatile artificial neuromorphic architectures.

It has been shown that a nanoscale memristor can function as an artificial synapse due to its similar activity dependent nonlinear conductance modulation.[167, 199-201] However, memristors require integration with the driving CMOS subsystems to successfully execute the memory/computation operations and emulate synaptic functions. To date, several hybrid CMOS-memristor architectures have been reported to achieve high density memory systems and neuromorphic computing paradigm.[169, 202, 203] But inefficient complex CMOS circuitry, inexorable electroforming process causing a high device-to-device variability and stochastic nature of resistive switching are hampering the realization of extremely efficient neuromorphic networks.[44, 167, 202] A hybrid architecture implementing a simple dynamic CMOS circuitry to comply with any type of memristors and an energy efficient electroforming-free memristor would enable to imitate versatile neuromorphic functions.

In this study, we demonstrate such a hybrid CMOS-memristor approach to practically emulate the synaptic functions. This approach employs CMOS-compatible amorphous oxygen deficient $SrTiO_{3-x}$ (*a*-STO_x) memristors as artificial synapses.[70, 102, 110] These synaptic devices exhibit electroforming-free characteristics which is a desired feature for energy efficient neuromorphic networks. Although, synaptic functions including pair-based STDP (*p*-STDP) have been implemented on different types of memristors;[204, 205] however, higher order time-dependent and rate-dependent learning rules (discovered in the biological synapses) such as triple-STDP (*t*-STDP) and

Bienenstosk Cooper Munro (BCM)[206-208] have not been experimentally demonstrated on artificial synaptic devices. We acknowledge that a few memristive models and circuits are recently proposed to reproduce these synaptic learning rules.[209-211] However, a physical emulation of these essential biological learning rules will signify the potential of exotic memristors for future neuromorphic computation. Herein, we employ electroforming-free *a*-STO_x synaptic devices to experimentally implement these STDP learning rules and benchmark the results against the biological dataset. Furthermore, a simple yet highly flexible CMOS drive circuit is adapted rendering its capability to implement a variety of synaptic functions. As such, we exploit the room temperature CMOS-compatible synthesis, electroforming-free characteristics of *a*-STO_x memristors and flexible design of the CMOS drive circuitry to demonstrate the realization of an efficient and reliable neuromorphic system.

6.2 Material Characterization

The chemical composition of the as-sputtered *a*-STO_x thin film is analysed by the X-ray photoelectron spectroscopy (XPS). In order to evaluate the stoichiometry, the core-level elemental spectra of the as-sputtered *a*-STO_x thin film are compared with the spectra collected from a reference stoichiometric STO (100) substrate, as shown in **Figure 6.1**. The Sr 3*d* and O 1*s* spectra of both samples show similar binding energies which are within the margin of measurement error (±0.1 eV). The Sr 3*d* spectra of stoichiometric STO and *a*-STO_x (Figure 6.1a) is fitted into a doublet where the binding energies of Sr $3d_{5/2}$ at 132.94 eV and 132.97 eV, respectively, can be attributed to Sr^{2+} state.[212, 213] The O 1*s* spectra of stoichiometric STO and *a*-STO_x (Figure 6.1b) is fitted with two distinct peaks. The peaks at binding energies of 529.45 eV (for stoichiometric STO) and 529.47 eV (for *a*-STO_x) correspond to O^{2-} ions[212] while peaks at higher binding energies can be associated to the adventitious C–O bonds [70, 212, 213] on the surfaces. On the other hand, the Ti 2*p* spectra of the both stoichiometric STO substrate and our *a*-STO_x are shown in Figure 6.1c. The Ti 2*p* spectra of the stoichiometric STO suggest that Ti is present in its single oxidation state, *i.e.* Ti^{4+} with Ti $2p_{3/2}$ peak at 458.37 eV.[160, 213, 214] However, the resolved Ti 2*p* spectra of the sputtered *a*-STO_x thin film show two distinct oxidation states with Ti $2p_{3/2}$ peaks at binding energies of 457.9 eV and 456.2 eV which correspond to the Ti^{4+} and Ti^{3+} oxidation states, respectively.[70, 212] The relative concentration of Ti^{4+} and Ti^{3+} is calculated by

integrating the respective fitted peaks. The ratios of Ti/Ti^{4+} and Ti/Ti^{3+} in *a*-STO_x are calculated to be 70.6% and 29.4%, respectively. This indicates that the STO thin films sputtered for *a*-STO_x synaptic devices are comparatively more oxygen deficient than our previously reported oxide films (with Ti/Ti^{3+} ratios ranging from 24.8% to 27.1%).[102] This can be associated with the sputtering conditions of STO in a pure argon environment where Ar^+ ion bombardment results in the preferential removal of oxygen atoms and creates inherent oxygen vacancies (Appendix E).[76] It is expected that by controlling the defect chemistry of *a*-STO oxide structure, the energy requirements and resistive switching characteristics can be tuned.[70]

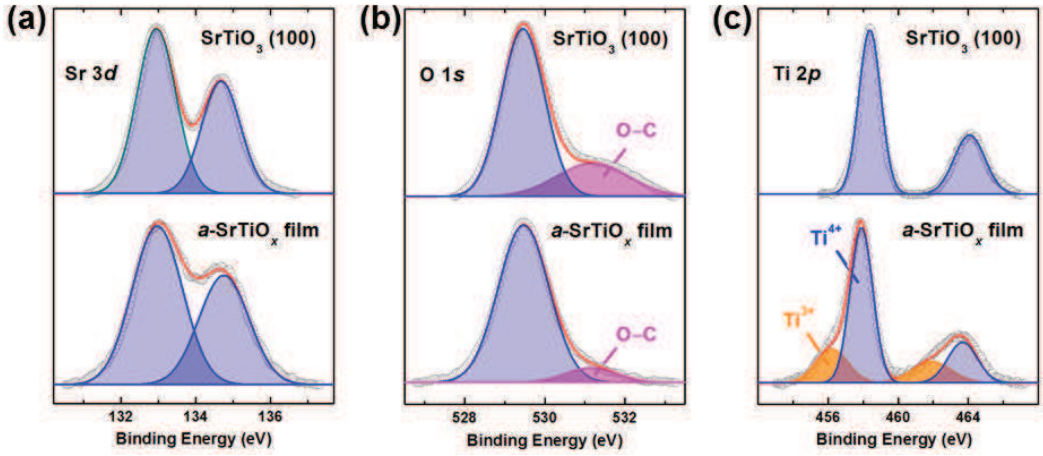

Figure 6.1 Material characterization of $SrTiO_3$. The resolved core-level XPS spectra of (a) Sr 3*d* (b) O 1*s* and (c) Ti 2*p* collected from a reference stoichiometric $SrTiO_3$ (100) substrate and the sputtered *a*-STO_x thin film.

6.3 Resistive switching characteristics of the synaptic devices

The *a*-STO_x synaptic devices are fabricated in metal-insulator-metal (MIM) configuration as a bilayer stack of Ti/*a*-STO_x sandwiched between top and bottom Pt electrodes. The *a*-STO_x MIM devices are fabricated with different active cell area ranging from 4×4 μm^2 to 100×100 μm^2 to analyse its effect on the resistive switching characteristics (Appendix E). Unlike our previously reported STO memristors,[70, 98, 102, 110] where an initial electroforming is required to activate the resistive switching, herein fabricated *a*-STO_x synaptic devices exhibit bipolar resistive switching without initial electroforming step. The as-fabricated MIM devices are in their high resistive

states (HRS) as the measured pristine resistances are close to the normal variance of the HRS achieved during the subsequent cyclic switching. However, the pristine state resistances are device area dependent (Appendix D). Furthermore, the statistical analysis of the as-fabricated devices show that the average SET and RESET voltages (*i.e.*, V_{SET} and V_{RESET}, respectively) during the first *I–V* sweeps are also area dependent (Appendix D). This electroforming-free characteristic of the *a*-STO_x synaptic devices can be associated with the higher concentration of as-grown oxygen vacancies,[40, 215] as discussed in the XPS analysis. Unlike our previously reported *a*-STO memristors,[70, 102] it is possible that during the first SET sweep the higher concentration of as-grown oxygen vacancies reduces their migration distance and electrical energy to form the nano-filament. **Figure 6.2**a shows a clockwise bipolar switching behavior which is typical for *a*-STO devices (*i.e.*, RESET on positive bias and SET on negative bias).[70, 98, 110]

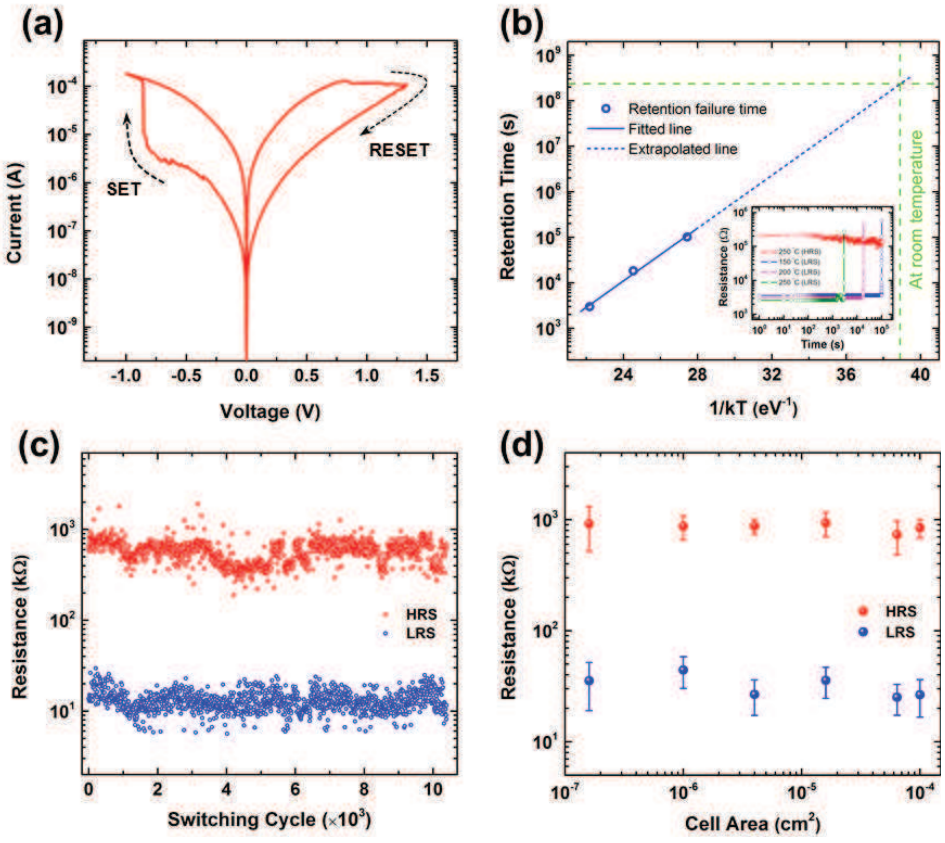

Figure 6.2 Electrical characterization of the *a*-STO_x synaptic devices. (a) The *I–V* characteristic sweep of a 10×10 μm^2 *a*-STO_x MIM device. (b) The retention time *vs* 1/kT plot to evaluate the state stability of the *a*-STO_x devices. The inset plot shows retention of LRS and HRS at different high temperatures ranging from 150 to 250 ˚C. (c) Endurance of the devices, where V_{RESET} of -1.6 V, V_{SET} of +1.4 V and V_{READ} of

+0.1 V are applied as a train of short pulses. (d) The dependence of HRS and LRS on the active cell area.

As depicted in Figure 6.2a, a negative triangular DC voltage sweep with amplitude of -1 V (as V_{SET}) switches the MIM device from its high resistance state (HRS) to a low resistance state (LRS). While an opposite polarity triangular DC voltage sweep with an amplitude of +1.3 V (as V_{RESET}) switches the device to its HRS. To evaluate the retentions of the MIM devices, the resistive states are measured at elevated temperatures ranging from 150 to 250 ˚C, as shown in the inset of Figure 6.2b. The retention of HRS measured for 30 hours at 250 ˚C shows no failure, indicating the stability of HRS. However, retention characteristics of LRS are temperature sensitive. This high temperature LRS retention failure can be associated with the thermally assisted reduction in the concentration of oxygen vacancies in the nano-filament and eventually its rupture.[216] The LRS retention failure time at different temperatures (where resistance jumps higher than the HRS) is plotted in an Arrhenius plot, as shown in Figure 2b, to calculate the oxygen vacancy migration activation energy and estimate the retention characteristics of the *a*-STO_x memristors. The extrapolation of the fitting line in Figure 6.2b estimates the retention time of *ca*. 7.6 years at room temperature. Even though, this retention is suitable for memory and neuromorphic applications, it can be improved by preventing the reoxidation of *a*-STO_x oxide layer through inserting a thin film exhibiting slow oxygen diffusion coefficient, such as Al_2O_3.[139] On the other hand, an active energy of *ca.* 0.29 eV is extracted from the linear fitting of the experimental data points in Figure 6.2b. This lower LRS activation energy, as compared to the other oxide systems [142, 216, 217] (*e.g.*, 1-1.6 eV reported for *a*-Al_2O_3, *a*-Ta_2O_5, *a*-Nb_2O_5 and TiO_2), suggests the hopping conduction mechanism in our *a*-STO_x MIM devices.[218] This hopping conduction refers to the electronic transport through the localized states where these states are provided by the oxygen vacancies in the nano-filament. To evaluate the switching repeatability of the *a*-STO_x synaptic devices (Figure 6.2c), short pulses with 1 μs duration and amplitude of -1.4 V and +1.6 V are applied for SET and RESET operations, respectively. While READ pulses with amplitude of +0.1 V and duration of 200 ns are used to measure the SET/RESET currents. The effect of pulse width on the switching performance is also evaluated (Appendix D). The endurance characteristics, for more than 10^4 switching cycles

(Figure 2c), indicate that the synaptic devices exhibit repeatable bipolar switching behavior. Generally in transition metal oxides, the bipolar resistive switching behavior is attributed to the inhomogeneous conduction mechanisms through the localized filamentary pathways and associated redox processes.[5, 28, 219, 220] As such, the resistance states (*i.e.*, HRS and LRS) are expected to be independent of the lateral dimensions of the MIM devices. Figure 6.2d reveals no appreciable area-dependency in our *a*-STO_x synaptic devices for either resistance state. This further supports our earlier statement regarding the formation of nano-filament in the synaptic MIM devices. We have conducted detailed characterization of filamentary conductive pathway through the cross-sectional microstructural analyses, as discussed in the following section.

6.4 Microstructural analysis of the synaptic devices

The physical structure of the *a*-STO_x synaptic devices and their compositional analysis is characterized with a cross-sectional transmission electron microscope (TEM). The electron energy loss spectroscopy (EELS) spectra are used to assess the distribution of oxygen content in the devices. The TEM micrograph and EELS spectra of a pristine device reveal an amorphous microstructure of the STO_x layer and a partial oxidation of the top Ti layer at the Ti/*a*-STO_x interface (Appendix D). The amorphous and oxygen deficient structure of STO_x layer is attributed to the room temperature sputtering in a pure argon environment which is consistent with our XPS analysis (Figure 6.1). Also, the partial oxidation of the top Ti layer to sub-oxide at Ti/*a*-STO_x interface can be associated with the interfacial oxygen diffusion and Ti–O bonding between deposited Ti and *a*-STO_x oxygen ions.[132, 221] **Figure 6.3**a shows an annular dark-field scanning TEM (STEM) image of a switching *a*-STO_x memristive device in its LRS. High color contrast regions are observed in the *a*-STO_x layer and along the top Ti/*a*-STO_x interface which indicate the applied electric field induced compositional changes in *a*-STO_x. To analyse the composition of the *a*-STO_x layer, a region of interest (ROI) is selected across the device, highlighted in Figure 3a. The EELS O–*K* edge area map (Figure 3b) shows the relative distribution of oxygen content in the ROI where the area map is generated by taking the O–*K* edge intensities of the collected spectra (at each pixel) after pre-edge background subtraction. The O–*K* edge area map reveals the presence of an oxygen deficient region extending between the top and bottom Pt electrodes. This

indicates a localized accumulation of oxygen vacancies and formation of filamentary path across the MIM structure.[110]

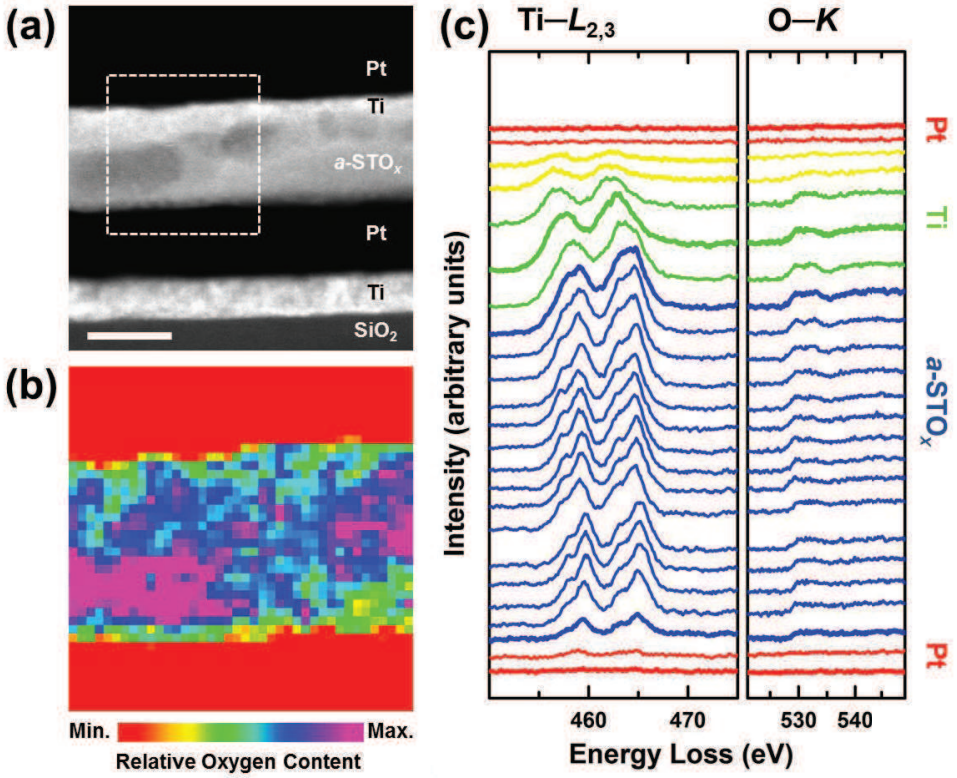

Figure 6.3 Microstructural and compositional analyses of the *a*-STO$_x$ synaptic devices. (a) STEM cross-section of a switching device in its LRS. Scale bar 20 nm. (b) The EELS O–*K* edge area map of the enclosed region of interest in (a). (c) The EELS Ti–$L_{2,3}$ and O–*K* edge profiles along a line scan across the filamentary region shown in (b).

The electronic character of the filamentary path is assessed by evaluating the oxidation state of Ti across the MIM structure. The generation of each oxygen vacancy in STO introduces two electrons into the Ti 3*d* orbital, and the resulting change in the Ti valence can be observed in the EELS Ti–$L_{2,3}$ edge profile.[136, 137] Figure 6.3c shows the background corrected Ti–$L_{2,3}$ and O–*K* spectra acquired along the EELS cross-sectional line scan passing over the filamentary region (indicated in Figure 6.3a). The gradual evolution of the Ti–$L_{2,3}$ fine structures in their intensity and position (from top Pt/Ti interface to the bottom Pt electrode) is clearly observed which indicates the change in Ti valence across the filamentary region. The O–*K* edge spectra are weak in intensity and exhibit low signal to noise ratio. Due to these resolution limitations we

evaluate only the Ti–$L_{2,3}$ edge profiles to qualitatively analyze the electronic structure of the filamentary region. The broad and relatively low intensity peaks at the top Pt/Ti interface indicate the presence of mixed Ti^{2+} and Ti^{3+} oxidation states.[132, 137, 138] At the Ti/*a*-STO_x interfacial region and in the *a*-STO_x layer, the crystal-field splitting of the Ti–L_3 and Ti–L_2 peaks (into t_{2g} and e_g peaks) and their shift can be attributed to the presence of Ti^{3+} and Ti^{4+} oxidation states.[222-224] It is well known that, in transition metal oxide based resistive memories, the resistive switching is attributed to the migration of oxygen vacancies and associated valence change in the transition metal cations.[28, 42] Our cross-sectional TEM analyses show that the extended oxygen deficient region with mixed Ti valence provides a conductive filamentary pathway for the charge transportation across the MIM structure

6.5 Implementation of the synaptic functions

Though the classical *p*-STDP model helped to establish fundamental understanding of the Hebbian synaptic plasticity (*i.e.*, time dependent pre- and post-synaptic spiking induces long- and short-term potentiation) in several neural systems but it is not sufficient to accurately model all biological experimental results produced by multiple (triplet and quadruplet) spikes.[206, 225] This can be associated with deficiencies in the classical *p*-STDP model, such as excluding non-linear integration of spike pairs and their repetition frequency to quantify the synaptic modification.[207, 225] This infers the classical *p*-STDP model cannot elicit the BCM synaptic learning rule, which is regarded as a possible explanation of experience-dependent synaptic plasticity.[207] On the other hand, the *t*-STDP model is believed to be comprehensive enough to explain the biological experimental results produced by multiple spikes. So implementation of the *t*-STDP rule on *a*-STO_x synaptic devices can highlight the capability of these artificial synapses to mimic the biological synaptic functionalities.

A typical biological synapse consists of a pre-synaptic neuron and a post-synaptic neuron connected through a synapse, as schematically illustrated in **Figure 6.4**a. In an artificial memristor based synaptic device, the bottom and top electrodes work as neurons and the switching layer acts as a synaptic connection. The electrical conductivity of the device interprets the synaptic weight, while its increase or decrease translates to potentiation or depression, respectively, in response to the applied voltage spikes. Figure 6.4b shows an experimental implementation of simplified *t*-STDP

learning rules as described in Ref.[206, 207] and also in **Equation 6.1,** using our *a*-STO_x memristor. Synaptic changes reported here (Figure 6.4b) are collected using application of different pulse magnitudes with fixed pulse widths. A time-to-digital-to-voltage circuitry (shown in Figure 6.6a and discussed later) is simulated to generate magnitude of the voltage pulses corresponding to the spike-timing information (Δt_1 and Δt_2). To verify the capability of this scheme to implement a wide range of learning rules, including *p*-STDP and *t*-STDP, we have applied a series of 100 pulses for each voltage magnitude that is chosen by the programming circuitry. The amplitude of applied voltage pulses for the corresponding spike-timing is listed in **Table D1,** Appendix D These experiments demonstrate a simple analog time-multiplexing implementation of artificial memristive synapses with shared peripheral circuitry. A simplified *t*-STDP learning rule,[206, 207] mentioned in Equation 6.1, suggests that synaptic depression is produced by spiking pairs with time interval of Δt_1 (as in classical *p*-STDP rule), while synaptic potentiation takes a triplet of spikes into account. Here we consider post-pre-post configuration of the triplet spikes, all details can be similarly applied for a pre-post-pre configuration.

It is also important to note that the asymmetry of the STDP window, shown in Figure 6.4b, is due to the asymmetry in potentiation and depression rates of the *a*-STO_x memristors and is consistent with several *in vivo* and *in vitro* STDP studies conducted on different types of biological synapses.[194]

A simplified *t*-STDP learning rule can be shown as,[207]

$$\begin{aligned} \Delta w^-(\Delta t_1) &= -A_1^- e^{(\Delta t_1/\tau_-)}, & \Delta t_1 < 0 \\ \Delta w^+(\Delta t_1, \Delta t_2) &= A_2^+ e^{(-\Delta t_1/\tau_+)} e^{(-\Delta t_2/\tau_y)}, & \Delta t_1 \geq 0, \Delta t_2 \geq 0 \end{aligned} \tag{6.1}$$

where $\Delta t_1 (= t^{\text{post}} - t^{\text{pre}})$ and $\Delta t_2 (= t^{\text{post1}} - t^{\text{post2}})$ are time differences. A_1^- and A_2^+ are constant amplitudes of each exponential term in potentiation (Δw^+) and depression (Δw^-) equations. The values of these amplitudes extracted from curve fitting (in Figure 6.4b) are $A_1^- = -0.70$ and $A_2^+ = 0.60$. Also, τ_+ and τ_- are time constants of Δw^+ and Δw^-, respectively, and obtained from the fitting parameters as $\tau_+ = 8.2$ ms and $\tau_- = 2.5$ ms. While the time constant τ_y indicates the exponential correlation between Δw^+ and Δt_2, and extracted as $\tau_y = 80$ ms. To reproduce the *t*-STDP window,

the values of Δt_2 are fixed at 10, 80 and 160 ms during the experiments (as shown in Figure 6.4).

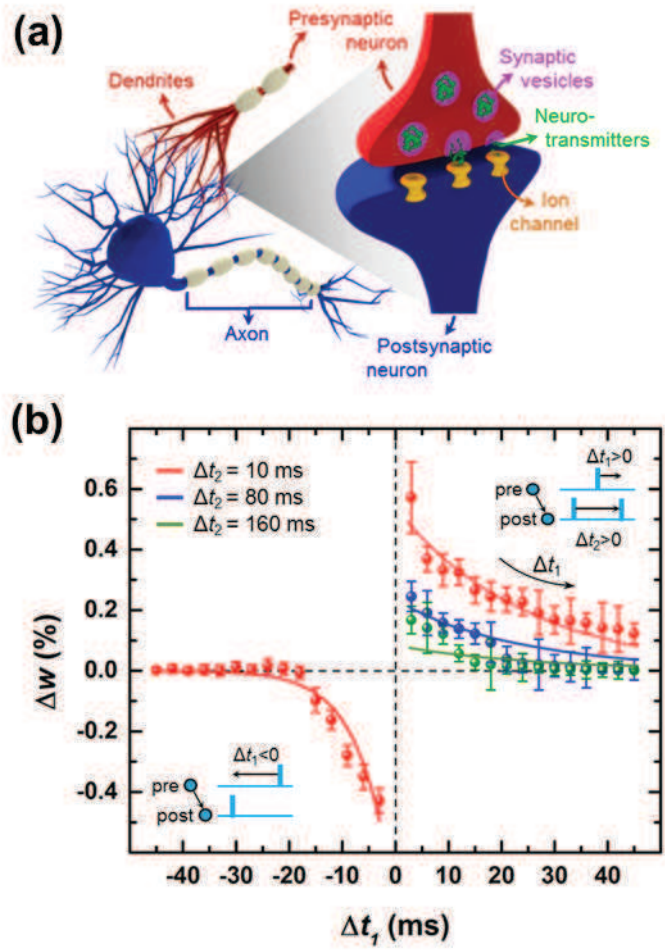

Figure 6.4 Triplet-based STDP window implemented on *a*-STO_x synaptic devices. (a) An illustration of two biological neurons connecting *via* synapses. (b) Artificial implementation of STDP learning rules using *a*-STO_x synaptic devices. Each data point and its deviation from mean (represented by bars) are collected by applying 100 cycles of identical pulses, where each cycle contains a RESET (for potentiation experiments) or SET (for depression experiments) pulse.

In order to demonstrate that our *a*-STO_x synaptic devices are capable to imitate the biological synaptic plasticity, we implement the *t*-STDP model (Equation 6.1) by following the experimental protocols reported by Pfister and Gerstner[206] and compare the results with the electrophysiological experiments performed in hippocampal culture[226] and visual cortex.[208] Two different triplet spiking patterns, namely post-

pre-post (*i.e.*, 1-pre-2-post) and pre-post-pre (*i.e.*, 2-pre-1-post), are used in hippocampal culture experiments,[226] each consists of 60 triplet of spikes and repeated at a given rate (1 Hz). The weight change as a function of timing difference between pre- and post-synaptic spikes in both triple patterns is graphically presented in **Figure** 6.5a and Figure 6.5b. The best fit is calculated by a normalized mean-square error function (E) represented as,[206]

$$E = \frac{1}{P}\sum_{i=1}^{P}\left(\frac{\Delta w_i^{exp} - \Delta w_i^{mem}}{\sigma_i}\right)^2 \tag{6.2}$$

where P, ΔW_i^{exp}, ΔW_i^{mem} and σ_i are the number of data points in a dataset, mean weight change (in electrophysiological and *a*-STO_x memristor experiments) and the standard error mean (SEM) of ΔW_i^{exp} for a given data point i, respectively. In the hippocampal culture, 13 data points are used, which includes 2 pairing and 3 quadruplet data points. To compare our experimental results with hippocampal culture, we use only 8 triplet data points, 4 for pre-post-pre triplet spiking pattern and 4 for post-pre-post triplet spiking pattern. The comparison of our *a*-STO_x memristor experimental results and hippocampal culture (Figure 5a and 5b) shows a very close match in the weight change associated to the respective time differences. The weight change corresponding to the both triplet pairing configurations is listed in **Table D2**, Appendix D.

Figure 6.5c shows the implementation of BCM learning rule where the synaptic weight changes as a function of the given frequency, ρ. The comparison of our experimental results with the visual cortex data set (Figure 6.5c) shows that *a*-STO_x memristors closely follow the BCM behavior for $\rho \leq 30$ Hz while for high frequencies our experimental results are within the variation limits of visual cortex data set. The values of synaptic weight change corresponding to different frequencies are listed in **Table D3**, Appendix D. This indicates that like time-dependent learning rules (*i.e.*, *p*-STDP and *t*-STDP); the BCM rule can also be implemented by our *a*-STO_x synaptic devices.

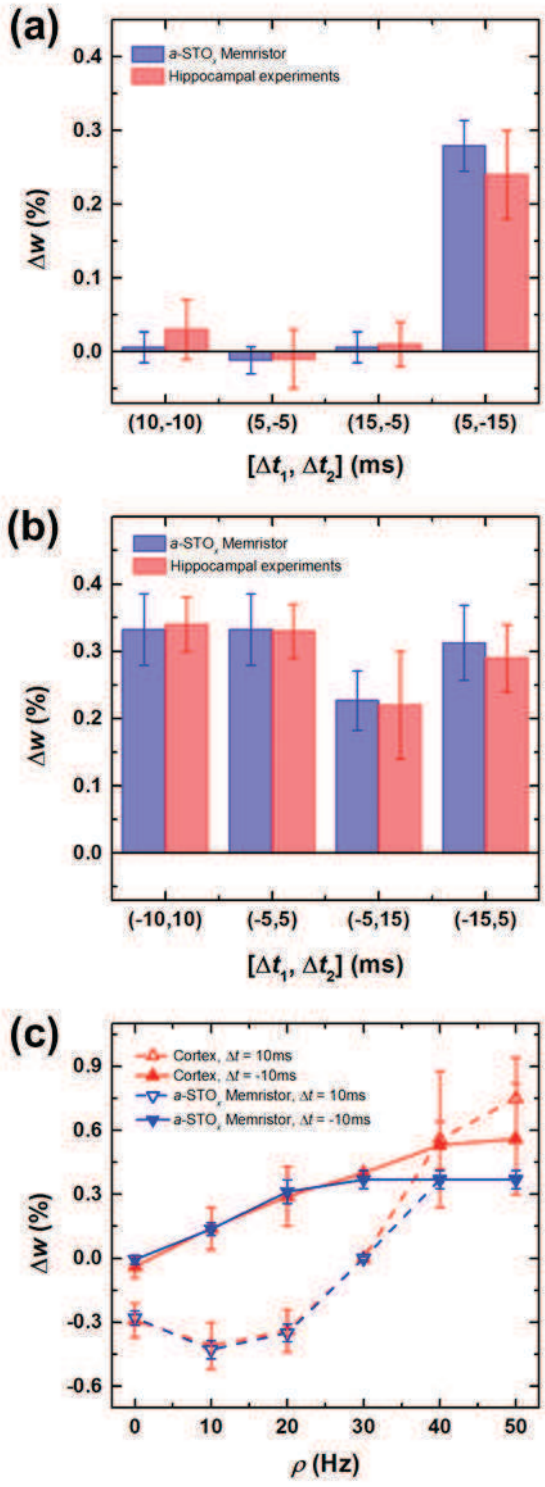

Figure 6.5 Reproduction analyses of the time- and rate-dependent learning rules. The reproduction of weight change induced by (a) pre- post- pre and (b) post- pre- post triplet spike patterns. (c) The synaptic weight change as a function of spike rate.

6.6 Design of CMOS drive circuitry

The available literature reports either extensive peripheral circuitry to generate suitable pre- and post-synaptic spike shapes (similar to the biological action potentials) or special circuits designed for a specific type of memristive system.[202, 227] Additionally, the direct interfacing between CMOS drive circuitry and memristive devices/array can expose them to CMOS circuit non-idealities.[228] Herein, we utilize a well-established CMOS circuit, called forward body biasing,[229-232] in combination with a time-to-digital converter to implement not only time dependent synaptic rules but also demonstrate the potential of implementing a wide variety of synaptic learning rules. **Figure 6.6a** shows a schematic of the proposed CMOS drive circuit which is a modification of the body-bias generator,[230, 231] and converts differences in input spike-timing into voltage amplitudes. The time-to-digital (T2D) module is responsible for the pre- and post-synaptic event digitization and includes a timing control unit and a decoder (Appendix D). The timing control unit is a fully digital unit that receives pre- and post-spikes and generates a binary code according to the timing intervals and works based on a number of counters that are triggered and stopped with spikes. It can be configured for multiple protocol implementation and Δt detection.[229] As depicted in Figure 6.6a, a finely tuned voltage (V_w) is generated to modify the weight of a memristor and is connected to a memristor array *via* a voltage follower (VF) and an array of transmission gates (TGs) that are connected to the top-electrodes (TEs) and bottom-electrodes (BEs) of the memristor array. It is worth mentioning that we focus on design of the peripheral circuitry for memristive artificial synapses, while modifications in the neuron designs may also be necessary to consider online-learning aspects of the learning rules discussed above. Each device in the array is individually accessible *via* an addressable top-electrode (TE) and bottom-electrode (BE) connections. Selections are mandated externally and also partially include some internal data. These selection signals are represented with two digital vectors for rows (R) and columns (C), *i.e.*, Sel_R and Sel_C respectively, in Figure 6.6a. Note that I_{ref} is a constant reference current that is supplied through a digital to analog converter (DAC), while V_{DDA} and V_{SSA} represent analog voltage supply and ground of the drive circuit, respectively. The proposed drive circuitry disconnects timing scales from the voltage level generation. Also the T2D

module is fully programmable and is capable of mapping any spike-timing to any binary code which can be translated to the corresponding voltage amplitude, *via* the DAC.

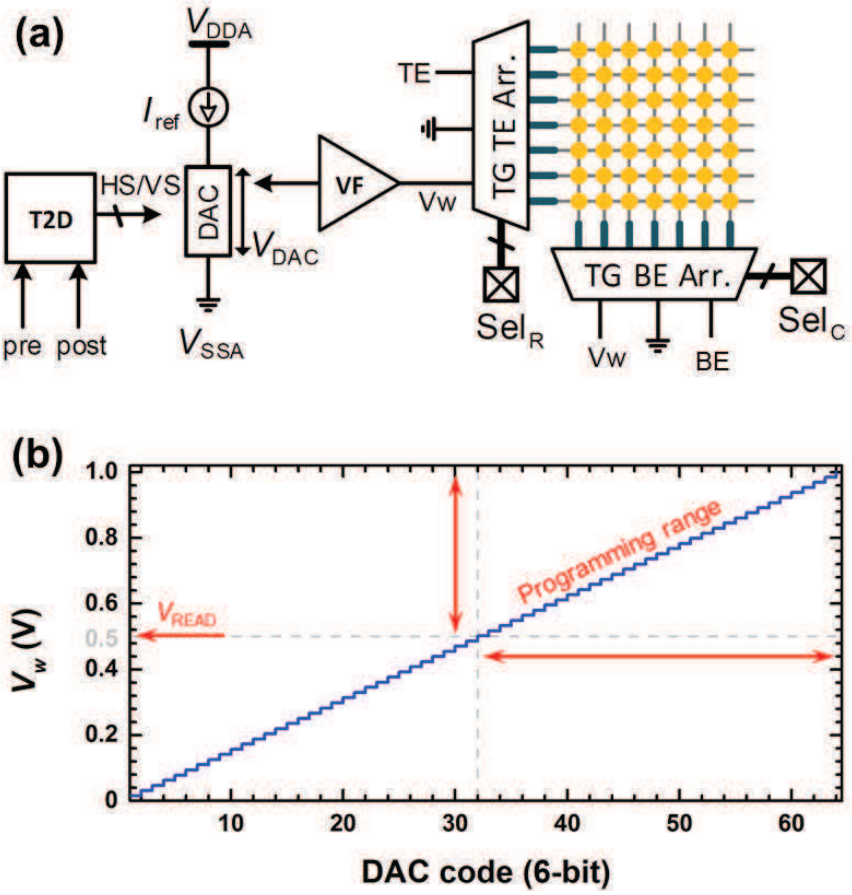

Figure 6.6 The CMOS drive circuitry. (a) A schematic of the proposed CMOS drive circuit which converts difference in input spike-timing into voltage amplitudes to modify the synaptic weight of a target memristor in the array. (b) Simulated resolution of the DAC circuitry to generate the weight changing voltage, *i.e.,* V_w.

As revealed in Figure 6.4b, near exponential relationship exists between the programming voltage amplitude (V_w) and synaptic weight change (Δw). This implies that a small variation in V_w can cause a significant deviation in Δw.Therefore, it is essential to estimate the programming efficiency of the proposed CMOS drive circuit. Figure 6.6b shows the Cadence simulation of the DAC circuitry using 90 nm CMOS technology. A 15.6 mV resolution of the V_{DAC} for a total 1 V supply is achieved. Figure 6.6b and Table D1 (Appendix D), shows overall mapping of spike-timing to DAC code and then to an equivalent voltage (V_w in this case). It has been reported that variation in V_w is less than 5 mV.[230, 231] Although the 15.6 mV increase in applied

voltage magnitudes even higher than the V_{READ} (*i.e.,* 0.5 V) do not necessarily switch the device, it is observed that such an increase makes a significant statistical change in Δw.

This shows that the forward transistor body biasing circuit is suitable for hybrid CMOS-memristor neuromorphic applications. Furthermore, by adopting this approach to experimentally emulate the *t*-STDP and BCM learning rules, it demonstrates a universal neuro-inspired programming scheme to implement a number of synaptic learning rules.

7 Conclusions and Future Work

The research work carried out in this dissertation aimed to engineer perovskite $SrTiO_3$ based resistive memories with dynamic switching characteristics and establish a comprehensive understanding of the underlying mechanisms. This chapter provides a brief summary of the significant outcomes of this research work and outlines the scope of future work in the field.

7.1 Conclusions

7.1.1 Controlled engineering of complex oxides

A novel methodology is established to synthesize CMOS compatible *a*-STO based resistive memories, on conventional substrates (*e.g.*, Si and SiO_2/Si). The control over synthesis parameters allowed engineering a variety of resistive switching behaviors in *a*-STO resistive memories.The *a*-STO thin films with control over their composition are successfully synthesized.

The un-doped *a*-STO thin films are tailored with different ratios of as-grown oxygen vacancies. This enabled to fabricate multi-layered oxide structures with distinct oxide-oxide interfaces. Moreover, acceptor and donor doped *a*-STO thin films with optimum concentration of dopant species are also realized. This allowed fabricating doped *a*-STO resistive memories to exhibit multi-state and multiple switching performances.

7.1.2 Realization of multi-state resistive switching

A detailed account of the structural and compositional properties of nano-filamentary resistive switching in the donor doped Nb:*a*-STO_x based devices. The role of substitutional Nb species in modulating the electronic structure and subsequent switching characteristics of these devices are provided. Key effects of dopant species are identified in bias/time and state dependence of volatile and non-volatile transport effects which can be instrumental for neuromorphic and adaptive computation applications. Overall, these results highlight the potential of disordered complex oxides as building blocks for memory and computing platforms. Also they provide guidelines for application specific engineering of memristive characteristics via structural and compositional design.

7.1.3 Multiple resistive switching behaviors

The presence of bipolar and threshold resistive switching behaviors in a single Pt/Ti/Cr:*a*-STO_x/Pt memory device have been shown. The multiple switching behaviors are defined by the current compliance limit during the initial electroforming step. The electroforming polarity-dependent bipolar and threshold resistive switching behaviors are also presented. In order to understand the existence of multiple resistive switching behaviors, rigorous compositional and micro/nano-structural analyses are carried out on the bare Cr:*a*-STO_x oxide and cross-sectional MIM devices. It is established that top Ti layer oxidized to a sub-stoichiometric oxide under the applied bias and introduces a Ti_2O_3/Cr:*a*-STO_x heterostructure in the MIM devices. Joule heating created local crystalline regions, provide a route for the migration of oxygen vacancies across the oxide heterostructure. Finally, to explain the observed multiple switching behaviors, a physical mechanism is proposed where current compliance during electroforming defines the concentration and distribution of oxygen vacancies in the heterostructure and the subsequent switching behaviors are combined effect of local redox reactions and Joule heating. The existence of multiple resistive switching behaviors in a Cr:*a*-STO_x

based memory cell and their addressability through a single physical parameter, *i.e.*, the current compliance during electroforming, opens new pathways for incorporation of memristors in ultra-dense memory architectures and conventional/non-conventional computation.

7.1.4 Multifunctional transparent resistive memories

Highly transparent ReRAM cells with bipolar switching behaviour are demonstrated. A bilayer stack of amorphous STO is utilized as the memory element sandwiched between transparent ITO electrodes. Comprehensive optical, electrical and compositional characterizations are conducted to propose a switching mechanism for the devices. The thickness of the bilayer stack is also varied to study its influence on the switching performance and to control the linearity in the switching behavior. Devices can be designed to exhibit a non-linear LRS which highlights their potential for large scale integration of *t*-ReRAM array. Additionally, the memory devices are shown to exhibit a transient photo-response in their HRS using a range of illumination wavelengths. Combining memristive properties with optically modulated HRS indicates the versatile functionality of such *t*-ReRAMs for optoelectronic applications such as photo-detectors/sensors.

7.1.5 Emulation of synaptic rules

A hybrid CMOS-memristor approach is demonstrated to practically emulate the synaptic functions. The CMOS-compatible *a*-STO_x memristors are used as artificial synapses. These synaptic devices exhibit electroforming-free characteristics. Higher order time-dependent and rate-dependent learning rules (discovered in the biological synapses) such as triple-STDP (*t*-STDP) and Bienenstosk Cooper Munro (BCM) have not been experimentally demonstrated on these artificial synaptic devices. Furthermore, a simple yet highly flexible CMOS drive circuit is presented rendering its capability to implement a variety of synaptic functions.

As such, the room temperature CMOS-compatible synthesis, electroforming-free characteristics of *a*-STO_x memristors and flexible design of the CMOS drive circuitry to demonstrate the realization of an efficient and reliable neuromorphic system are exploited.

7.2 Future Work

The research work carried out in this thesis has presented significant amount of insights into the fabrication and characteristics of novel perovskite oxide based resistive memories. But still there are several aspects remaining for the further investigations. A few significant research topics are listed below:

7.2.1 High performance memristive arrays

The micro-scale cross-point memristive devices with a variety of characteristics are fabricated and rigorously tested in this research work. All devices have shown reliable resistive switching performances and scaling potential as they exhibit nano-filamentary switching phenomena. Furthermore, the presence of multiple switching behaviors (bipolar and threshold resistive switching) in a single memory cell highlights the potential of these devices for large scale memory array. So the downscaling of these devices (to <100 nm device size) and integration into a large scale memory array is an opportunity to investigate the effect of physical parameters on the efficiency of their performance.

7.2.2 Multi-stimuli resistive memory

Transparent resistive memories with a transient photo-response have been demonstrated in this research work. The development of a resistive memory where its resistive states are optically, electrically and thermally tuneable will offer a versatile memory system with an extra degree of control over the switching characteristics. Moreover, the investigation of interplay between different stimuli will provide insights into the complex multifunctional properties of the perovskite oxides.

7.2.3 Efficient neuromorphic networks

A variety of synaptic learning rules have been implemented on the electroforming-free *a*-STO memristive devices. The comparison of experimental results with the biological data set shows that the *a*-STO memristive devices can successfully mimic the complex neural activities. As such, the development of an efficient neuromorphic network based on these memristive devices will serve as a step forward to realize a brain-on-chip.

References

1. Ramirez, A.P., *Oxide Electronics Emerge.* Science, 2007. **315**(5817): p. 1377.
2. Mannhart, J. and D.G. Schlom, *Oxide Interfaces—An Opportunity for Electronics.* Science, 2010. **327**(5973): p. 1607.
3. Menzel, S., et al., *Origin of the Ultra-nonlinear Switching Kinetics in Oxide-Based Resistive Switches.* Adv. Func. Mater., 2011. **21**(23): p. 4487-4492.
4. Muenstermann, R., et al., *Realization of regular arrays of nanoscale resistive switching blocks in thin films of Nb-doped $SrTiO_3$.* Appl. Phys. Lett., 2008. **93**(2): p. 023110.
5. Dittmann, R., et al., *Scaling Potential of Local Redox Processes in Memristive $SrTiO_3$ Thin-Film Devices.* Proc. IEEE, 2012. **100**(6): p. 1979-1990.
6. Menke, T., et al., *Impact of the electroforming process on the device stability of epitaxial Fe-doped $SrTiO_3$ resistive switching cells.* J. Appl. Phys., 2009. **106**(11): p. 114507.
7. Alexandrov, V.E., et al., *First-principles study of bulk and surface oxygen vacancies in $SrTiO_3$ crystal.* Eur. Phys. J. B, 2009. **72**(1): p. 53-57.
8. Rodenbücher, C., et al., *Cluster-like resistive switching of $SrTiO_3$:Nb surface layers.* New J. Phys., 2013. **15**(10): p. 103017.
9. Bhalla, A.S., R. Guo, and R. Roy, *The perovskite structure—a review of its role in ceramic science and technology.* Mater. Res. Innov., 2000. **4**(1): p. 3-26.
10. Panda, D. and T.-Y. Tseng, *Perovskite Oxides as Resistive Switching Memories: A Review.* Ferroelectrics, 2014. **471**(1): p. 23-64.
11. Ahmed, T., A. Vorobiev, and S. Gevorgian, *Growth temperature dependent dielectric properties of $BiFeO_3$ thin films deposited on silica glass substrates.* Thin Solid Films, 2012. **520**(13): p. 4470-4474.
12. Fergus, J.W., *Perovskite oxides for semiconductor-based gas sensors.* Sens. Actuators B. Chem., 2007. **123**(2): p. 1169-1179.
13. Piskunov, S., et al., *Bulk properties and electronic structure of $SrTiO_3$, $BaTiO_3$, $PbTiO_3$ perovskites: an ab initio HF/DFT study.* Comput. Mater. Sci., 2004. **29**(2): p. 165-178.

14. van Benthem, K., C. Elsässer, and R.H. French, *Bulk electronic structure of $SrTiO_3$: Experiment and theory.* J. Appl. Phys., 2001. **90**(12): p. 6156-6164.
15. Ueno, K., et al., *Electric-field-induced superconductivity in an insulator.* Nat. Mater., 2008. **7**(11): p. 855-858.
16. Jang, H.W., et al., *Ferroelectricity in Strain-Free $SrTiO_3$ Thin Films.* Phys. Rev. Lett., 2010. **104**(19): p. 197601.
17. Brinkman, A., et al., *Magnetic effects at the interface between non-magnetic oxides.* Nat. Mater., 2007. **6**(7): p. 493-496.
18. Longo, V.M., et al., *Structural conditions that leads to photoluminescence emission in SrTiO3: An experimental and theoretical approach.* J. Appl. Phys., 2008. **104**(2): p. 023515.
19. Cen, C., et al., *Nanoscale control of an interfacial metal-insulator transition at room temperature.* Nat. Mater., 2008. **7**(4): p. 298-302.
20. Muenstermann, R., et al., *Coexistence of filamentary and homogeneous resistive switching in Fe-doped $SrTiO_3$ thin-film memristive devices.* Adv. Mater., 2010. **22**(43): p. 4819-22.
21. Chan, N.H., R.K. Sharma, and D.M. Smyth, *Nonstoichiometry in $SrTiO_3$.* J. Electrochem. Soc., 1981. **128**(8): p. 1762-1769.
22. Baiatu, T., R. Waser, and K.H. Härdtl, *dc Electrical Degradation of Perovskite-Type Titanates: III, A Model of the Mechanism.* J. Am. Ceram. Soc., 1990. **73**(6): p. 1663-1673.
23. Akhtar, M.J., et al., *Computer Simulation Studies of Strontium Titanate.* J. Am. Ceram. Soc., 1995. **78**(2): p. 421-428.
24. Tanaka, T., et al., *First-principles study on structures and energetics of intrinsic vacancies in $SrTiO_3$.* Phys. Rev. B, 2003. **68**(20): p. 205213.
25. Crawford, J. and P. Jacobs, *Point Defect Energies for Strontium Titanate: A Pair-Potentials Study.* J. Solid State Chem., 1999. **144**(2): p. 423-429.
26. Meyer, R., et al., *Observation of Vacancy Defect Migration in the Cation Sublattice of Complex Oxides by ^{18}O Tracer Experiments.* Phys. Rev. Lett., 2003. **90**(10): p. 105901.
27. Tufte, O.N. and P.W. Chapman, *Electron Mobility in Semiconducting Strontium Titanate.* Phys. Rev., 1967. **155**(3): p. 796-802.
28. Waser, R., et al., *Redox-Based Resistive Switching Memories – Nanoionic Mechanisms, Prospects, and Challenges.* Adv. Mater., 2009. **21**(25-26): p. 2632-2663.
29. Luo, W., et al., *Structural and electronic properties of n-doped and p-doped $SrTiO_3$.* Phys. Rev. B, 2004. **70**(21): p. 214109.
30. Shanthi, N. and D.D. Sarma, *Electronic structure of electron doped $SrTiO_3$:$SrTiO_{3-\delta}$ and $Sr_{1-x}La_xTiO_3$.* Phys. Rev. B, 1998. **57**(4): p. 2153-2158.
31. Balachandran, U. and N.G. Eror, *Electrical conductivity in strontium titanate.* J. Solid State Chem., 1981. **39**(3): p. 351-359.
32. Campet, G., et al., *Influence of crystallinity and structural degects on the electronic properties of transparent and conductive $SrTiO_3$ films, amorphous or crystalline. Comparative study with ITO films.* Mater. Sci. Eng. B, 1991. **8**(1): p. 45-52.
33. Gerblinger, J. and H. Meixner, *Electrical conductivity of sputtered films of strontium titanate.* J. Appl. Phys., 1990. **67**(12): p. 7453-7459.
34. Tkach, A., et al., *Role of trivalent Sr substituents and Sr vacancies in tetragonal and polar states of $SrTiO_3$.* Acta Mater., 2011. **59**(14): p. 5388-5397.

35. Wei, W., et al., *Density functional characterization of the electronic structure and optical properties of Cr-doped $SrTiO_3$.* J. Phys. D: Appl. Phys., 2009. **42**(5): p. 055401.
36. Tomio, T., et al., *Control of electrical conductivity in laser deposited $SrTiO_3$ thin films with Nb doping.* J. Appl. Phys., 1994. **76**(10): p. 5886-5890.
37. Zhang, C., et al., *Substitutional position and insulator-to-metal transition in Nb-doped $SrTiO_3$.* Mater. Chem. Phys., 2008. **107**(2-3): p. 215-219.
38. Strukov, D.B., et al., *The missing memristor found.* Nature, 2008. **453**(7191): p. 80-3.
39. Strukov, D.B. and R.S. Williams, *Exponential ionic drift: fast switching and low volatility of thin-film memristors.* Appl. Phys. A, 2008. **94**(3): p. 515-519.
40. Joshua Yang, J., et al., *The mechanism of electroforming of metal oxide memristive switches.* Nanotechnology, 2009. **20**(21): p. 215201.
41. Ielmini, D., *Resistive switching memories based on metal oxides: mechanisms, reliability and scaling.* Semicond. Sci. Technol., 2016. **31**(6): p. 063002.
42. Menzel, S., et al., *Physics of the Switching Kinetics in Resistive Memories.* Adv. Func. Mater., 2015. **25**(40): p. 6306-6325.
43. Pan, F., et al., *Recent progress in resistive random access memories: Materials, switching mechanisms, and performance.* Mater. Sci. Eng. R Rep., 2014. **83**: p. 1-59.
44. Yang, Y. and W. Lu, *Nanoscale resistive switching devices: mechanisms and modeling.* Nanoscale, 2013. **5**(21): p. 10076-92.
45. Waser, R. and M. Aono, *Nanoionics-based resistive switching memories.* Nat. Mater., 2007. **6**(11): p. 833-840.
46. Janousch, M., et al., *Role of Oxygen Vacancies in Cr-Doped $SrTiO_3$ for Resistance-Change Memory.* Adv. Mater., 2007. **19**(17): p. 2232-2235.
47. Lee, M.J., et al., *A fast, high-endurance and scalable non-volatile memory device made from asymmetric Ta_2O_{5-x}/TaO_{2-x} bilayer structures.* Nat Mater, 2011. **10**(8): p. 625-30.
48. Choi, B.J., et al., *Trilayer Tunnel Selectors for Memristor Memory Cells.* Advanced Materials, 2015: p. n/a-n/a.
49. Wang, G., et al., *Three-Dimensional Networked Nanoporous Ta2O5–x Memory System for Ultrahigh Density Storage.* Nano Letters, 2015. **15**(9): p. 6009-6014.
50. Prezioso, M., et al., *Training and Operation of an Integrated Neuromorphic Network Based on Metal-Oxide Memristors.* Nature, 2015. **521**: p. 61-64.
51. Jo, S.H., et al., *Nanoscale memristor device as synapse in neuromorphic systems.* Nano letters, 2010. **10**(4): p. 1297-1301.
52. Miao, F., et al., *Continuous electrical tuning of the chemical composition of TaO x-based memristors.* ACS nano, 2012. **6**(3): p. 2312-2318.
53. Ziegler, M., et al., *An electronic version of Pavlov's dog.* Advanced Functional Materials, 2012. **22**(13): p. 2744-2749.
54. Kim, S., et al., *Experimental demonstration of a second-order memristor and its ability to biorealistically implement synaptic plasticity.* Nano Lett, 2015. **15**(3): p. 2203-11.
55. Tan, Z.-H., et al., *Synaptic Metaplasticity Realized in Oxide Memristive Devices.* Advanced Materials, 2016. **28**(2): p. 377-384.
56. Chen, P.-Y., et al. *Exploiting resistive cross-point array for compact design of physical unclonable function*. in *Hardware Oriented Security and Trust (HOST), 2015 IEEE International Symposium on*. 2015. IEEE.

57. Rajendran, J., et al. *Nano-PPUF: A memristor-based security primitive*. in *2012 IEEE Computer Society Annual Symposium on VLSI*. 2012. IEEE.
58. Rührmair, U., et al., *Applications of high-capacity crossbar memories in cryptography.* IEEE Transactions on Nanotechnology, 2011. **10**(3): p. 489-498.
59. Rainer, W., et al., *Redox-Based Resistive Switching Memories - Nanoionic Mechanisms, Prospects, and Challenges.* Advanced Materials, 2009. **21**.
60. Strukov, D. and H. Kohlstedt, *Resistive switching phenomena in thin films: Materials, devices, and applications.* Materials Research Society Bulletin, 2012. **37**.
61. Yang, J.J., D.B. Strukov, and D.R. Stewart, *Memristive devices for computing.* Nature nanotechnology, 2013. **8**(1): p. 13-24.
62. Miao, F., et al., *Observation of two resistance switching modes in TiO2 memristive devices electroformed at low current.* Nanotechnology, 2011. **22**(25): p. 254007.
63. Yang, J.J., et al., *Metal/TiO 2 interfaces for memristive switches.* Applied Physics A: Materials Science & Processing, 2011. **102**(4): p. 785-789.
64. Metlenko, V., et al., *Do dislocations act as atomic autobahns for oxygen in the perovskite oxide SrTiO3?* Nanoscale, 2014. **6**(21): p. 12864-12876.
65. Lenser, C., et al., *Formation and Movement of Cationic Defects During Forming and Resistive Switching in $SrTiO_3$ Thin Film Devices.* Adv. Func. Mater., 2015. **25**(40): p. 6360-6368.
66. Tsuruoka, T., et al., *Redox Reactions at Cu,Ag/Ta2O5 Interfaces and the Effects of Ta2O5 Film Density on the Forming Process in Atomic Switch Structures.* Advanced Functional Materials, 2015. **25**(40): p. 6374-6381.
67. Wedig, A., et al., *Nanoscale cation motion in TaOx, HfOx and TiOx memristive systems.* Nat Nano, 2015. **advance online publication**.
68. Moors, M., et al., *Resistive Switching Mechanisms on TaOx and SrRuO3 Thin-Film Surfaces Probed by Scanning Tunneling Microscopy.* ACS Nano, 2016. **10**(1): p. 1481-1492.
69. Nili, H., et al., *Nanoscale resistive switching in amorphous perovskite oxide (a-$SrTiO_3$) memristors.* Advanced Functional Materials, 2014. **24**(43): p. 6741-6750.
70. Nili, H., et al., *Donor-Induced Performance Tuning of Amorphous $SrTiO_3$ Memristive Nanodevices: Multistate Resistive Switching and Mechanical Tunability.* Adv. Func. Mater., 2015. **25**(21): p. 3172-3182.
71. Mikheev, E., et al., *Resistive switching and its suppression in Pt/Nb: SrTiO3 junctions.* Nature Communications, 2014. **5**: p. 3990.
72. Ielmini, D., R. Bruchhaus, and R. Waser, *Thermochemical resistive switching: materials, mechanisms, and scaling projections.* Phase Transitions, 2011. **84**(7): p. 570-602.
73. Lin, Y., et al., *Resistive switching mechanisms relating to oxygen vacancies migration in both interfaces in Ti/HfOx/Pt memory devices.* Journal of Applied Physics, 2013. **113**(6): p. 064510.
74. Bourim, E.M., Y. Kim, and D.W. Kim, *Interface State Effects on Resistive Switching Behaviors of Pt/Nb-Doped $SrTiO_3$ Single-Crystal Schottky Junctions.* ECS J. Solid State Sci. Technol., 2014. **3**(7): p. N95-N101.
75. Mikheev, E., et al., *Tailoring resistive switching in Pt/SrTiO3 junctions by stoichiometry control.* Scientific reports, 2015. **5**.
76. Kan, D., et al., *Blue-light emission at room temperature from Ar^+-irradiated $SrTiO_3$.* Nat. Mater., 2005. **4**(11): p. 816-819.

77. Pizani, P., et al., *Photoluminescence of disordered ABO_3 perovskites.* Applied Physics Letters, 2000. **77**: p. 824-826.
78. Pinheiro, C., et al., *The role of defect states in the creation of photoluminescence in SrTiO3.* Applied Physics A, 2003. **77**(1): p. 81-85.
79. Pontes, F., et al., *Photoluminescence at room temperature in amorphous $SrTiO_3$ thin films obtained by chemical solution deposition.* Materials Chemistry and Physics, 2003. **77**(2): p. 598-602.
80. Zhang, Z., W. Sigle, and M. Rühle, *Atomic and electronic characterization of the a [100] dislocation core in SrTiO 3.* Physical Review B, 2002. **66**(9): p. 094108.
81. Zhu, G.-z., G. Radtke, and G.A. Botton, *Bonding and structure of a reconstructed (001) surface of SrTiO3 from TEM.* Nature, 2012. **490**(7420): p. 384-387.
82. Qin, W., J. Hou, and D.A. Bonnell, *Effect of Interface Atomic Structure on the Electronic Properties of Nano-Sized Metal–Oxide Interfaces.* Nano letters, 2014. **15**(1): p. 211-217.
83. Hanzig, F., et al., *Crystallization dynamics and interface stability of strontium titanate thin films on silicon.* Journal of applied crystallography, 2015. **48**(2): p. 393-400.
84. Abramov, Y.A., et al., *The chemical bond and atomic displacements in SrTiO3 from X-ray diffraction analysis.* Acta Crystallographica Section B: Structural Science, 1995. **51**(6): p. 942-951.
85. Waser, R. and R. Hagenbeck, *Grain boundaries in dielectric and mixed-conducting ceramics.* Acta Materialia, 2000. **48**(4): p. 797-825.
86. Hagenbeck, R. and R. Waser, *Influence of temperature and interface charge on the grain-boundary conductivity in acceptor-doped SrTiO3 ceramics.* Journal of Applied Physics, 1998. **83**(4): p. 2083-2092.
87. De Souza, R.A., *The formation of equilibrium space-charge zones at grain boundaries in the perovskite oxide $SrTiO_3$.* Physical Chemistry Chemical Physics, 2009. **11**(43): p. 9939-9969.
88. Dittmann, R., et al., *Scaling Potential of Local Redox Processes in Memristive $SrTiO_3$ Thin-Film Devices.* Proceedings of the IEEE, 2012. **100**: p. 1979-1990.
89. Meyer, R., et al., *Observation of Vacancy Defect Migration in the Cation Sublattice of Complex Oxides by ^{18}O Tracer Experiments.* Physical Review Letters, 2003. **90**(10): p. 105901.
90. Vollmann, M. and R. Waser, *Grain boundary defect chemistry of acceptor-doped titanates: high field effects.* Journal of Electroceramics, 1997. **1**(1): p. 51-64.
91. Bourim, E.M., Y. Kim, and D.-W. Kim, *Interface State Effects on Resistive Switching Behaviors of Pt/Nb-Doped SrTiO3 Single-Crystal Schottky Junctions.* ECS Journal of Solid State Science and Technology, 2014. **3**(7): p. N95-N101.
92. Messerschmitt, F., et al., *Memristor Kinetics and Diffusion Characteristics for Mixed Anionic-Electronic $SrTiO_{3-\delta}$ Bits: The Memristor-Based Cottrell Analysis Connecting Material to Device Performance.* Advanced Functional Materials, 2014. **24**(47): p. 7448-7460.
93. La Barbera, S., D. Vuillaume, and F. Alibart, *Filamentary Switching: Synaptic Plasticity through Device Volatility.* ACS nano, 2015. **9**(1): p. 941-949.
94. Chen, J.Y., et al., *Switching Kinetic of VCM-Based Memristor: Evolution and Positioning of Nanofilament.* Adv. Mater., 2015. **27**(34): p. 5028-33.

95. Yang, J.J., et al., *Metal oxide memories based on thermochemical and valence change mechanisms.* MRS Bulletin, 2012. **37**(02): p. 131-137.
96. Kwon, D.H., et al., *Atomic structure of conducting nanofilaments in TiO_2 resistive switching memory.* Nat. Nanotechnol., 2010. **5**(2): p. 148-53.
97. Yoon, K.J., et al., *Evolution of the shape of the conducting channel in complementary resistive switching transition metal oxides.* Nanoscale, 2014. **6**(4): p. 2161-9.
98. Nili, H., et al., *Nanoscale Resistive Switching in Amorphous Perovskite Oxide (a-$SrTiO_3$) Memristors.* Adv. Func. Mater., 2014. **24**(43): p. 6741-6750.
99. Breuer, T., et al., *Low-current operations in $4F^2$-compatible Ta_2O_5-based complementary resistive switches.* Nanotechnology, 2015. **26**(41): p. 415202.
100. Balatti, S., et al., *Multiple memory states in resistive switching devices through controlled size and orientation of the conductive filament.* Adv. Mater., 2013. **25**(10): p. 1474-8.
101. Messerschmitt, F., et al., *Memristor Kinetics and Diffusion Characteristics for Mixed Anionic-Electronic $SrTiO_{3-\delta}$ Bits: The Memristor-Based Cottrell Analysis Connecting Material to Device Performance.* Adv. Func. Mater., 2014. **24**(47): p. 7448-7460.
102. Ahmed, T., et al., *Transparent Amorphous Strontium Titanate Resistive Memories with Transient Photo-Response.* Nanoscale, 2017. **9**(38): p. 14690-702.
103. Lee, S.B., et al., *Reversible changes between bipolar and unipolar resistance-switching phenomena in a Pt/$SrTiO_x$/Pt cell.* Curr. Appl. Phys., 2012. **12**(6): p. 1515-1517.
104. Sun, X., et al., *Coexistence of the bipolar and unipolar resistive switching behaviours in Au/$SrTiO_3$/Pt cells.* J. Phys. D Appl. Phys., 2011. **44**(12): p. 125404.
105. Cai, H.L., X.S. Wu, and J. Gao, *Effect of oxygen content on structural and transport properties in $SrTiO_{3-x}$ thin films.* Chem. Phys. Lett., 2009. **467**(4-6): p. 313-317.
106. Tonda, S., et al., *Synthesis of Cr and La-codoped $SrTiO_3$ nanoparticles for enhanced photocatalytic performance under sunlight irradiation.* Phys. Chem. Chem. Phys., 2014. **16**(43): p. 23819-28.
107. Yu, H., et al., *Sol–gel hydrothermal synthesis of visible-light-driven Cr-doped SrTiO3 for efficient hydrogen production.* J. Mater. Chem., 2011. **21**(30): p. 11347.
108. Wang, D., et al., *Photophysical and Photocatalytic Properties of $SrTiO_3$ Doped with Cr Cations on Different Sites.* J. Phys. Chemis. B, 2006. **110**(32): p. 15824-15830.
109. Funabiki, F., T. Kamiya, and H. Hosono, *Doping effects in amorphous oxides.* J. Ceram. Soc. Jpn., 2012. **120**(11): p. 447-457.
110. Nili, H., et al., *Microstructure and dynamics of vacancy-induced nanofilamentary switching network in donor doped $SrTiO_{3-x}$ memristors.* Nanotechnology, 2016. **27**(50): p. 505210.
111. Soledade, L.E.B., et al., *Room-temperature photoluminescence in amorphous $SrTiO_3$ - the influence of acceptor-type dopants.* Appl. Phys. A: Mater. Sci. Process., 2002. **75**(5): p. 629-632.
112. Goldenberg, E., et al., *Effect of O_2/Ar flow ratio and post-deposition annealing on the structural, optical and electrical characteristics of $SrTiO_3$ thin films*

deposited by RF sputtering at room temperature. Thin Solid Films, 2015. **590**: p. 193-199.
113. Pontes, F.M., et al., *Photoluminescence at room temperature in amorphous $SrTiO_3$ thin films obtained by chemical solution deposition.* Mater. Chem.Phys., 2003. **77**(2): p. 598-602.
114. Orhan, E., et al., *Origin of photoluminescence in $SrTiO_3$: a combined experimental and theoretical study.* J. Solid State Chem., 2004. **177**(11): p. 3879-3885.
115. Yu, H., et al., *Elements doping to expand the light response of $SrTiO_3$.* J. Photochem. Photobiol. A Chem., 2014. **275**: p. 65-71.
116. La Mattina, F., et al., *Detection of charge transfer processes in Cr-doped $SrTiO_3$ single crystals.* Appl. Phys. Lett., 2008. **93**(2): p. 022102.
117. Comes, R.B., et al., *Visible light carrier generation in co-doped epitaxial titanate films.* Appl. Phys. Lett., 2015. **106**(9): p. 092901.
118. Linn, E., et al., *Complementary resistive switches for passive nanocrossbar memories.* Nat. Mater., 2010. **9**(5): p. 403-6.
119. Yu, S., et al., *Read/write schemes analysis for novel complementary resistive switches in passive crossbar memory arrays.* Nanotechnology, 2010. **21**(46): p. 465202.
120. Tappertzhofen, S., et al., *Capacity based nondestructive readout for complementary resistive switches.* Nanotechnology, 2011. **22**(39): p. 395203.
121. Gao, S., et al., *Implementation of Complete Boolean Logic Functions in Single Complementary Resistive Switch.* Sci. Rep., 2015. **5**: p. 15467.
122. Wang, Z.Q., et al. *Cycling-induced degradation of metal-oxide resistive switching memory (RRAM)*. in *2015 IEEE International Electron Devices Meeting (IEDM)*. 2015.
123. Balatti, S., et al. *Pulsed cycling operation and endurance failure of metal-oxide resistive (RRAM)*. in *2014 IEEE International Electron Devices Meeting*. 2014.
124. Kan, D. and Y. Shimakawa, *Transient behavior in Pt/Nb-doped SrTiO3 Schottky junctions.* Appl. Phys. Lett., 2013. **103**(14): p. 142910.
125. Park, W.Y., et al., *A $Pt/TiO_2/Ti$ Schottky-type selection diode for alleviating the sneak current in resistance switching memory arrays.* Nanotechnology, 2010. **21**(19): p. 195201.
126. Sawa, A., *Resistive switching in transition metal oxides.* Mater. Today, 2008. **11**(6): p. 28-36.
127. Szot, K., et al., *Switching the electrical resistance of individual dislocations in single-crystalline $SrTiO_3$.* Nat. Mater., 2006. **5**(4): p. 312-20.
128. Baeumer, C., et al., *Quantifying redox-induced Schottky barrier variations in memristive devices via in operando spectromicroscopy with graphene electrodes.* Nat. Comm., 2016. **7**: p. 12398.
129. Lee, W., et al., *Resistance switching behavior of atomic layer deposited $SrTiO_3$ film through possible formation of $Sr_2Ti_6O_{13}$ or $Sr_1Ti_{11}O_{20}$ phases.* Sci. Rep., 2016. **6**: p. 20550.
130. Kwon, J., et al., *Oxygen Vacancy Creation, Drift, and Aggregation in TiO_2-Based Resistive Switches at Low Temperature and Voltage.* Adv. Func. Mater., 2015. **25**(19): p. 2876-2883.
131. Meng Lu, Y., et al., *Impact of Joule heating on the microstructure of nanoscale TiO2 resistive switching devices.* J. Appl. Phys., 2013. **113**(16): p. 163703.

132. Li, Y., et al., *Nanoscale Chemical and Valence Evolution at the Metal/Oxide Interface: A Case Study of Ti/$SrTiO_3$.* Adv. Mater. Interf., 2016. **3**(17): p. 1600201.
133. Stille, S., et al., *Detection of filament formation in forming-free resistive switching $SrTiO_3$ devices with Ti top electrodes.* Appl. Phys. Lett., 2012. **100**(22): p. 223503.
134. Yang, J.J., et al., *Diffusion of adhesion layer metals controls nanoscale memristive switching.* Adv. Mater., 2010. **22**(36): p. 4034-8.
135. Jeong, H.Y., et al., *Role of interface reaction on resistive switching of metal/amorphous TiO_2/Al RRAM devices.* J. Electrochem. Soc., 2011. **158**(10): p. H979-H982.
136. Muller, D.A., et al., *Atomic-scale imaging of nanoengineered oxygen vacancy profiles in $SrTiO_3$.* Nature, 2004. **430**(7000): p. 657-661.
137. Sanchez-Santolino, G., et al., *Characterization of surface metallic states in $SrTiO_3$ by means of aberration corrected electron microscopy.* Ultramicroscopy, 2013. **127**: p. 109-13.
138. Stoyanov, E., F. Langenhorst, and G. Steinle-Neumann, *The effect of valence state and site geometry on Ti $L_{3,2}$ and O K electron energy-loss spectra of Ti_xO_y phases.* Am. Mineral., 2007. **92**(4): p. 577-586.
139. Baeumer, C., et al., *Verification of redox-processes as switching and retention failure mechanisms in Nb:$SrTiO_3$/metal devices.* Nanoscale, 2016. **8**(29): p. 13967-75.
140. Meijer, G.I., et al., *Valence states of Cr and the insulator-to-metal transition in Cr-dopedSrTiO$_3$.* Phys. Rev. B, 2005. **72**(15): p. 155102.
141. Kim, T., et al., *Thickness-dependent resistance switching in Cr-doped $SrTiO_3$.* J. Korean Phys. Soc., 2012. **61**(5): p. 754-758.
142. Miao, F., et al., *Observation of two resistance switching modes in TiO_2 memristive devices electroformed at low current.* Nanotechnology, 2011. **22**(25): p. 254007.
143. Cho, E., et al., *First-principles study of point defects in rutileTiO_{2-x}.* Phys. Rev. B, 2006. **73**(19).
144. Tanaka, T., et al., *First-principles study on structures and energetics of intrinsic vacancies in$SrTiO_3$.* Phys. Rev. B, 2003. **68**(20).
145. Andreasson, B.P., et al., *Spatial distribution of oxygen vacancies in Cr-doped $SrTiO_3$ during an electric-field-driven insulator-to-metal transition.* Appl. Phys. Lett., 2009. **94**(1): p. 013513.
146. Shang, J., et al., *Thermally Stable Transparent Resistive Random Access Memory based on All-Oxide Heterostructures.* Adv. Func.l Mater., 2014. **24**(15): p. 2171-2179.
147. Tan, H., et al., *An optoelectronic resistive switching memory with integrated demodulating and arithmetic functions.* Adv. Mater., 2015. **27**(17): p. 2797-803.
148. Ungureanu, M., et al., *A light-controlled resistive switching memory.* Adv. Mater., 2012. **24**(18): p. 2496-500.
149. Bera, A., et al., *A Versatile Light-Switchable Nanorod Memory: Wurtzite ZnO on Perovskite $SrTiO_3$.* Adv. Func. Mater., 2013. **23**(39): p. 4977-4984.
150. Yao, J., et al., *Two-terminal nonvolatile memories based on single-walled carbon nanotubes.* ACS Nano, 2009. **3**(12): p. 4122-6.
151. Yao, J., et al., *Highly transparent nonvolatile resistive memory devices from silicon oxide and graphene.* Nat. Commun., 2012. **3**: p. 1101.

152. He, C., et al., *Tunable electroluminescence in planar graphene/SiO_2 memristors.* Adv. Mater., 2013. **25**(39): p. 5593-8.
153. Roy, K., et al., *Graphene-MoS_2 hybrid structures for multifunctional photoresponsive memory devices.* Nat. Nanotechnol., 2013. **8**(11): p. 826-30.
154. Yang, Y., S. Choi, and W. Lu, *Oxide heterostructure resistive memory.* Nano Lett., 2013. **13**(6): p. 2908-15.
155. Lee, M.J., et al., *A fast, high-endurance and scalable non-volatile memory device made from asymmetric Ta_2O_{5-x}/TaO_{2-x} bilayer structures.* Nat. Mater., 2011. **10**(8): p. 625-30.
156. You, T., et al., *Exploiting Memristive $BiFeO_3$ Bilayer Structures for Compact Sequential Logics.* Adv. Func. Mater., 2014. **24**(22): p. 3357-3365.
157. Siemon, A., et al., *Realization of Boolean Logic Functionality Using Redox-Based Memristive Devices.* Adv. Func. Mater., 2015. **25**(40): p. 6414-6423.
158. Shirley, D.A., *High-Resolution X-Ray Photoemission Spectrum of the Valence Bands of Gold.* Phys. Rev. B, 1972. **5**(12): p. 4709-4714.
159. Zakrzewska, K., *Nonstoichiometry in Studied by Ion Beam Methods and Photoelectron Spectroscopy.* Adv. Mater. Sci. Eng., 2012. **2012**: p. 13.
160. Heide, P.A.W.v.d., et al., *X-ray photoelectron spectroscopic and ion scattering study of the $SrTiO_3$ (001) surface.* Surf. Sci., 2001. **473**: p. 59-70.
161. Scigaj, M., et al., *Conducting interfaces between amorphous oxide layers and $SrTiO_3$(110) and $SrTiO_3$(111).* Solid State Ionics, 2015. **281**: p. 68-72.
162. Pinheiro, C.D., et al., *The role of defect states in the creation of photoluminescence in $SrTiO_3$.* Appl. Phys. A: Mater.Sci. Process., 2003. **77**(1): p. 81-85.
163. Morii, K., et al., *Dielectric relaxation in amorphous thin films of $SrTiO_3$ at elevated temperatures.* J. Appl. Phys., 1995. **78**(3): p. 1914.
164. Kumar, D. and R.C. Budhani, *Defect-induced photoluminescence of strontium titanate and its modulation by electrostatic gating.* Phys. Rev. B, 2015. **92**(23): p. 2351151-6.
165. Yasuda, H. and Y. Kanemitsu, *Dynamics of nonlinear blue photoluminescence and Auger recombination in$SrTiO_3$.* Phys. Rev. B, 2008. **77**(19): p. 193202.
166. Kan, D., et al., *Blue luminescence from electron-doped $SrTiO_3$.* Appl. Phys. Lett., 2006. **88**(19): p. 191916.
167. Yang, J.J., D.B. Strukov, and D.R. Stewart, *Memristive devices for computing.* Nat. Nanotechnol., 2013. **8**(1): p. 13-24.
168. Joshua Yang, J., et al., *Engineering nonlinearity into memristors for passive crossbar applications.* Appl. Phys. Lett., 2012. **100**(11): p. 113501.
169. Kim, K.H., et al., *A functional hybrid memristor crossbar-array/CMOS system for data storage and neuromorphic applications.* Nano Lett., 2012. **12**(1): p. 389-95.
170. Wen-Fa, W., C. Bi-Shiou, and H. Shu-Ta, *Effect of sputtering power on the structural and optical properties of RF magnetron sputtered ITO films.* Semicond. Sci. Technol., 1994. **9**(6): p. 1242.
171. Vaufrey, D., et al., *ITO-on-top organic light-emitting devices: a correlated study of opto-electronic and structural characteristics.* Semicond. Sci. Technol., 2003. **18**(4): p. 253.
172. Lan, Y.-F., et al., *Microstructural characterization of high-quality indium tin oxide films deposited by thermionically enhanced magnetron sputtering at low temperature.* Vacuum, 2014. **107**: p. 56-61.

173. Sunde, T.O.L., et al., *Transparent and conducting ITO thin films by spin coating of an aqueous precursor solution.* J. Mater. Chem., 2012. **22**(31): p. 15740.
174. Mochizuki, S., F. Fujishiro, and S. Minami, *Photoluminescence and reversible photo-induced spectral change of $SrTiO_3$.* J. Phys. Condens. Matter, 2005. **17**(6): p. 923-948.
175. Lee, J.H., et al., *A study of threshold switching of NbO2 using atom probe tomography and transmission electron microscopy.* Micron, 2015. **79**: p. 101-9.
176. Pickett, M.D., et al., *Coexistence of memristance and negative differential resistance in a nanoscale metal-oxide-metal system.* Adv. Mater., 2011. **23**(15): p. 1730-3.
177. Sung, K.D., et al., *Intriguing photoconductivity behaviors of $SrTiO_{3-\delta}$ thin films with Pt contacts.* Solid State Commun., 2011. **151**(23): p. 1784-1786.
178. Rossella, F., et al., *Photoconductivity and the structural phase transition in $SrTiO_3$.* Solid State Commun., 2007. **141**(2): p. 95-98.
179. Zhao, K., et al., *Ultraviolet fast-response photoelectric effect in tilted orientation $SrTiO_3$ single crystals.* Appl. Phys. Lett., 2006. **89**(17): p. 173507.
180. Liu, X.Z., B.W. Tao, and Y.R. Li, *Effect of oxygen vacancies on nonlinear dielectric properties of SrTiO3 thin films.* J. Mater. Sci., 2007. **42**(1): p. 389-392.
181. Ni, M.C., et al., *Resistive switching effect in $SrTiO_{3-\delta}$/Nb-doped $SrTiO_3$ heterojunction.* Appl. Phys. Lett., 2007. **91**(18): p. 183502.
182. Tan, H., et al., *Oxygen Vacancy Enhanced Photocatalytic Activity of Pervoskite $SrTiO_3$.* ACS Appl. Mater. Interfaces, 2014. **6**(21): p. 19184-19190.
183. Janotti, A., et al., *Vacancies and small polarons in $SrTiO_3$.* Phys. Rev. B, 2014. **90**(8): p. 0852021-6.
184. Tebano, A., et al., *Room-Temperature Giant Persistent Photoconductivity in $SrTiO_3/LaAlO_3$ Heterostructures.* ACS Nano, 2012. **6**(2): p. 1278-1283.
185. Tarun, M.C., F.A. Selim, and M.D. McCluskey, *Persistent photoconductivity in strontium titanate.* Phys. Rev. Lett., 2013. **111**(18): p. 187403.
186. Shang, D.S., et al., *Resistance dependence of photovoltaic effect in $Au/SrTiO_3$:Nb(0.5wt%) Schottky junctions.* Appl. Phys. Lett., 2008. **93**(17): p. 172119.
187. Bridoux, G., et al., *Light-induced metal-insulator transition in$SrTiO_3$ by photoresistance spectroscopy.* Phys. Rev. B, 2015. **92**(15): p. 155202.
188. Zhao, K., et al., *Ultraviolet photovoltage characteristics of $SrTiO_{3-\delta}$/Si heterojunction.* Appl. Phys. Lett., 2005. **86**(22): p. 221917.
189. Borghetti, J., et al., *Optoelectronic Switch and Memory Devices Based on Polymer-Functionalized Carbon Nanotube Transistors.* Adv. Mater., 2006. **18**(19): p. 2535-2540.
190. Royer, S. and D. Pare, *Conservation of total synaptic weight through balanced synaptic depression and potentiation.* Nature, 2003. **422**(6931): p. 518-522.
191. Kavalali, E.T., *The mechanisms and functions of spontaneous neurotransmitter release.* Nat. Rev. Neurosci., 2015. **16**(1): p. 5-16.
192. Feldman, D.E., *The spike timing dependence of plasticity.* Neuron, 2012. **75**(4): p. 556-571.
193. Sen, S., K.D. Miller, and L.F. Abbott, *Competitive Hebbian learning through spike-timing-dependent synaptic plasticity.* Nat. Neurosci., 2000. **3**(9): p. 919-26.
194. Caporale, N. and Y. Dan, *Spike timing–dependent plasticity: a Hebbian learning rule.* Annu. Rev. Neurosci., 2008. **31**: p. 25-46.

195. van Rossum, M.C.W., G.Q. Bi, and G.G. Turrigiano, *Stable Hebbian Learning from Spike Timing-Dependent Plasticity.* J. Neurosci., 2000. **20**: p. 8812-8821.
196. Abbott, L.F. and S.B. Nelson, *Synaptic plasticity: taming the beast.* Nat. Neurosci., 2000. **3 Suppl 1**(11s): p. 1178-83.
197. Türel, Ö., et al., *Neuromorphic architectures for nanoelectronic circuits.* Int. J. Circ. Theor. App., 2004. **32**(5): p. 277-302.
198. Hutchby, J.A., et al., *Extending the road beyond CMOS.* IEEE Circuits Devices Mag., 2002. **18**(2): p. 28-41.
199. Jo, S.H., et al., *Nanoscale memristor device as synapse in neuromorphic systems.* Nano. Lett., 2010. **10**(4): p. 1297-301.
200. Zamarreno-Ramos, C., et al., *On spike-timing-dependent-plasticity, memristive devices, and building a self-learning visual cortex.* Front. Neurosci., 2011. **5**: p. 26.
201. Serrano-Gotarredona, T., et al., *STDP and STDP variations with memristors for spiking neuromorphic learning systems.* Front. Neurosci., 2013. **7**: p. 1-15.
202. Chakrabarti, B., et al., *A multiply-add engine with monolithically integrated 3D memristor crossbar/CMOS hybrid circuit.* Sci. Rep., 2017. **7**: p. 42429.
203. Prezioso, M., et al., *Training and operation of an integrated neuromorphic network based on metal-oxide memristors.* Nature, 2015. **521**(7550): p. 61-4.
204. Wang, Z., et al., *Memristors with diffusive dynamics as synaptic emulators for neuromorphic computing.* Nat. Mater., 2017. **16**(1): p. 101-108.
205. Wang, Z., et al., *Nanoionics-Enabled Memristive Devices: Strategies and Materials for Neuromorphic Applications.* Adv. Electron. Mater., 2017: p. 1600510.
206. Pfister, J.P. and W. Gerstner, *Triplets of spikes in a model of spike timing-dependent plasticity.* J. Neurosci., 2006. **26**(38): p. 9673-82.
207. Gjorgjieva, J., et al., *A triplet spike-timing-dependent plasticity model generalizes the Bienenstock-Cooper-Munro rule to higher-order spatiotemporal correlations.* Proc. Natl. Acad. Sci. USA, 2011. **108**(48): p. 19383-8.
208. Sjöström, P.J., G.G. Turrigiano, and S.B. Nelson, *Rate, Timing, and Cooperativity Jointly Determine Cortical Synaptic Plasticity.* Neuron, 2001. **32**(6): p. 1149-1164.
209. Azghadi, M.R., et al., *A Hybrid CMOS-Memristor Neuromorphic Synapse.* IEEE Trans. Biomed. Circuits Syst., 2017. **11**(2): p. 434-445.
210. Aghnout, S., G. Karimi, and M.R. Azghadi, *Modeling triplet spike-timing-dependent plasticity using memristive devices.* J. Comput. Electron., 2017. **16**(2): p. 401-410.
211. Cai, W., F. Ellinger, and R. Tetzlaff, *Neuronal Synapse as a Memristor: Modeling Pair- and Triplet-Based STDP Rule.* IEEE Trans. Biomed. Circuits Syst., 2015. **9**(1): p. 87-95.
212. Ehre, D., et al., *X-ray photoelectron spectroscopy of amorphous and quasiamorphous phases of $BaTiO_3$ and $SrTiO_3$.* Phys.l Rev. B, 2008. **77**(18): p. 184106.
213. Nagarkar, P.V., P.C. Searson, and F.D. Gealy, *Effect of surface treatment on $SrTiO_3$: An x-ray photoelectron spectroscopic study.* J. Appl. Phys., 1991. **69**(1): p. 459.
214. Sullivan, J.L., S.O. Saied, and I. Bertoti, *Effect of ion and neutral sputtering on single crystal TiO2.* Vacuum, 1991. **42**(18): p. 1203-1208.

215. Gao, S., et al., *Forming-free and self-rectifying resistive switching of the simple Pt/TaO$_x$/n-Si structure for access device-free high-density memory application.* Nanoscale, 2015. **7**(14): p. 6031-8.
216. Choi, S., et al., *Retention failure analysis of metal-oxide based resistive memory.* Appl. Phys. Lett., 2014. **105**(11): p. 113510.
217. Nakamura, R., et al., *Diffusion of oxygen in amorphous Al2O3, Ta2O5, and Nb2O5.* J. Appl. Phys., 2014. **116**(3): p. 033504.
218. Phan, B.T., et al., *Hopping and trap controlled conduction in Cr-doped SrTiO$_3$ thin films.* Solid State Electron., 2012. **75**: p. 43-47.
219. Lee, E., et al., *Resistance state-dependent barrier inhomogeneity and transport mechanisms in resistive-switching Pt/SrTiO$_3$ junctions.* Appl. Phys. Lett., 2011. **98**(13): p. 132905.
220. Kim, H., et al., *Inhomogeneous barrier and hysteretic transport properties of Pt/SrTiO$_3$ junctions.* J. Phys. D: Appl. Phys., 2009. **42**(5): p. 055306.
221. Hill, D.M., H.M. Meyer, and J.H. Weaver, *Y, Ba, Cu, and Ti interface reactions with SrTiO3(100) surfaces.* J. Appl. Phys., 1989. **65**(12): p. 4943-4950.
222. Cooper, D., et al., *Anomalous Resistance Hysteresis in Oxide ReRAM: Oxygen Evolution and Reincorporation Revealed by In Situ TEM.* Adv. Mater., 2017. **29**(23): p. 17002121-8.
223. Du, H., et al., *Atomic structure and chemistry of dislocation cores at low-angle tilt grain boundary in SrTiO$_3$ bicrystals.* Acta Mater., 2015. **89**: p. 344-351.
224. Rho, J., et al., *Observation of room temperature photoluminescence in proton irradiated SrTiO$_3$ single crystal.* J. Lumin., 2010. **130**(10): p. 1784-1786.
225. Bi, G.-Q. and H.-X. Wang, *Temporal asymmetry in spike timing-dependent synaptic plasticity.* Physiol. Behav. , 2002. **77**(4): p. 551-555.
226. Wang, H.-X., et al., *Coactivation and timing-dependent integration of synaptic potentiation and depression.* Nat. Neurosci., 2005. **8**(2): p. 187-193.
227. Chu, M., et al., *Neuromorphic Hardware System for Visual Pattern Recognition With Memristor Array and CMOS Neuron.* IEEE Trans. Ind. Electron., 2015. **62**(4): p. 2410-2419.
228. Xinyu, W., V. Saxena, and Z. Kehan. *A CMOS spiking neuron for dense memristor-synapse connectivity for brain-inspired computing*. in *2015 International Joint Conference on Neural Networks (IJCNN)*. 2015.
229. Friedmann, S., et al., *Demonstrating Hybrid Learning in a Flexible Neuromorphic Hardware System.* IEEE Trans. Biomed. Circuits Syst., 2017. **11**(1): p. 128-142.
230. Blagojević, M., et al. *A fast, flexible, positive and negative adaptive body-bias generator in 28nm FDSOI*. in *2016 IEEE Symposium on VLSI Circuits Digest of Technical Papers*. 2016. Widerkehr and Associates
231. Meijer, M. and J.P.d. Gyvez, *Body-Bias-Driven Design Strategy for Area- and Performance-Efficient CMOS Circuits.* IEEE Trans. VLSI Syst., 2012. **20**(1): p. 42-51.
232. Meijer, M., et al. *A forward body bias generator for digital CMOS circuits with supply voltage scaling*. in *Proceedings of 2010 IEEE International Symposium on Circuits and Systems*. 2010.

Appendices

Appendix A: Supporting Information for Chapter 3

Figure A1 shows the core level binding energy spectra of Ti 2*p* and Nb 3*d* in virgin Nb:*a*-STO_x oxide layer. This illustrates the partially reduced titanium sub-oxide network and the substitutional doping of niobium species (at a 5+ ionization state) in the oxygen-deficient oxide structure. The relative concentration of Ti^{3+}/Ti^{4+} species in Nb:*a*-STO_x is only slightly lower than that of pristine *a*-STO_x (34% and 40%, respectively) as estimated from the integrated peak area for respective fits. This slight difference falls within the margin of error for background correction and peak fitting procedures. Therefore, it appears that low concentrations of donor species do not significantly alter the sub-oxide species within the amorphous phase.

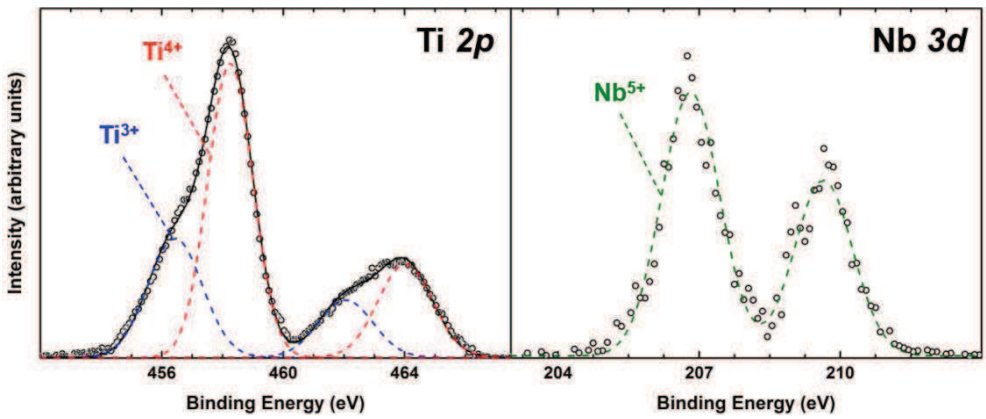

Figure A1 Core-level binding energy spectra of Ti 2*p* and Nb 3*d* in as-grown Nb:*a*-STO_x thin films.

Figure A2 depicts TEM micrographs of an as-grown MIM device obtained from a FIB-cut cross-section. No evidence of crystalline regions was found in the as-grown sample. At the interface, the redox reaction between the metal and oxide sides results in a partially reduced/oxidized region that is highlighted as a uniformly bright region (the area between the dashed lines in figure A2b).

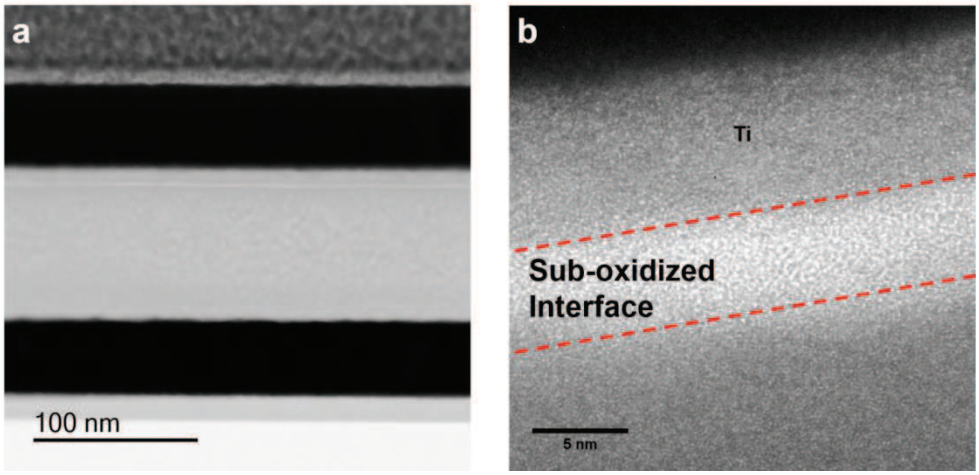

Figure A2 (a) TEM micrograph of a representative random area in virgin Nb:*a*-STO_x device corss-section. (b) HR-TEM micrograph of the interfacial Ti/Nb:*a*-STO_x region. Dashed lines indicate the partially reduced interfacial region.

Figure A3 depicts a wide-view and a magnified TEM micrograph of represntative area in switching MIM device cross-section. The regions with distinctly contrast variations are expected to show significant structural and compositional variations and are targeted form HR-TEM and STEM-EELS studies.

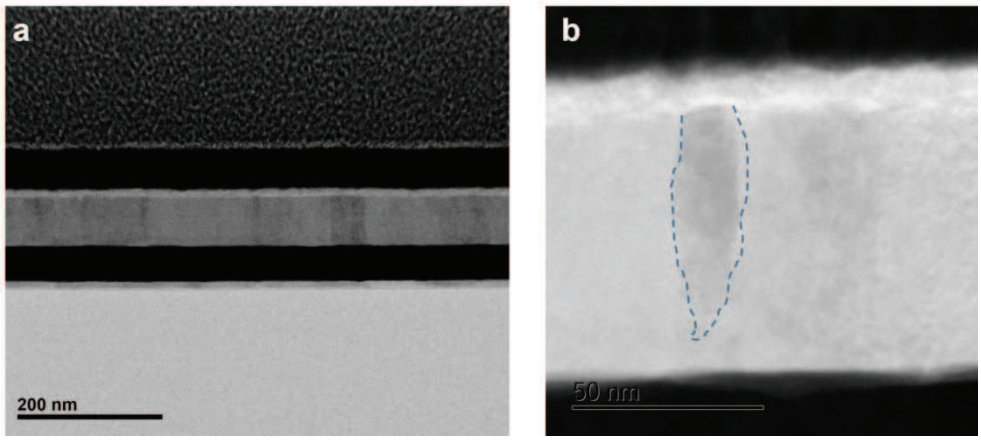

Figure A3 (a) Low and (b) high magnification TEM micrographs of a representative area in switching Nb:*a*-STO_x device cross-section. The areas with distinct contrast variations are targeted for detailed studies.

Appendix B: Supporting Information for Chapter 4

B1. Characterization of functional Cr:*a*-STO_x thin films

Figure B1 shows the core-level XPS spectra of O 1*s* and Sr 3*d* in the sputtered Cr:*a*-STO_x thin films. The O 1*s* spectra (Figure B1a) can be de-convoluted into two components centered at 529.5 eV and 531.24 eV which can be associated with O^{2-} ions and C-O bond on the surface.[B1,B2] The core-level spectra of Sr 3*d* (Figure B1b) is de-convoluted into a single component indexed to Sr^{2+} with Sr $3d_{5/2}$ and Sr $3d_{3/2}$ peaks at 132.89 eV and 134.66 eV binding energies, respectively.[B1-3]

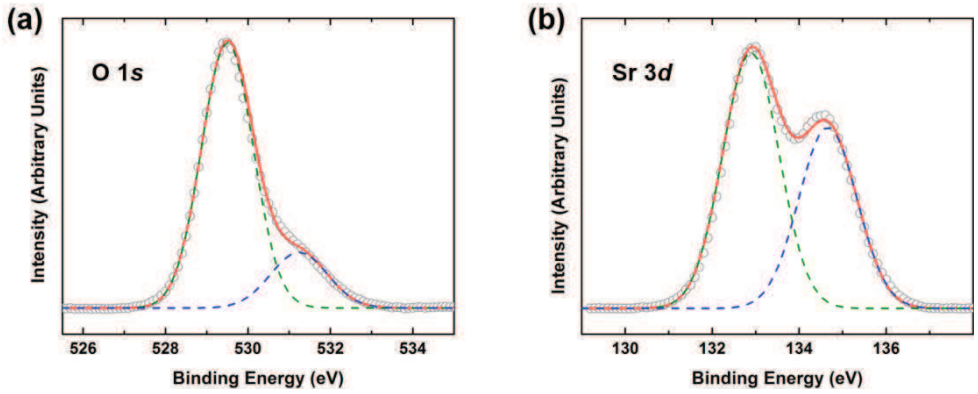

Figure B1 The XPS spectra from Cr:*a*-STO_x thin films. The core-level spectra of (a) O 1*s* and (b) Sr 3*d* of the sputtered thin films.

Figure B2 shows the core-level XPS spectra of principal elements acquired from the un-doped *a*-STO_x thin films sputtered in a pure Ar environment. The Ti 2*p* spectra (Figure B2a) are fitted with two distinct components at binding energies of 458.4 eV and 456.2 eV indexed to the Ti^{4+} and Ti^{3+} oxidation states, respectively.[B4] The core-level spectra of Sr 3*d* (Figure B2b) are de-convoluted into the Sr^{2+} oxidation state at binding energies 132.98 eV and 134.72 eV for Sr $3d_{5/2}$ and Sr $3d_{3/2}$, respectively.[S1,S2] Furthermore, the core-level spectra of O 1s (Figure B2c) are de-convoluted into two components at 529.5 eV and 531.4 eV binding energies indexed to the O^{2-} oxidation state and C-O bonds on the oxide surface, respectively.[B1,B2]

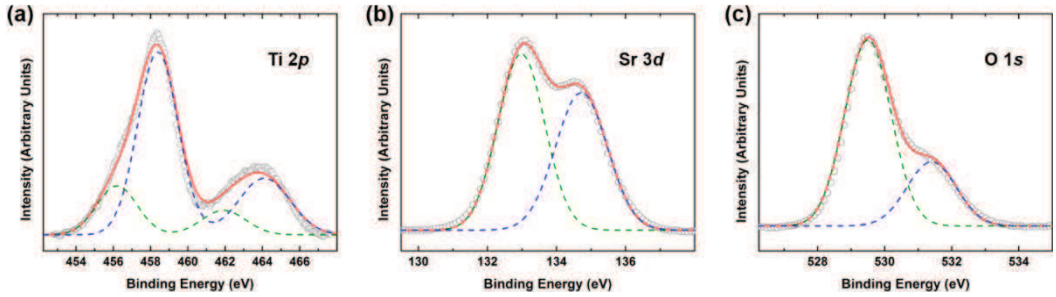

Figure B2 The XPS spectra of principal elements from sputtered undoped oxygen deficient *a*-STO_x thin films. The core-level spectra of (a) Ti 2*p*, (b) Sr 3*d* and (c) O 1*s*.

B2. Resistive switching characteristic of MIM devices

Figure B3 shows the representative electroforming sweeps to induce multifunctional resistive switching behaviors in our Cr:*a*-STO_x MIM devices.

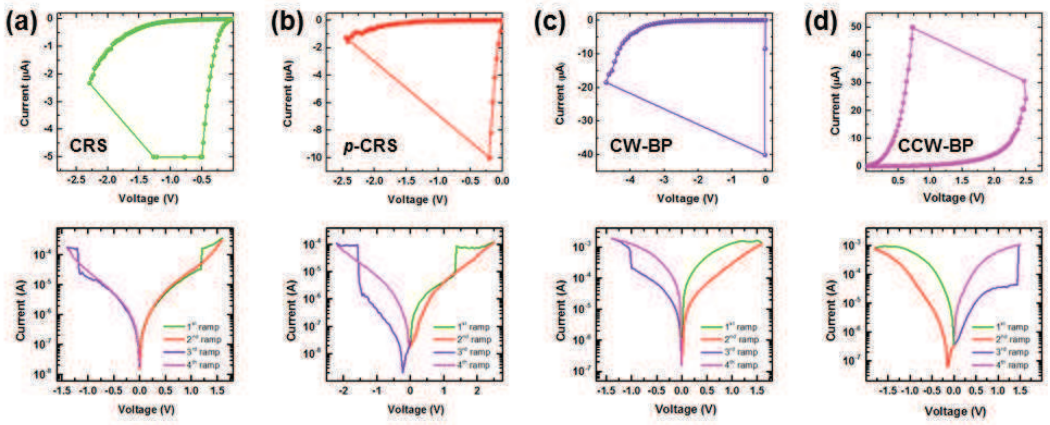

Figure B3 Current compliance controlled electroforming step and induced resistive switching behaviors. The representative electroforming sweeps to induce (a) complementary resistive switching behavior where current compliance is set to 5 μA, (b) *peculiar*-complementary resistive switching where current compliance is set to 10 μA, (c) clockwise bipolar resistive switching with current compliance fixed at 40 μA and (d) counter-clockwise bipolar resistive switching with current compliance at 50 μA. The colored voltage ramps represent the sequence of applied voltage sweeps during the subsequent switching cycles of the corresponding resistive switching behavior. The current compliance is set to $>5\times10^{-4}$ A during the switching cycles.

The effect of current compliance during the electroforming process is studied on at least 115 Cr:*a*-STO_x based MIM devices. **Figure B4** shows that the current compliances in the range 1-5 µA, 10-15 µA and 40-100 µA induce CRS, *p*-CRS and bipolar resistive switching (BRS) behaviors, respectively.

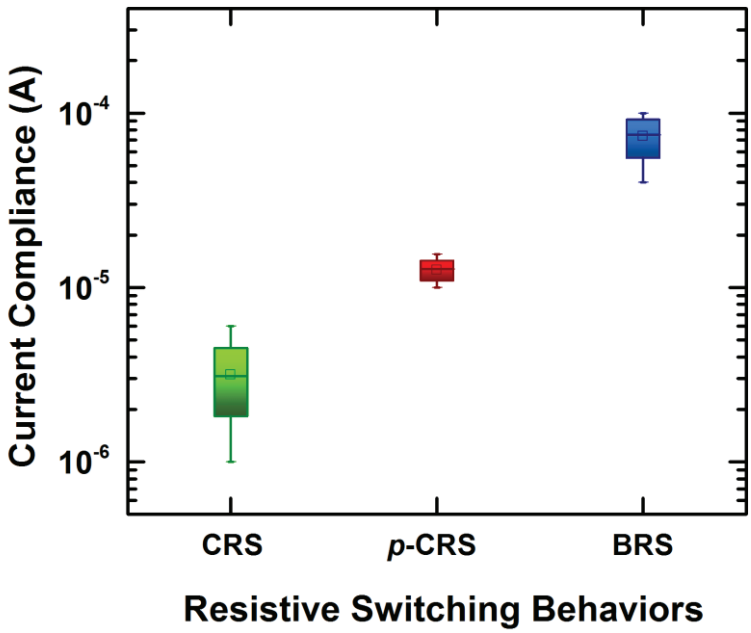

Figure B4 Influence of the current compliance on the resistive switching behaviors. Statistical distribution of the current compliance during electroforming process based on the data acquired from 115 different MIM devices.

In order to evaluate the reliability of the switching behaviors, the retention and endurance characteristics are measured for several devices in their corresponding switching behaviors. For each switchingbehavior, at least 15 different devices are electroformed to induce either *p*-CRS, CW-BP or CCW-BP switching behavior before they are subjected to the retention and endurance measurements. **Figure B5** shows that our Cr:*a*-STO_x MIM devices exhibit reproducible retention and cyclic endurance characteristics in their corresponding resistive switching behaviors without the loss of memory window.

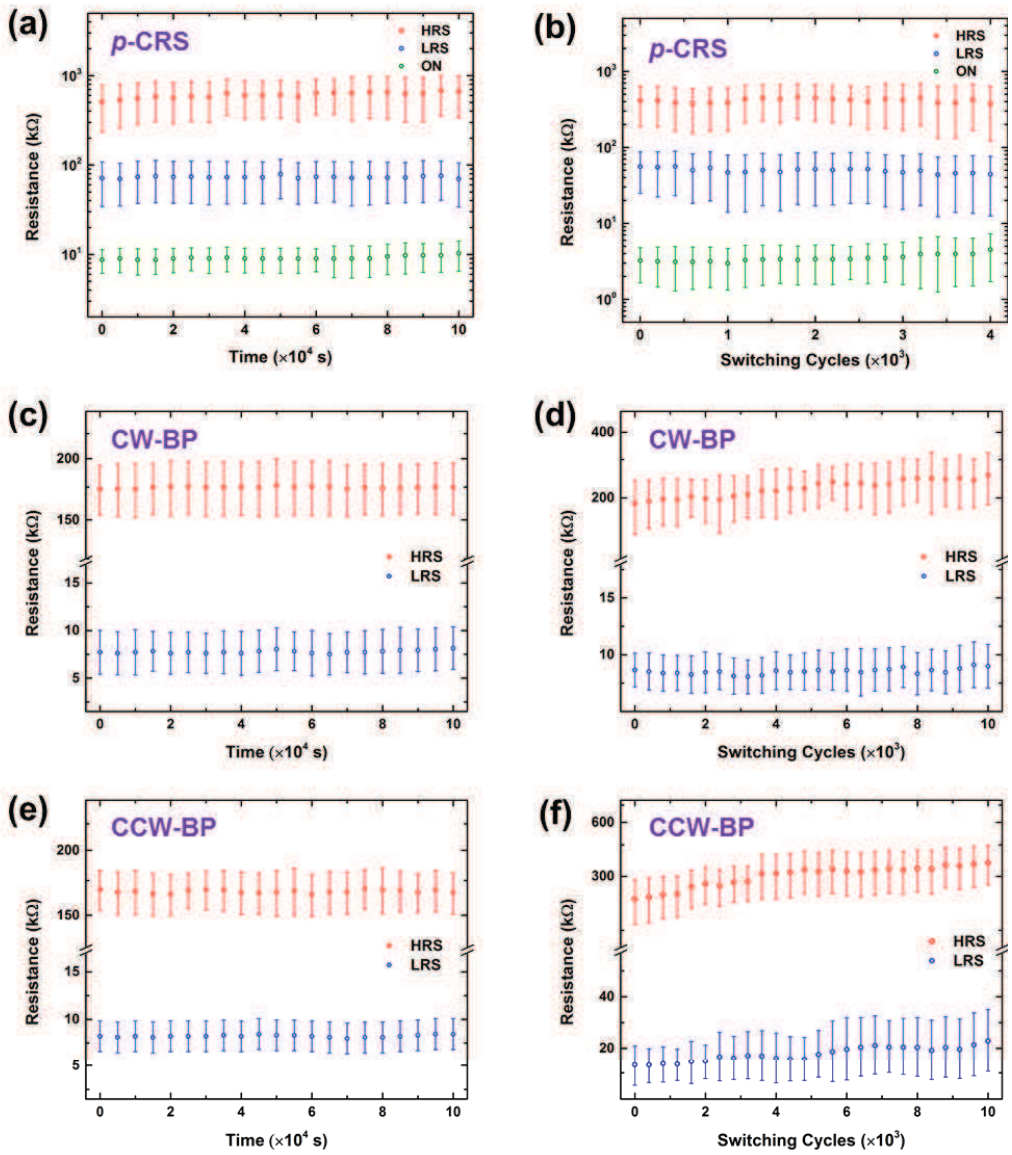

Figure B5 Electrical performance of the resistive switching behaviors. The retention and endurance characteristics of (a, b) the *p*-CRS, (c, d) the CW-BP and (e, f) CCW-BP switching behaviors, respectively, are measured and averaged for at least 15 different devices, for each switching behavior. The bars indicate the standard deviation.

Symmetric Pt (35 nm)/Cr:*a*-STO_x (25 nm)/Pt (7 nm) MIM devices are prepared by following identical fabrication conditions as the asymmetric MIM devices. **Figure B6** shows the *I*–*V* characteristic of a symmetric MIM device.

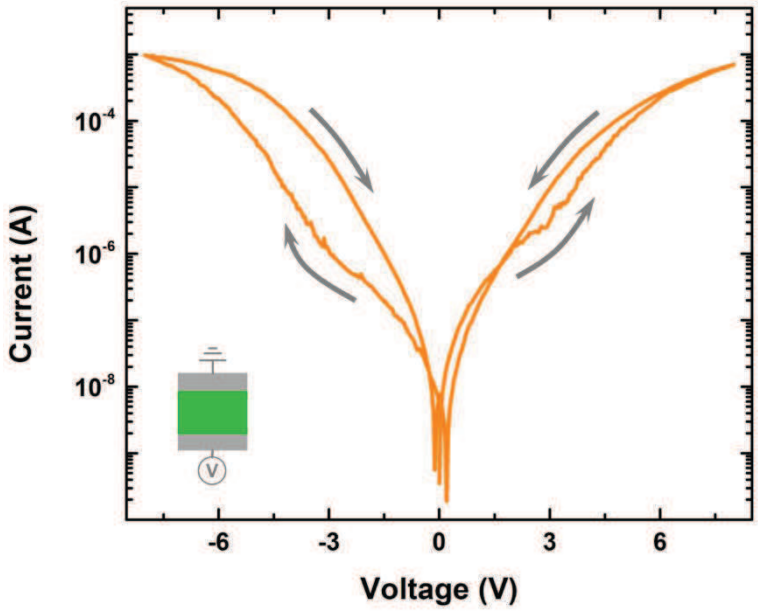

Figure B6 Electrical characteristics of the symmetric MIM devices. *I–V* cyclic sweep of the symmetric MIM device while biasing from the bottom Pt electrode. Inset shows the biasing scheme during cyclic sweeps.

B3. Cross-sectional analyses of Cr:*a*-STO_x MIM devices

Transmission electron microscope (TEM) and electron energy loss spectroscopy (EELS) techniques are used to analyze the morphology and composition of the Cr:*a*-STO_x MIM devices. In order to ascertain the effect of applied bias (during electroforming and resistive switching) on the metal/oxide interfaces and within the functional oxide, the cross-sectional TEM samples are prepared from separate MIM devices subjected to different bias conditions namely; pristine, electroformed and switching devices.

Figure B7 shows the cross-sectional TEM analyses of a pristine Cr:*a*-STO_x MIM device. Figure B7a shows a TEM micrograph of the MIM structure where the Cr:*a*-STO_x oxide film is sandwiched between the top Pt/Ti and bottom Pt electrodes. The selected-area electron diffraction (SAED) pattern collected from the MIM cross-section shows a diffused ring (Figure B7b), indicative of an amorphous structure. The amorphous structure of the Cr:*a*-STO_x oxide film is also confirmed by the high-resolution TEM (HRTEM) micrograph, shown in Figure B7c. To assess the electronic composition and the relative distribution of oxygen content across the pristine MIM device, the EELS area map is collected by considering the O–*K* edge intensities (Figure B7d). The presence of low oxygen content in the Cr:*a*-STO_x oxide layer

indicates its oxygen deficient stoichiometry which is consistent with our XPS analyses. The EELS Ti–$L_{2,3}$ and O–*K* edge profiles are also obtained from a line-scan across the MIM structure (Figure B7e). Broad Ti–L_3 and Ti–L_2 peaks at the top Ti/Cr:*a*-STO_x interface indicate the presence of mixed Ti^{2+} and Ti^{3+} oxidation states,[S5] which suggests the partial oxidation of top Ti layer (also observed in the EELS area map, Figure B7d). In the functional oxide layer, a weak splitting of the t_{2g} and e_g peaks in a few Ti–$L_{2,3}$ edge profiles indicate Ti^{4+} oxidation state. However, O–*K* edge profiles are weak and noisy which makes difficult to clearly distinguish the fine structures and cannot be used to accurately identify the Ti valence.

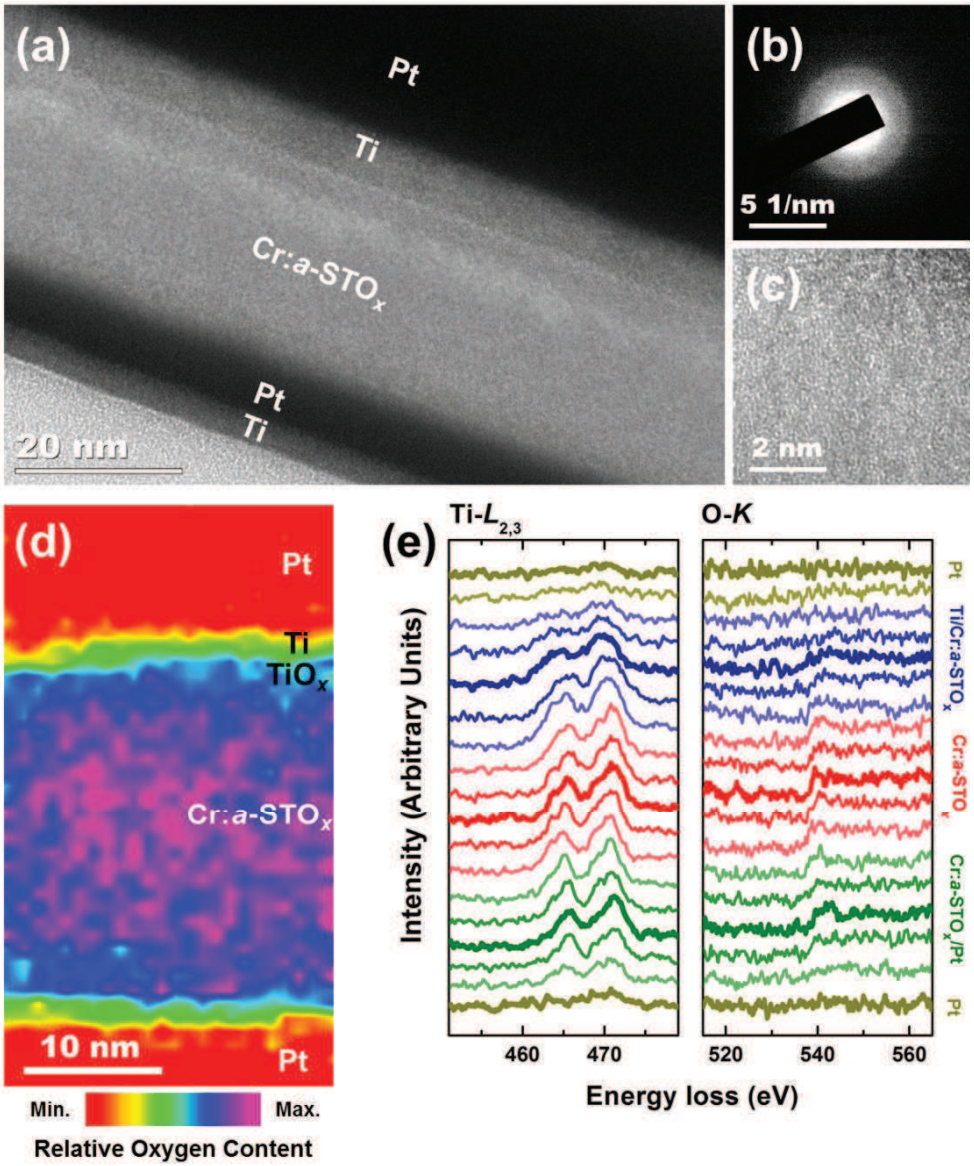

Figure B7 Microstructure and electronic structure of the pristine Cr:a-STO_x devices. (a) TEM micrograph of a pristine MIM device. (b) Selected area electron diffraction pattern collected from the MIM cross-section. (c) High resolution TEM micrograph of the Cr:*a*-

STO_x oxide film. (d) The EELS O–*K* edge area map and (e) the EELS Ti–$L_{2,3}$ and O–*K* edge profiles along a line scan across the MIM device.

Figure B8a shows the cross sectional TEM micrograph of a Cr:*a*-STO_x MIM device electroformed to exhibiting BP resistive switching behavior. The highlighted region of interest (ROI, enclosed in a box) shows the isolated incomplete filaments along the bottom interface. The fast Fourier transform (FFT, Figure B8b) taken from the ROI shows the diffraction spots. The diffraction spots indicated with arrows can be indexed to the cubic phase of STO and are masked to perform an inverse FFT (iFFT), as shown in Figure B8c. Several diffraction spots are used to ensure the iFFT show the distribution of crystals with differing orientations.

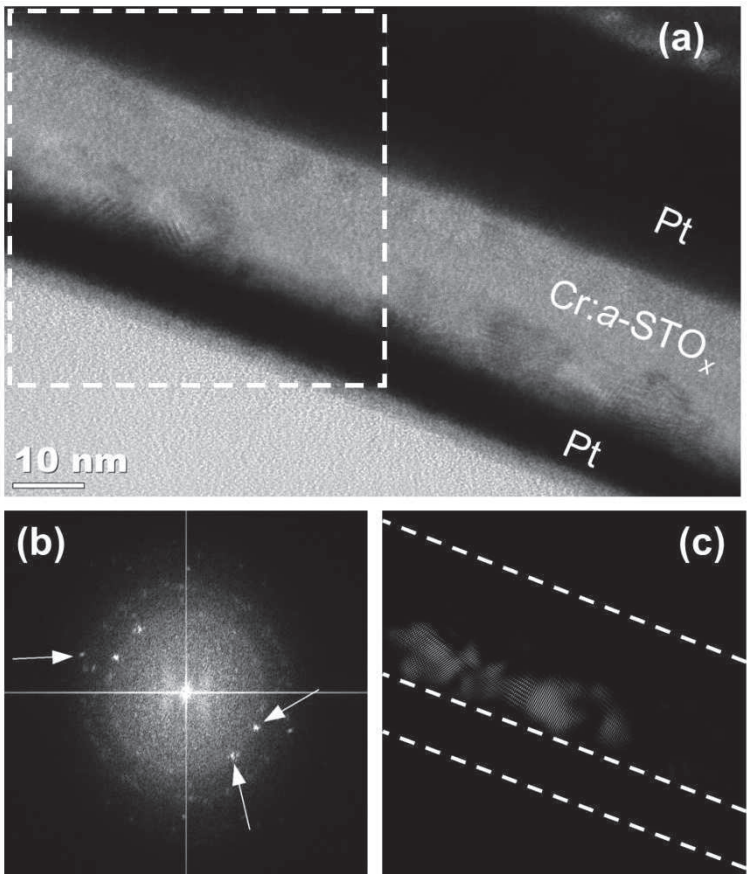

Figure B8 Morphological analyses of the Cr:*a*-STO_x MIM devices electroformed to exhibit CW-BP resistive switching behavior. (a) TEM micrograph of the MIM device subjected to electroforming step to exhibit CW-BP switching behavior. The box encloses the ROI. (b) The FFT diffraction patterns generated from the ROI enclosed in

(a). (c) The iFFT obtained from a diffraction spot in (b) highlight the crystalline region along the bottom electrode.

Figure B9a shows the cross sectional HR-TEM micrograph of a Cr:*a*-STO_x MIM device in its HRS, exhibiting CW-BP resistive switching characteristics. The ROI shows the localized crystalline region in the active Cr:*a*-STO_x layer, extending from the bottom Pt electrode. The FFT diffraction pattern of the ROI (Figure B9b) indicates the presence of different crystalline phases of STO. The diffraction spot of the highest intensity (marked as spot 1 in Figure B9b) and other weaker diffraction spots can be assigned to the cubic perovskite STO phase. However, the encircled diffraction spots could not be assigned to the cubic perovskite STO phase, indicating the presence of other secondary phases. The spot 1 (with the *d*-spacing of 0.28 nm) is used to generate the iFFT (Figure B9c) highlighting the presence of [011] cubic STO phase in the selected ROI.

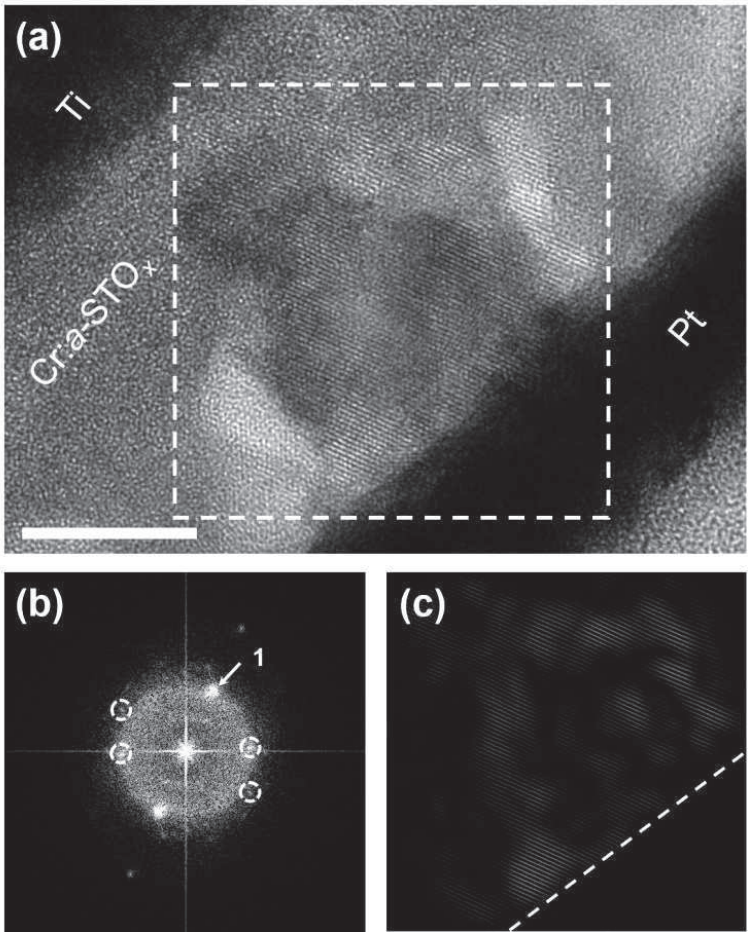

Figure B9 Morphological analyses of the Cr:*a*-STO_x MIM devices in HRS and exhibiting CW-BP resistive switching behavior. (a) TEM micrograph of the MIM

device subjected to at least 100 switching cycles and set to HRS prior to the lamella preparation. ROI is enclosed in the box. Scale bars 5 nm. (b) The FFT diffraction patterns generated from the ROI enclosed in (a). (c) The iFFT obtained from spot 1 in (b) highlight the crystalline region.

Figure B10 shows the cross-sectional HR-TEM micrograph of the top Ti/Cr:*a*-STO_x interface of a MIM device subjected to electroforming. In order to assess the morphological changes in the top Ti layer, two ROIs are selected along its length at two different locations (Figure B10a). The FFT diffraction patterns generated for each location (Figure B10b and 10c) reveal the polycrystalline structure of the top Ti layer. The high intensity diffraction patterns with the *d*-spacing ranging from 0.24 nm to 0.26 nm can be indexed to the different planes of the rhombohedral Ti_2O_3. This suggests that under the influence of applied electroforming bias, the as-deposited amorphous Ti layer (observed in TEM analysis from pristine MIM devices shown in Figure B7a) has changed its micro-structure to polycrystalline along the length of top Pt electrode (acting as an anode). Furthermore, the diffusion of oxygen ions from the functional Cr:*a*-STO_x layer causes the oxidation of Ti to a suboxide such as Ti_2O_3.

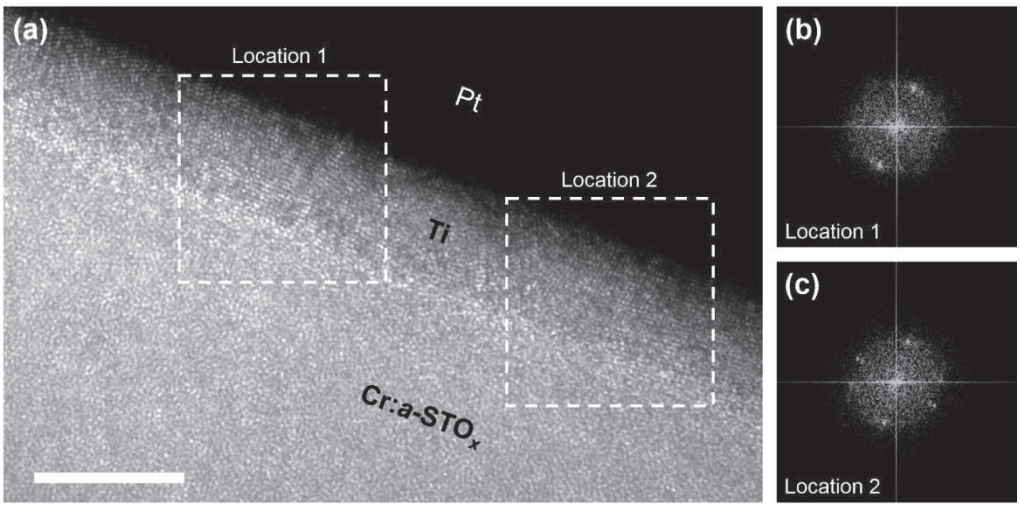

Figure B10 Microstructure of electroformed MIM devices**.** (a) TEM micrograph of top Pt/Ti/Cr:*a*-STO_x interface. Two ROIs are selected at Location 1 and Location 2, enclosed in boxes. Scale bar denotes 10 nm. (b) and (c) are the FFT diffraction patterns generated from Location 1 and Location 2, respectively, in (a).

Figure B11 shows the EELS O–*K* edge area map of the locally crystalline ROI from the MIM device exhibiting CW-BP resistive switching behavior (presented in Figure B9). The representative MIM device was set to HRS prior to TEM sample preparation. Relatively low oxygen content at the bottom Pt electrode indicates a ruptured filamentary path and accumulation of the V_os at anode in HRS. Presence of varying oxygen content at the vicinity of top Pt electrode shows the oxidation of Ti layer to a sub-stoichiometric Ti_2O_3, as indexed in the FFT analysis.

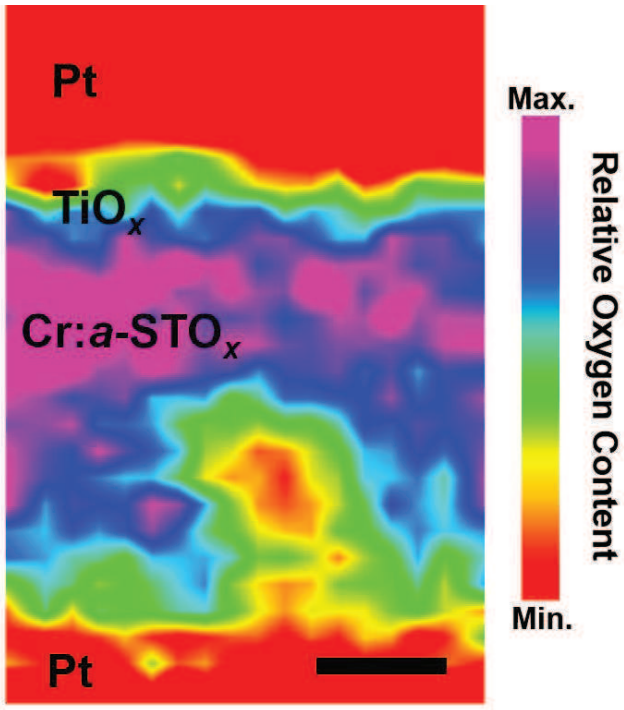

Figure B11 Relative distribution of oxygen in the Cr:*a*-STO_x MIM devices exhibiting CW-BP resistive switching behavior. The EELS O–*K* edge area map of the conductive filamentary path in HRS. Scale bar represents 20 nm.

Reference

[B1] D. Ehre, H. Cohen, V. Lyahovitskaya, I. Lubomirsky, *Phys. Rev. B* **2008**, *77*, 184106.

[B2] P. V. Nagarkar, P. C. Searson, F. D. Gealy, *J. Appl. Phys.* **1991**, *69*, 459.

[B3] H. Yu, S. Ouyang, S. Yan, Z. Li, T. Yu, Z. Zou, *J. Mater. Chem.* **2011**, *21*, 11347.

[B4] H. L. Cai, X. S. Wu, J. Gao, *Chem. Phys. Lett.* **2009**, *467*, 313.

[B5] Y. Li, Q. Wang, M. An, K. Li, N. Wehbe, Q. Zhang, S. Dong, T. Wu, *Adv. Mater. Interf.* **2016**, *3*, 1600201.

Appendix C: Supporting Information for Chapter 5

C1. Area dependent resistive switching characteristics

In transition metal oxides, the bipolar resistive switching behaviour is usually attributed to the formation and rupture of localized filamentary pathways due to redox processes.[C1,C2] Under a filamentary switching mechanism, the lateral dimensions of the memory cell are not expected to influence the resistive switching properties. **Figure C1** shows the correlation between HRS/LRS read currents and the area of our *t*-ReRAM cells. Unlike interfacial resistive switching, where the resistance–area product is independent of cell size,[C3] our *t*-ReRAMs show an increase in the product with increasing cell size. This further indicates that the switching mechanism in both Device BL15 (Fig. C1a) and Device BL5 (Fig. C1b) is of a filamentary nature.

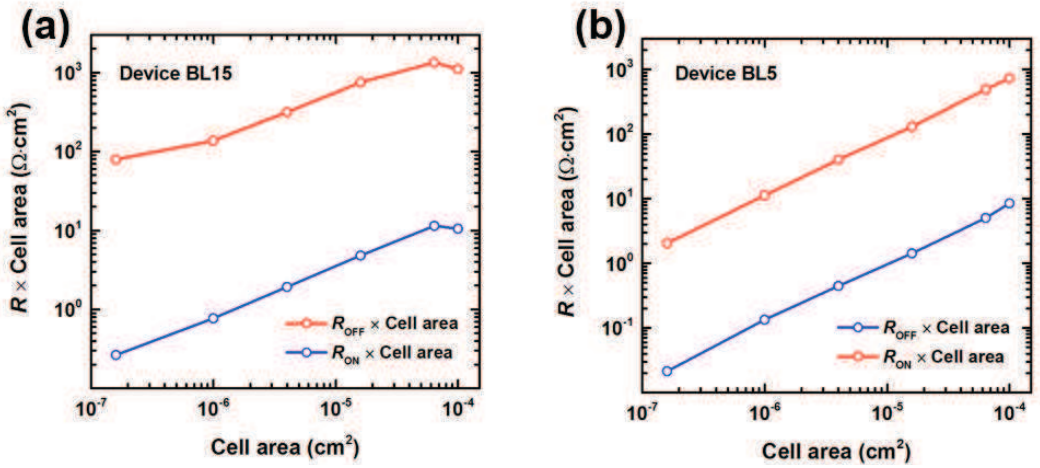

Figure C1 The resistance–area product of Device BL15 (a) and Device BL5 (b) in HRS and LRS. The resistances are measured for varying cell sizes at a V_{READ} of 0.5 V.

C2. Stoichiometric analysis of ITO thin films

The XPS analysis was carried out to characterize the composition and identify the chemical states of the principal elements in sputtered ITO (50 nm) thin films on glass. Curve-fitting of the core level spectra (O 1*s*, Sn 3$d_{5/2}$ and In 3$d_{5/2}$) for two types of ITO thin films, namely – as-grown and post-deposition annealed at 400 ˚C, is shown in **Figure C2**.

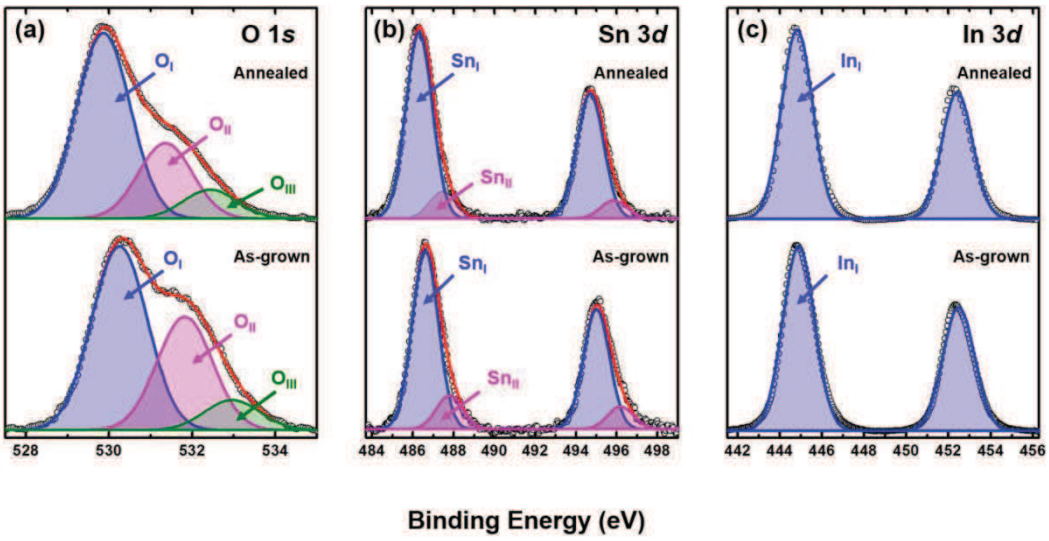

Figure C2 High resolution XPS spectra corresponding to (a) O 1*s* (b) Sn 3*d* and (c) In 3*d* for the as-grown and post-deposition annealed ITO (50 nm) thin films.

The characteristic peaks positions are within the corresponding rage and are comparable to those reported in the literature.[C4-7] All sub-peaks of principal elements have been labelled to distinguish among them and their positions are listed in Table C1. The O 1*s* spectra have been fitted with three peaks centered at 530.3 eV (O_I), 531.8 eV (O_{II}), 533.0 eV (O_{III}) for as-grown, and 529.9 eV (O_I), 531.4 eV (O_{II}) and 532.4 eV (O_{III}) for the post-deposition annealed sample. It is believed that the room temperature sputtering of ITO in a pure Ar environment results in oxygen deficient thin films, originating O_I and O_{II} peaks in the XPS spectra due to the formation of two types of O^{2-} ions.[C5] Whereas O_{III} at higher binding energies (533.0 eV and 532.4 eV for as-grown and annealed samples, respectively) is associated with $In(OH)_x$ present on the surface.[C4,C7] The presence of oxygen deficient regions such as oxygen vacancies (V_o) and Sn centers, in ITO thin film act as charge trapping sites, making In 3*d* peaks insensitive to the concentration V_o and Sn species.[C7] In the literature, it is suggested that the O_{II}/O_I ratio can be used to estimate the oxygen deficiency in the ITO thin films.[C5] The calculated O_{II}/O_I ratios (listed in **Table C1**) for our sputtered ITO thin films show that as-grown ITO thin films are more oxygen deficient than the post-deposition annealed thin films.

	Labels	Peak positions (eV)	
		As-grown	Annealed
O 1*s*	O_I	530.3	529.9
	O_{II}	531.8	531.4
	O_{III}	533.0	532.4
Sn $3d_{5/2}$	Sn_I	486.9	486.3
	Sn_{II}	487.6	487.5
In $3d_{5/2}$	In_I	444.9	444.8
	O_{II}/O_I	0.62	0.41

Table C1 Peak positions of the resolved core level XPS spectra from the principal elements in as-grown and post-deposition annealed ITO thin films.

C3 Optical transmission characterization of ITO thin films

Optical transmission characteristics of both as-grown and post-deposition annealed ITO thin films (50 nm), within the optical range of 300-800 nm, are shown in **Figure C3**. The average transmission increased after post-deposition annealing at 400 ˚C in air which is consistent with the literature.[C4]

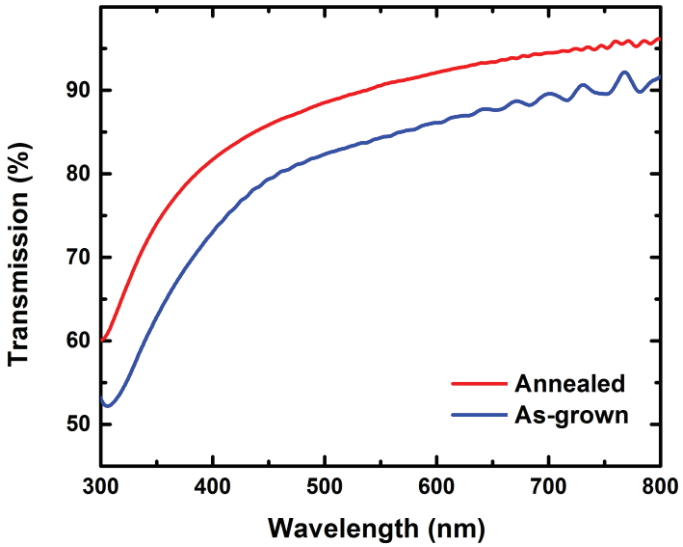

Figure C3 Optical transmission characteristics of the ITO (~50 nm) thin films sputtered at room temperature on glass substrates.

C4 Electrical characterization of single layer and bilayer *t*-ReRAM cells with symmetric interfaces

The *I–V* characteristics of a single layer (ITO/*a*-STO_x (35 nm)/ITO) and bilayer (ITO/*a*-STO_x (10 nm)/*a*-STO_y (15 nm)/ITO) are shown in **Figure C4a** and Figure C4b, respectively.

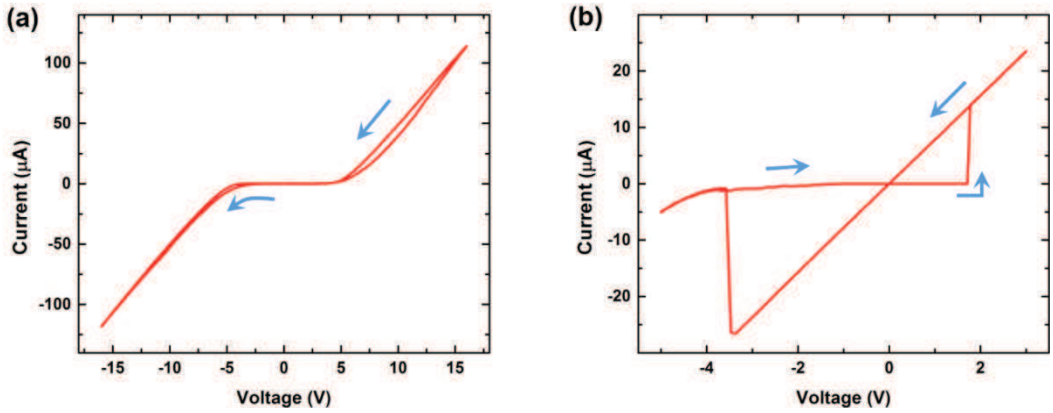

Figure C4 Electrical characterization of transparent devices with symmetric interfaces. (a) *I–V* characteristics of single layer ITO/*a*-STO_x/ITO cell. (b) *I–V* characteristics of bilayer ITO/*a*-STO_x/STO_y/ITO cell.

C5. Optical characterization

UV-Vis transmission and reflectance spectra of sputtered functional bilayer (*a*-STO_x/*a*-STO_y) oxide stack, bottom (ITO) and top (ITO/Ti) electrodes of our devices are shown in **Figure C5a** and C5b, respectively. The bottom ITO electrodes are post-deposition annealed (at 400 ˚C in air) to improve the transparency of *t*-ReRAM cells, instead of annealing top ITO/Ti electrode which may permanently diffuse the interfaces at high temperature and deteriorate the resistive switching performance of the devices. **Figure C6** shows the reflectance spectra of both Device BL5 and Device BL15. The reflectance spectra are collected from device (ITO/Ti/*a*-STO_x/*a*-STO_y/ITO) region.

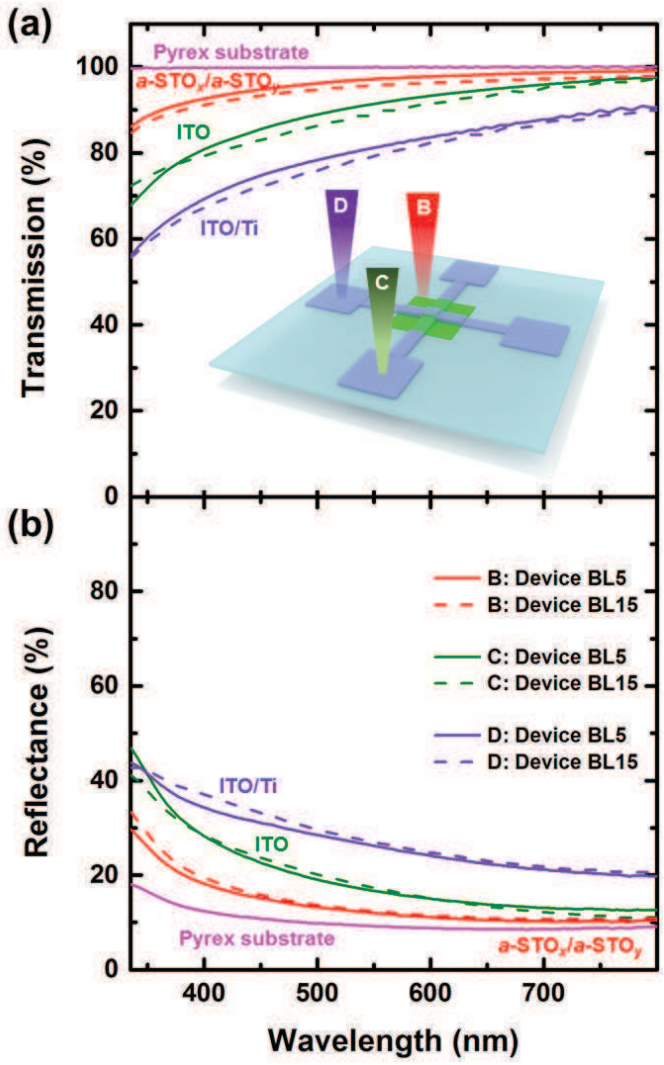

Figure C5 Optical characteristics of the sputtered oxides. (a) UV-Vis transmission and (b) reflectance spectra of the bilayer *a*-STO_x/*a*-STO_y stack, bottom ITO and top ITO/Ti electrodes for Device BL5 and Device BL15. Inset shows a schematic of the regions on the cross-point cells used for the collection of transmission spectra for both devices and are highlighted by markers "B", "C" and "D" for bottom ITO electrode, *a*-STO_x/*a*-STO_y stack and top ITO/Ti electrode, respectively.

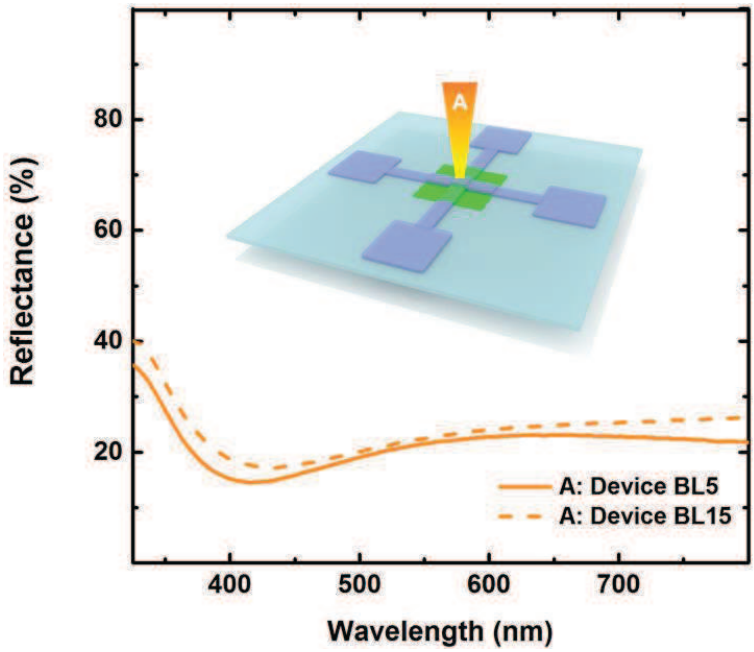

Figure C6 UV-Vis reflectance spectra of Device BL5 and Device BL15 in 325-800 nm optical range. The spectra are collected from the device area highlighted by a marker "A" on the inset schematic of a cross-point device.

C6. XPS analysis of functional *a*-STO oxides

Figure C7 shows the core-level binding energy spectra of oxygen (O 1*s*) and strontium (Sr 3*d*) in *a*-STO_x and *a*-STO_y oxides sputtered in a reducing (0% oxygen) and an oxidizing (5% oxygen) environment, respectively. In both oxides, O 1*s* spectra (Figure C7a) can be fitted with two components with peak positions at 529.5 eV (±0.1 eV) and 531.3 eV (±0.1 eV), corresponding to O^{2-} ions in *a*-STO oxide[C8] and C–O bond[C8-10] formed due to adsorption of adventitious carbon onto the surface, respectively.

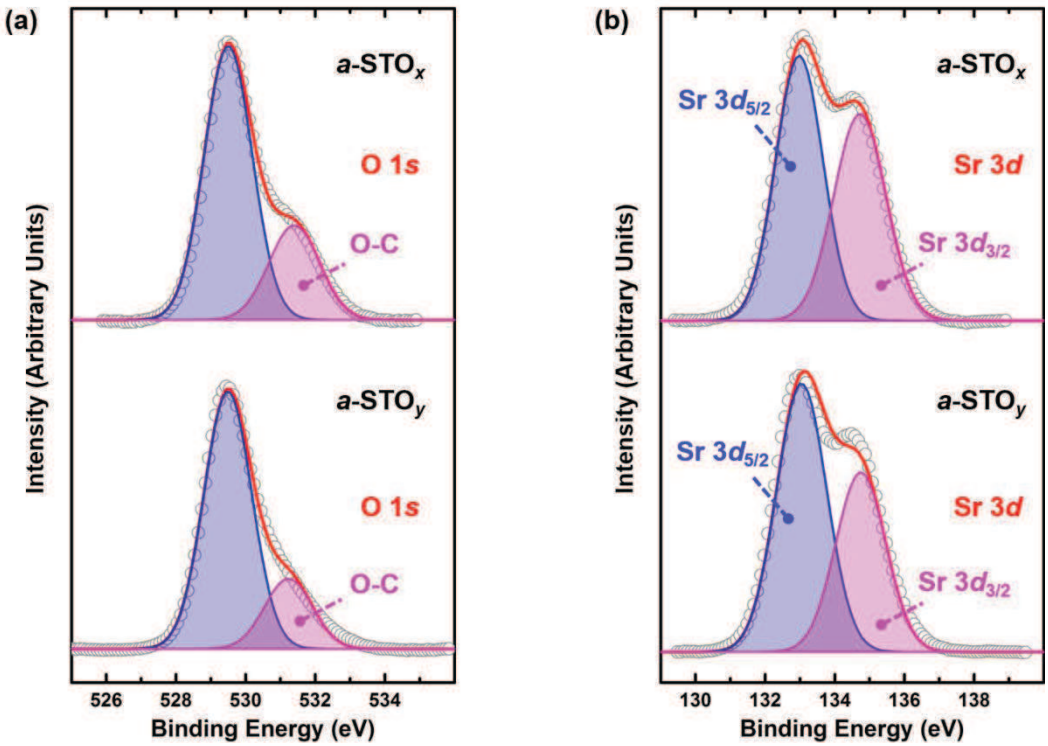

Figure C7 Core-level XPS spectra of (a) O 1*s* and (b) Sr 3*d* for as-grown *a*-STO_x and *a*-STO_y oxides.

Furthermore, the core-level spectra of Sr 3*d* (Figure C7b) could be fitted into a single component with no significient shift observed in chemical states. The binding energies for Sr $3d_{5/2}$ at 132.9 eV (±0.1 eV) and for Sr $3d_{3/2}$ at 134.7 eV (±0.1 eV) for both oxides, are attributed to Sr^{2+} species in *a*-STO.[C8,C10]

C7. Electroforming of *t*-ReRAMs

Figure C8 shows the electroforming sweeps of 10×10 μm^2 *t*-ReRAMs while biasing from the bottom ITO electrodes. The Device BL15 (Figure C8a) electroforms by applying -17.2 V and setting the current compliance at 100 µA. On the other hand, the Device BL5 (Figure C8b) electroforms by applying -14.5 V and the current compliance fixed at 5 µA. Comparatively higher electroforming current in the Device BL15 than the Device BL5 can be associated with the higher concentration of as-grown V_os in the Device BL15 owing to its thicker oxide stack. Under the influence of an electroforming voltage, the concentration of V_os further increases which results in the formation of conductive filamentary pathways and consequently an abrupt jump in current (limited by the current compliance at -100 µA) is observed at around -16.3 V (Figure C8a).

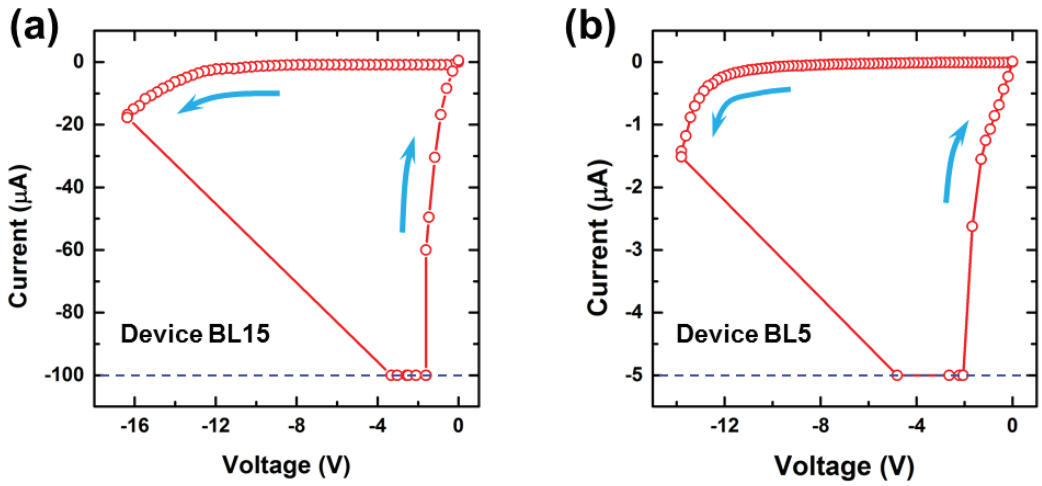

Figure C8 The electroforming *I–V* sweeps of 10×10 μm^2 *t*-ReRAMs. The electroforming sweep of (a) Device BL15 where current compliance is fixed at 100 μA and (b) Device BL5 where current compliance is fixed at 5 μA.

C8. X-ray diffraction spectra of ITO

The crystalline structure of as-deposited and post-deposition annealed ITO films (150 nm) on a glass substrate is investigated by X-ray diffraction (Bruker, D2 Phaser). In **Figure C9**, the diffractogram of annealed ITO (at 400 ˚C in ambient) shows a crystalline structure and can be indexed to cubic In_2O_3.[C11,C12]

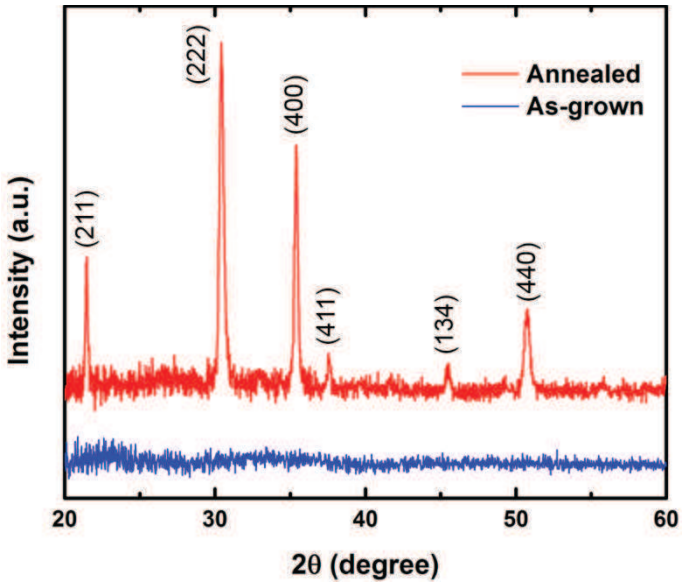

Figure C9 X-ray diffractograms of room temperature sputtered and post-deposition annealed ITO thin films on pyrex substrates.

C9. Electron energy loss spectroscopic analysis of *t*-ReRAM cells

Figure C10 shows the titanium $L_{2,3}$ absorption edge of a virgin and an electroformed *t*-ReRAM cell. The fine structure from the electroformed cell is relatively more defined and the presence of t_{2g} peak indicates the higher morphological order in *a*-STO than the virgin cell.[C13,C14]

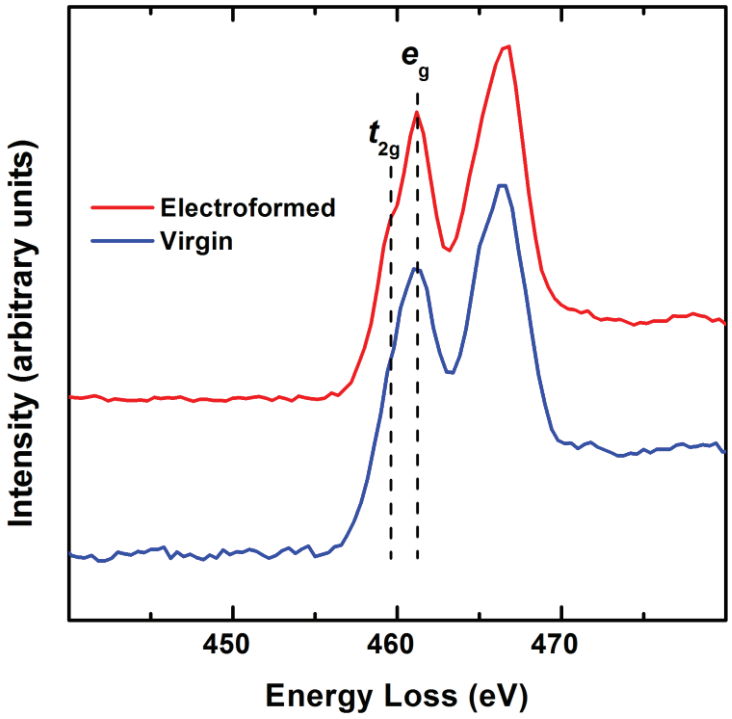

Figure C10 Electron energy loss spectra of the virgin and electroformed *t*-ReRAM cells for the titanium $L_{2,3}$ edge.

C10. Photoelectric characterization of *t*-ReRAM cells

The photoelectric response of *t*-ReRAM cells in HRS is measured under UV illumination (25±2 mW/cm^2) as a function of exposure frequency. **Figure C11** shows the photoelectric modulation in HRS of Device BL15 at 10 Hz of exposure frequency (Figure C11a) and Device BL5 at 5 Hz (Figure C11b) under read voltages of 0.25 V and 1 V, respectively.

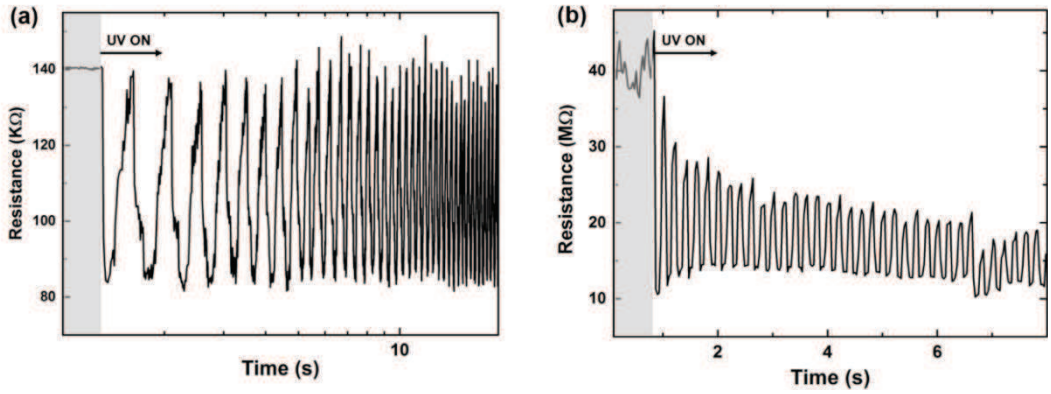

Figure C11 Photoelectric modulation in HRS of the *t*-ReRAM devices. (a) Photoelectric response of Device BL15 at 10 Hz of exposure frequency, measured under a constant read bias of 250 mV. (b) Photoelectric response of Device BL5 at 5 Hz of exposure frequency, measured under a constant read bias of 1 V.

C11. Photoelectric response of ITO electrodes

The optical response of top and bottom ITO electrodes to the different wavelengths (**Figure C12**) shows that both electrodes are insensitive to the exciting illuminations.

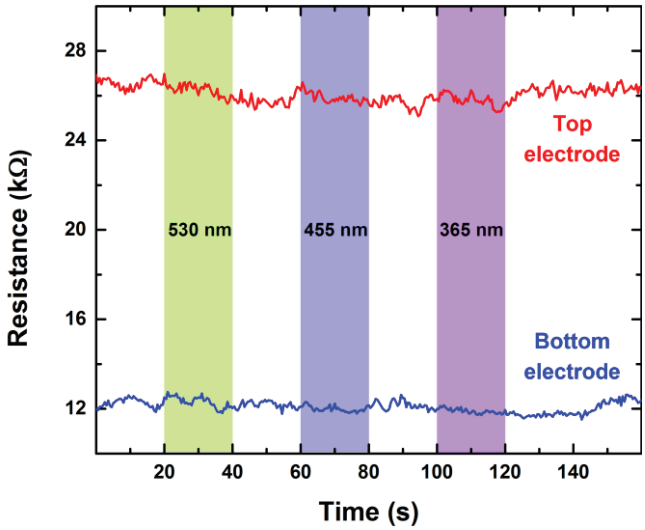

Figure C12 The optical response of ITO electrodes to 365, 455, and 530 nm of illumination wavelengths at a V_{READ} of 100 mV.

References

[C1] R. Dittmann, R. Muenstermann, I. Krug, D. Park, T. Menke, J. Mayer, A. Besmehn, F. Kronast, C. M. Schneider, R. Waser, *Proc. IEEE* **2012**, *100*, 1979.

[C2] R. Waser, R. Dittmann, G. Staikov, K. Szot, *Adv. Mater.* **2009**, *21*, 2632.

[C3] M. Hansen, M. Ziegler, L. Kolberg, R. Soni, S. Dirkmann, T. Mussenbrock, H. Kohlstedt, *Sci Rep* **2015**, *5*, 13753.

[C4] J. H. Park, C. Buurma, S. Sivananthan, R. Kodama, W. Gao, T. A. Gessert, *Appl. Surf. Sci.* **2014**, *307*, 388.

[C5] A. Thøgersen, M. Rein, E. Monakhov, J. Mayandi, S. Diplas, *J. Appl. Phys.* **2011**, *109*, 113532.

[C6] L.-j. Meng, A. Maçarico, R. Martins, *Vacuum* **1995**, *46*, 673.

[C7] W. Wen-Fa, C. Bi-Shiou, H. Shu-Ta, *Semicond. Sci. Technol.* **1994**, *9*, 1242.

[C8] D. Ehre, H. Cohen, V. Lyahovitskaya, I. Lubomirsky, *Phys. Rev. B* **2008**, *77*, 184106.

[C9] H. Nili, S. Walia, A. E. Kandjani, R. Ramanathan, P. Gutruf, T. Ahmed, S. Balendhran, V. Bansal, D. B. Strukov, O. Kavehei, M. Bhaskaran, S. Sriram, *Adv. Funct. Mater.* **2015**, *25*, 3172.

[C10] P. V. Nagarkar, P. C. Searson, F. D. Gealy, *J. Appl. Phys.* **1991**, *69*, 459.

[C11] Y.-F. Lan, Y.-H. Chen, J.-L. He, J.-T. Chang, *Vacuum* **2014**, *107*, 56.

[C12] T. O. L. Sunde, E. Garskaite, B. Otter, H. E. Fossheim, R. Sæterli, R. Holmestad, M.-A. Einarsrud, T. Grande, *J. Mater. Chem.* **2012**, *22*, 15740.

[C13] R. F. Egerton, *Electron Energy-Loss Spectroscopy in the Electron Microscope*, Springer, US, 3 edn., 2011.

[C14] J. Rho, J. Kim, S. Shin, J. Kwon, M. Kim, J. Song, E. Choi, *J. Lumin.* **2010**, *130*, 1784.

Appendix D: Supporting Information for Chapter 6

D1. Electrical characterization of *a*-STO_x devices

Figure D1 shows the resistance of as-fabricated *a*-STO_x devices with respect to their active area. The resistances of at least 15 devices, with same active area are measured under a read voltage (V_{READ}) of 0.1 V.

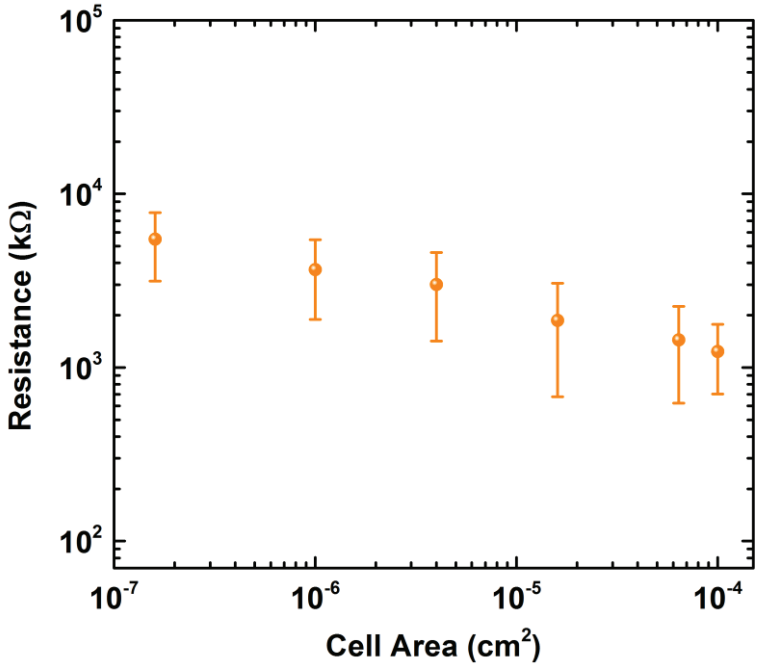

Figure D1 Electrical characterization of the pristine *a*-STO_x devices. The pristine resistance measured for at least 15 devices of the same cell area at V_{READ} of 0.1 V. The error bars show the standard deviation in the measurement.

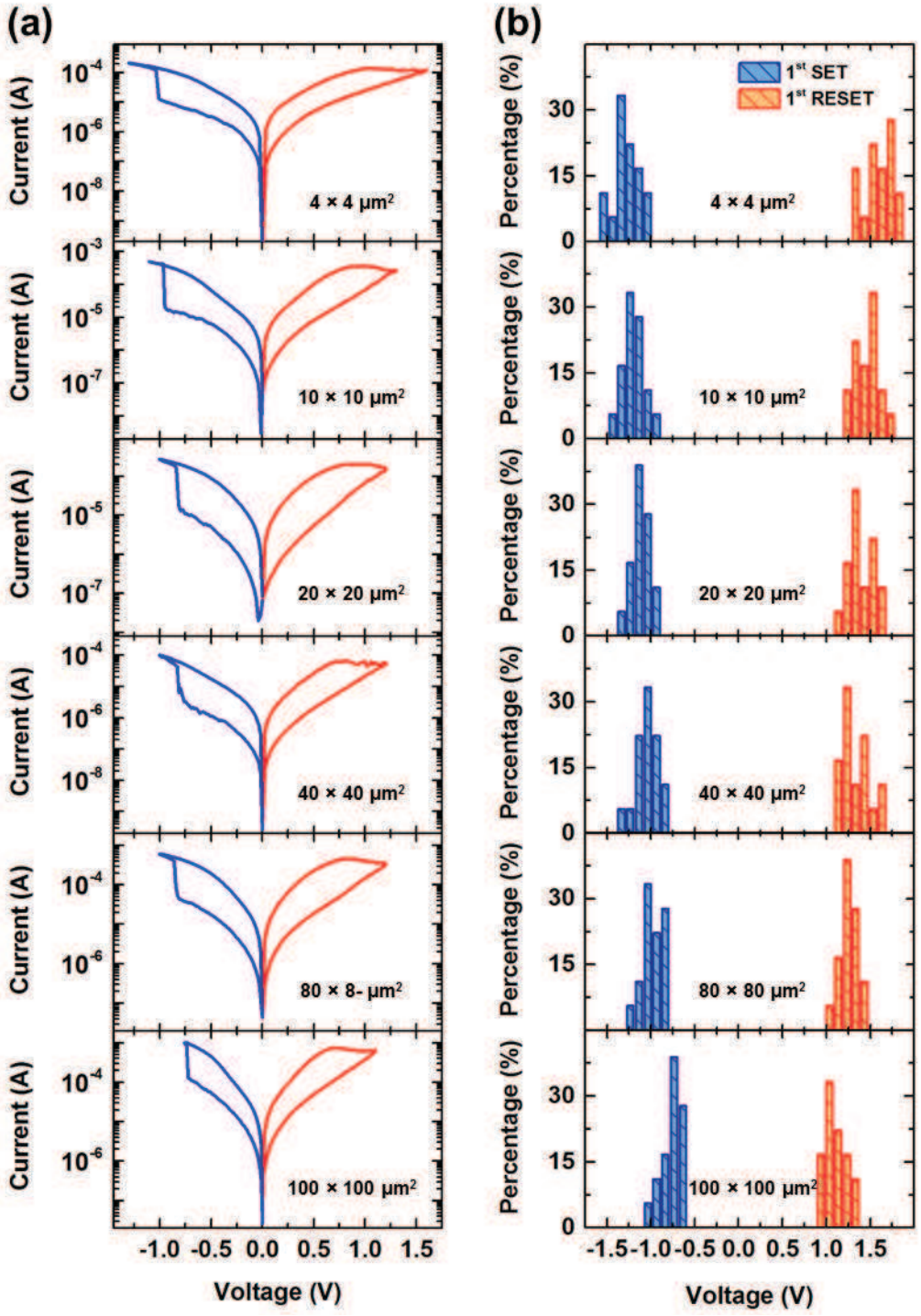

Figure D2 First SET/RESET characterization of the *a*-STO_x devices. (a) The representative *I-V* characteristics of the first SET/RESET sweeps. The current compliance is set at ≥0.5 mA during the *I-V* sweeps. (b) The statistics of the first V_{SET} and V_{RESET} of at least 15 MIM devices with same cell sizes.

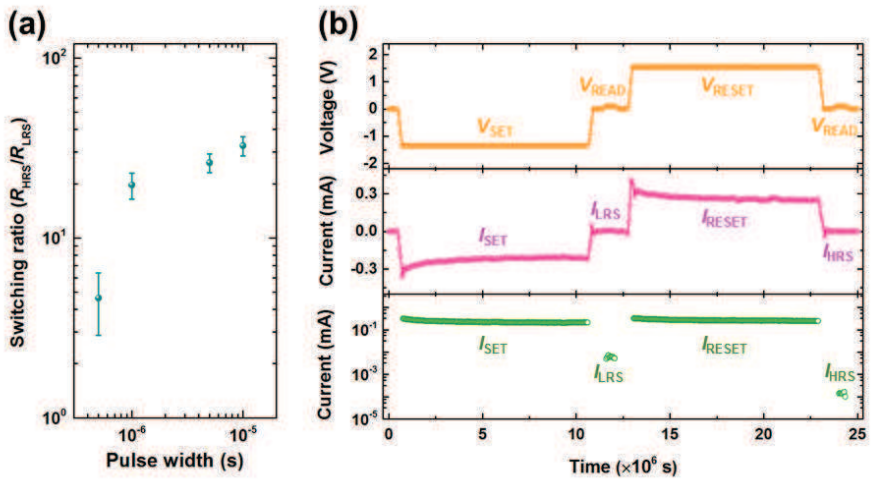

Figure D3 Characterization of SET/RESET pulses for the endurance of *a*-STO$_x$ MIM devices. (a) Effect of SET and RESET pulse width on switching ratio. The READ pulses with amplitude of 0.1 V and fixed width of 200 ns are used to measure the switching ratios of 15 MIM devices with 10×10 μm^2 active area. (b) Response of the MIM device to the input V_{SET} (-1.4 V)/V_{RESET} (+1.6 V) voltage pulses with 1 μs pulse width (500 ns rise and fall time) and 0.1 V V_{READ} pulses with width of 200 ns. The upper panel shows the input voltage pulses, middle panel shows measured current response to the applied voltage pulses on a linear scale while the lower panel shows only SET/RESET and LRS/HRS read currents on a log scales.

D2. Cross-sectional analyses of *a*-STO$_x$ devices

Transmission electron microscope (TEM) and electron energy loss spectroscopy (EELS) techniques are used to analyze the morphology and composition of the *a*-STO$_x$ MIM devices. **Figure D4a** shows a TEM micrograph of the pristine *a*-STO$_x$ MIM device. During the TEM and live-FFT observation of the pristine devices, no noticeable crystalline regions are identified in the top Ti or the *a*-STO$_x$ functional oxide layer. To assess the electronic composition of the pristine device, the EELS area map and Ti–$L_{2,3}$ and O–*K* edge profiles are obtained from a line-scan across the MIM structure (Figure D4b,c respectively). The EELS O–*K* area map (Figure D4b) shows the presence of low oxygen content in the *a*-STO$_x$ oxide layer which indicates its oxygen deficient stoichiometry. The EELS Ti–$L_{2,3}$ edge profiles collected along a line scan (Figure D4c) show broad Ti–L_3 and Ti–L_2 peaks at the top Ti/*a*-STO$_x$ interface indicate the presence of mixed Ti^{2+} and Ti^{3+} oxidation states.[D1] In the functional oxide layer, weak splitting

of the t_{2g} and e_g peaks indicate Ti^{4+} oxidation state. However, O–*K* edge profiles are weak and noisy which makes difficult to clearly distinguish the fine structures and cannot be used to accurately identify the Ti valence.

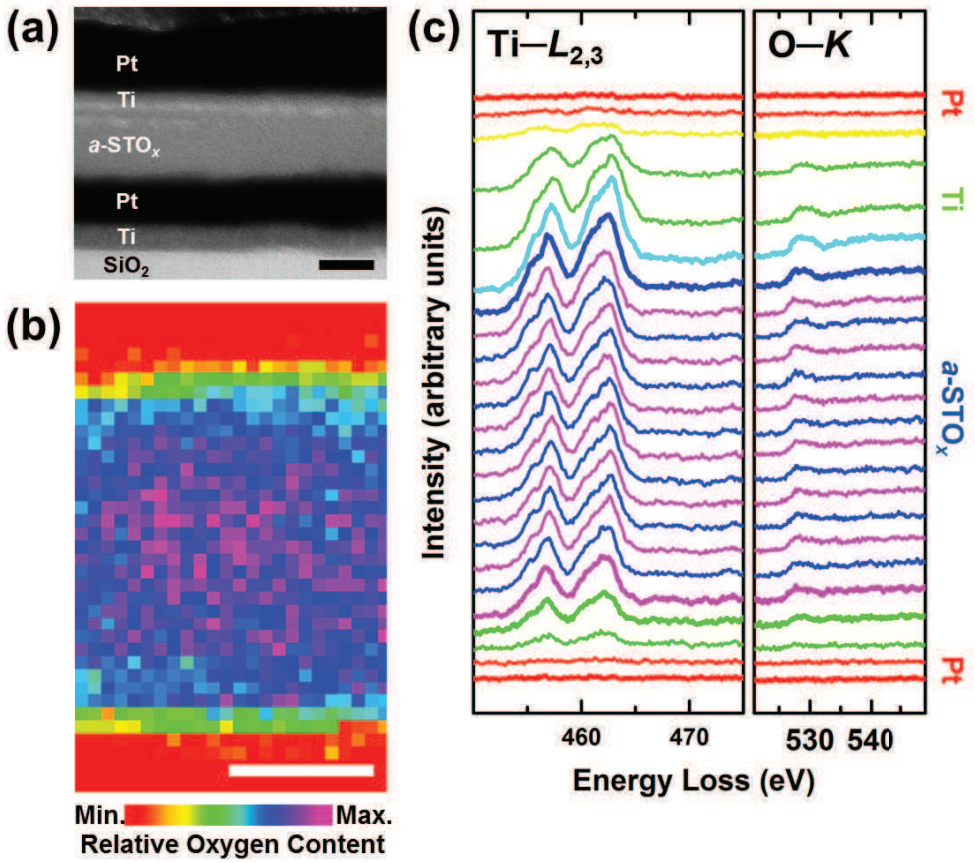

Figure D4 Microstructure and electronic structure of the pristine a-STO_x devices. (a) TEM cross-section of a pristine device. Scale bar 20 nm. (b) The EELS O–*K* edge area map of a pristine device. Scale bar 20 nm. (c) The EELS Ti–$L_{2,3}$ and O–*K* edge profiles along a line scan across the pristine device.

D3. Spike-time conversion to voltage

The time-to-digital-to-voltage circuitry converts spike-timing information into corresponding voltage magnitude. The corresponding voltages are applied to the bottom or top electrode of the *a*-STO_x synaptic devices, depending on the sign of Δt_1 (potentiation or depression). **Table D1** lists the selected Δt_1 values and corresponding voltage amplitudes.

Depression		Potentiation			
Δt_1 (ms)	ΔV (V)	Δt_1 (ms)	ΔV (V)		
			Δt_2 = 10 ms	Δt_2 = 80 ms	Δt_2 = 160 ms
-45	0.500	3	-0.800	-0.900	-1.200
-42	0.529	6	-0.778	-0.875	-1.167
-39	0.557	9	-0.757	-0.850	-1.135
-36	0.586	12	-0.735	-0.825	-1.103
-33	0.614	15	-0.714	-0.800	-1.071
-30	0.643	18	-0.692	-0.775	-1.039
-27	0.671	21	-0.671	-0.750	-1.007
-24	0.700	24	-0.650	-0.725	-0.975
-21	0.729	27	-0.628	-0.700	-0.942
-18	0.757	30	-0.607	-0.675	-0.910
-15	0.786	33	-0.585	-0.650	-0.878
-12	0.814	36	-0.564	-0.625	-0.846
-9	0.843	39	-0.542	-0.600	-0.814
-6	0.871	42	-0.521	-0.575	-0.782
-3	0.900	45	-0.500	-0.550	-0.750

Table D1 Conversion of the spike-timing information to voltage. Selected values of Δt1 are simulated to obtain corresponding voltage amplitudes.

Triplet pairing	Timing difference		Weight change	
	Δt_1	Δt_2	Hippocampal experiments	*a*-STO_x memristors
2-pre-1-post	5	-5	-0.01±0.04	-0.01±0.02
	10	-10	0.03±0.04	0.01±0.02
	15	-5	0.01±0.03	0.01±0.02
	5	-15	0.24±0.06	0.28±0.03
1-pre-2-post	-10	10	0.34±0.04	0.33±0.05
	-5	5	0.33±0.04	0.33±0.05
	-5	15	0.22±0.08	0.23±0.04
	-15	5	0.29±0.05	0.31±0.06

Table D2 Comparison of Hippocampal data set and *a*-STO_x memristors. The synaptic weight change corresponding to different spike time differences is listed for both 2-pre-1-pre and 1-pre-2-post triplet pairing configurations. The Hippocampal data set is taken from Ref.[D2]

Spike rate ρ (Hz)	Cortex		*a*-STO_x memristors	
	Δt = 10 ms	Δt = -10 ms	Δt = 10 ms	Δt = -10 ms
0.1	-0.29±0.08	-0.04±0.05	-0.28±0.03	-0.006±0.02
10	-0.41±0.11	0.14±0.1	-0.43±0.04	0.13±0.03
20	-0.34±0.1	0.29±0.14	-0.35±0.04	0.31±0.05
30	0	0.4±0	0±0.01	0.37±0.04
40	0.56±0.32	0.53±0.11	0.37±0.04	0.37±0.04
50	0.75±0.19	0.56±0.26	0.37±0.04	0.37±0.04

Table D3 Comparison of Visual Cortex data set and *a*-STO_x memristors. The synaptic weight change corresponding to the different spike rates is listed for both Δt = 10 ms and Δt = -10 ms. The Visual Cortex data is taken from Ref.[D2]

D4. Event Digitizor and Time-to-Voltage Converter

The T2D (time-to-digital) module of our proposed CMOS circuitry (shown in Figure 6a in the main manuscript) includes a timing control unit and a decoder as shown in **Figure D5a**. The timing control unit is a fully digital unit that receives pre and post digital spikes and generates timing interval signals solely based on counters. It can be configured for multiple protocol implementation and Δt detection.[D3] The resolution of timing detection for any Δt is identified by (1) meaningful changes in synaptic weight (Δw) as the result of applying slight changes in voltage, and (2) resolution of overall time-to-voltage (V_w) conversion which is mainly depends on the DAC resolution. The T2D module passes a multi-bit spike timing (ST) digital signal to a decoder where two multi-bit horizontal/vertical select (HS/VS) digital signals are generated to adjust the number of resistors in series in our resistive DAC. The ST signal contains information about Δt_1 and Δt_2 and their different configurations which then are translated into an equivalent voltage (V_w) to be generated. It also includes flags that are part of Sel_R and Sel_C and identify whether a Δt is positive or negative, hence, applying V_w to the top or the bottom electrodes.

Figure D5b shows schematic of a single cell with two polysilicon resistors, controls and input/output signals. For a k-bit DAC, 2^k resistors are required. More detail on the implementation of the DAC and voltage follower/buffer (VF) is provided in Ref.[D4]

Figure D5c illustrates generation of an internal reference voltage (V_{ref}) by using a voltage divider and also demonstrates a regulated current mirror to generate and regulate a fixed reference current to the chain of DAC resistors. The signal ENA provides the option to minimize the static current flowing through the resistor chain when the time-to-voltage circuit is disabled. It is worth highlighting again that these signals are affecting Sel_R and Sel_C to select a device in the array. As stated, voltage V_{DAC} identifies maximum required voltage for programming the a-STO_x memristor. In case of V_{DAC} = 700 mV, 6-bit resistive DAC, and 1.2 V supply voltage in 90 nm standard CMOS technology, a 543 mV dynamic range on V_w, 191 µA active mode current, 99 nA standby mode leakage current at room temperature, and a 235 mV/µs slew rate is achieved.[D4] The circuit also demonstrates a strong accuracy of ±5 mV with 8.5 mV step sizes. While we have modified the design, the original design is reported to have an area of around 175×175 µm^2 capable of driving up to 1 mm^2 of digital IP block.[D4] We have added a fully digital timing control unit and removed n-well bias

generation. While the main analog components are still part of the circuit, we estimate an area reduction of at least 20% is achievable in the modified time-to-voltage circuitry in comparison with the original body bias generator circuitry.

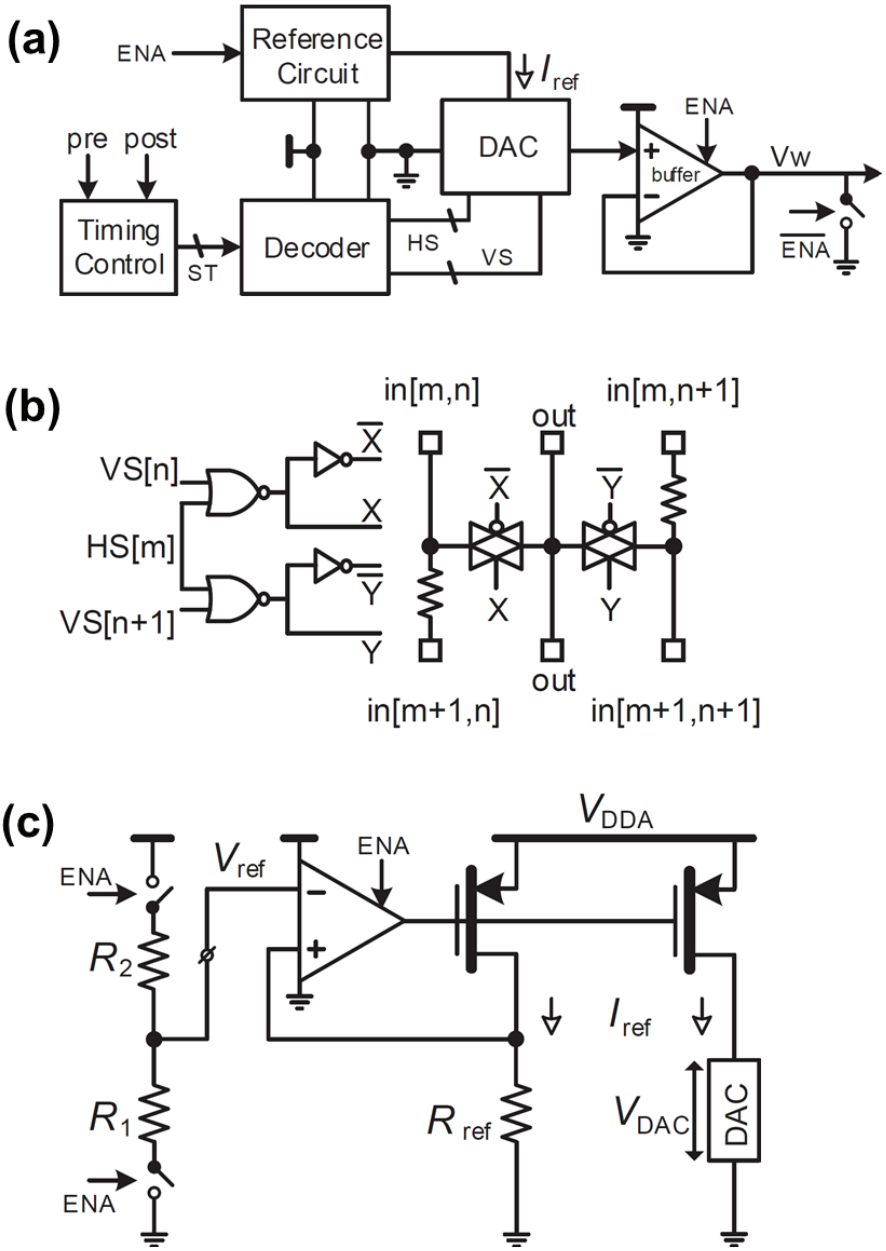

Figure D5 Event digitization and Time-to-Voltage conversion. Schematics of (a) time-to-digital module, (b) a single cell of resistive DAC and (c) a circuit to generate and regulate reference current and voltage for DAC.

References

[D1] Y. Li, Q. Wang, M. An, K. Li, N. Wehbe, Q. Zhang, S. Dong, T. Wu, *Adv. Mater. Interf.* **2016**, *3*, 1600201.

[D2] J. P. Pfister, W. Gerstner, *J. Neurosci.* **2006**, *26*.

[D3] S. Friedmann, J. Schemmel, A. Grübl, A. Hartel, M. Hock, K. Meier, *IEEE Trans. Biomed. Circuits Syst.* **2017**, *11*, 128.

[D4] M. Meijer, J. P. d. Gyvez, IEEE Transactions on Very Large Scale Integration (VLSI) Systems **2012**, 20, 42.

Appendix E: Fabrication and Characterization of *a*-STO memristors

E2. Deposition of amorphous STO oxides

In this research work, *a*-STO thin films with different compositions are deposited by room temperature sputtering. Undoped *a*-STO thin films are deposited *via* RF-mangetron sputtering of a stoichiometric STO ceramic target, while metal doping (*i.e.*, Nb and Cr) is achieved by DC co-sputtering of metal targets. The sputtering parameters used in this work are listed in Table E1.

Ceramic target	$SrTiO_3$
Metal targets	Nb, Cr
Process gases	0, 5% O_2 in Ar, 100% Ar
Base pressure	$<5 \times 10^{-7}$ Torr
Process pressure	3.5×10^{-7} Torr
Process temperature	25 ˚C
RF power	100-200 W
DC power	4-40W

Table E1 Sputtering and co-sputtering parameters for doped and undoped STO thin films.

The oxygen partial pressure as well as the sputtering powers on both RF and DC sources are systematically varied to achieve different concentrations of the oxygen vacancies and dopant species. The thicknesses of the thin films are controlled by the sputtering time. Detailed specifications of the sputtering parameters used to deposit different *a*-STO thin films are explained in the following sections.

E2. Fabrication of Nb-doped *a*-STO_x memristors

Microscale Nb:*a*-STO_x MIM devices in crossbar array configuration (20-100 μm symmetric electrode sizes) were fabricated on SiO_2/Si substrates using a three step photolithography/lift off process. In the first lift-off step, 50 nm bottom Pt electrodes with 10 nm TiO_2 adhesion layers were deposited on pre-patterned SiO_2/Si substrates by electron beam evaporation at room temperature. Nb:*a*-STO_x thin films of 100 nm thickness with a nominal oxygen deficiency of 3-4% were then RF sputtered at room temperature in a pure argon atmosphere through a shadow mask. Lastly, Pt/Ti (50:10 nm) top electrodes were patterned using photolithography deposited by electron beam evaporation to complete the crossbar structure.

E3. Fabrication of Cr-doped *a*-STO_x memristors

The Cr: *a*-STO_x resistive switching devices in cross-point configuration are fabricated *via* standard photolithography/lift-off and thin film deposition processes. After patterning through a photolithography (chrome) mask, the bottom Pt (7 nm)/Ti (3 nm) electrodes are evaporated onto a SiO_2 (300 nm)/Si substrate by electron beam evaporation (Kurt J. Lesker PVD75 Pro-line). A 25 nm thin film of amorphous Cr doped oxygen-deficient STO is sputtered (Kurt J. Lesker PVD75 sputtering system) in a pure argon atmosphere at room temperature from a commercial ceramic STO target (99.95%, Testbourne Ltd) by using 200 W RF (13.54 MHz) plasma and under a sputtering pressure of 3.5×10^{-3} Torr. Cr was incorporated into STO by co-sputtering of metallic Cr target (99.95%, Testbourne Ltd) by using 4 W DC power. Finally, following the photolithographic patterning, top Pt (35 nm)/Ti (8 nm) electrodes are evaporated by electron beam evaporation at $<5\times10^{-7}$ Torr base pressure. The *a*-Cr:STO_x MIM cross-point devices with active area of 2×2 μm^2, 4×4 μm^2 10×10 μm^2, 20×20 μm^2, 40×40 μm^2, 80×80 μm^2 and 100×100 μm^2 are fabricated.

E4. Fabrication of transparent *a*-STO memristors

The transparent *a*-STO based resistive memories (*t*-ReRAMs) are fabricated in a cross-point configuration on a glass (Pyrex) substrate *via* standard photolithography/lift-off and sputter deposition processes. To study the effect of cell size on the resistive

switching characteristics, different *t*-ReRAM cells are fabricated with lateral dimensions of 2×2 μm^2, 4×4 μm^2, 10×10 μm^2, 20×20 μm^2, 40×40 μm^2, 80×80 μm^2 and 100×100 μm^2. Each *t*-ReRAM cell comprises of a bilayer homojunction of *a*-STO, with different oxygen vacancy concentrations, sandwiched between two transparent conductive oxide (TCO) electrodes. A pair of bottom (30 nm) and top (40 nm) ITO electrodes are RF sputtered in a pure Ar atmosphere from a commercial ITO source (In_2O_3:SnO_2 in a 90:10 wt%, Testbourne Ltd.). A detailed description on the stoichiometry of sputtered ITO thin films is provided in Appendix C. Room temperature RF sputtering of ITO in pure Ar environment results in thin films with poor transparency. In order to enhance optical transparency, the bottom ITO electrodes are annealed in ambient conditions at 400 ˚C for one hour in a furnace. Subsequently, the bilayer homojunction of *a*-STO is RF sputtered at room temperature from a ceramic $SrTiO_3$ source (99.95% pure, Testbourne Ltd.). In order to enable repeatable resistive switching in *t*-ReRAM cells, an underlying Ti (5 nm) layer is DC sputtered in a pure Ar environment and capped with a top ITO electrode to form asymmetric top ITO/Ti/*a*-STO_x interface. Single layer and bilayer *t*-ReRAM cells with symmetric interfaces are also fabricated by following the processes explained above. Their electrical characterization shows unstable resistive switching behavior (Appendix C), necessitating the use of asymmetric interfaces in this work.

E5. Fabricaiton of *a*-STO memristors for synaptic functions

The *a*-STO_x synaptic devices are fabricated as cross-point devices and array in metal-insulator-metal (MIM) configuration with active areas of 2×2 μm^2, 4×4 μm^2, 10×10 μm^2, 20×20 μm^2, 40×40 μm^2, 80×80 μm^2 and 100×100 μm^2 by following standard photolithography and thin film deposition processes. The bottom Pt (15 nm)/Ti (7 nm) electrodes are patterned onto a SiO_2 (300 nm)/Si substrate by electron beam (e-beam) evaporation. As a switching layer, 25 nm thin film of amorphous oxygen-deficient STO is deposited by using radio frequency sputtering (with 100 W power) from a commercial STO ceramic target in a pure argon environment under a pressure of 0.46 Pa and at room temperature. In order to complete the MIM structure, top Pt (30 nm)/Ti (5 nm) electrodes are evaporated by the e-beam evaporation at a base pressure of $<6\times10^{-5}$ Pa.

E6. Electrical characterization

The electrical characterizations of the *a*-STO memristive devices are performed under ambient pressure by using the Keithley 4200SCS equipped with remote preamplifiers and 4225 pulse modulation unit connected to a micro-probe station.
High temperature electrical measurements are performed by using an environmentally isolated Linkum chamber connected with an Agilent 2912A sourcemeter.

E7. X-ray photoelectron spectroscopy

X-ray photoelectron spectroscopy (XPS) analysis is conducted by using a Thermo Scientific K-Alpha instrument utilizing an aluminum *K*α radiation source (1486.6 eV) is used. The XPS spectra are collected from bare *a*-STO oxide thin films, sputtered on SiO_2/Si substrates. All spectra were resolved by using the standard Gaussian-Lorentzian function followed by the Shirley background correction.

E8. Photoluminescence spectroscopy

The photoluminescence emission spectra are obtained using a Horiba Scientific FluoroMax-4 spectrofluorometer. All spectra are collected at room temperature from as-deposited bare *a*-STO_x thin films sputtered on SiO_2/Si substrates. A laser source is used to excite the sputtered oxides.

E9. Secondary ion mass spectroscopy

Dynamic secondary ion mass spectrometry (SIMS) analyses are carried out with a CAMECA NanoSIMS 50L. Elemental depth profiles are obtained using a Cs^+ primary ion source with a beam diameter of approximately 100 nm, impact energy of 16 keV and a beam current of approximately 3 pA. The instrument is operated in multi-collector mode, allowing the simultaneous detection of O^-, TiO^-, SrO^- and CrO^-. The raster size is 15 μm^2, however, only secondary ions from the central 10 μm^2 are used to determine the depth profiles. The mass spectrometer is calibrated using a commercial stoichiometric $SrTiO_3$ single-crystal (100) substrate and pure Ti and Cr metals, prior to the characterization of the MIM devices.

E10. Cross-sectional analyses

The transmission electron microscopy (TEM) and electron energy loss spectroscopic (EELS) analyses are performed on pristine, electroformed and switching (at least for 100 cycles and subjected to constant bias stresses) *a*-STO MIM devices using a JEOL 2100F scanning transmission electron microscope (STEM) with attached Tridium Gatan image filter with an entrance aperture of 5 mm. Thin TEM lamellae are prepared by focused ion beam (FIB) cuts through the MIM structure by using a FEI Scios DualBeam^{TM} system. Cross-sectional STEM micrographs and EELS spectra are collected using a <1.5 nm beam spot. EELS spectra are collected with a dispersion of 0.3 eV per pixel which allowed simultaneous recording of the titanium $L_{2,3}$ (Ti–$L_{2,3}$) edge and oxygen *K* (O–K) edge in the regions of interest (ROIs) and across the MIM cross-sections. A power law fit is adopted for the pre-edge background correction while the influence of nearby peaks and plural scattering are reduced by narrow signal windows.